Modeling the influence of bone mineralization and remodeling on the structure of bone

D I S S E R T A T I O N

zur Erlangung des akademischen Grades

doctor rerum naturalium (Dr. rer. nat.)
im Fach Physik

eingereicht an der
Mathematisch-Naturwissenschaftlichen Fakultät I
Humboldt-Universität zu Berlin

von
Diplom Physikerin Carolin Lukas

Präsident der Humboldt-Universität zu Berlin:
Prof. Dr. Jan-Hendrik Olbertz

Dekan der Mathematisch-Naturwissenschaftlichen Fakultät I:
Prof. Stefan Hecht, PhD

Gutachter:
1. Prof. Dr. Dr. h.c. Peter Fratzl
2. Prof. Dr. Igor Sokolov
3. Prof. Dr. Dr. h.c. Jürgen Kurths

eingereicht am: 07.08.2012
Tag der mündlichen Prüfung: 11.12.2012

Für Monika und Hans W. Stoermer.

Kurzfassung

Die Struktur des Knochenmaterials ist während des gesamten Lebens dynamischen Prozessen unterworfen, die es stetig modifizieren. Diese Prozesse sind zum einen der Umbauprozess, in welchem existierendes Material entfernt und durch neues, vorerst weiches ersetzt wird. Und zum anderen der Mineralisierungsprozess, bei dem Mineralien eingelagert werden und somit die Steifigkeit des weichen Materials erhöht wird. Diese zwei Prozesse führen zu einem heterogenen Knochenmaterial. Das komplexe Zusammenspiel kann durch Knochenkrankheiten beeinflusst werden und zu einem mechanischen Versagen des Materials führen. Wie viel Einfluss dabei allein dem Umbauprozess und dem Mineralisierungsprozess zuzuschreiben sind, konnte bislang nicht geklärt werden. Während der Umbauprozess mechanisch kontrolliert ist, ist wenig bekannt wie mechanische Stimuli die Mineralisierung beeinflussen.
An diese Fragestellungen wird in der vorliegenden Dissertation mit physikalischen und numerischen Methoden herangegangen.
Das heterogene Material ist das Ergebnis des Mineralisierungs- und Umbauprozesses und wird abkürzend BMDD (für bone mineralization density distribution) genannt. Die BMDD ist für alle gesunden Erwachsenen gleich und weicht bei Knochenkrankheiten von dieser gesunden Referenzkurve ab. Die BMDD wurde zuerst entfaltet, um etwaige Verbreiterungen, hervorgerufen durch den Messprozess, ausschließen zu können. Das Ergebnis ist eine leicht schmalere Kurve. Im nächsten Schritt wurde ein bestehendes mathematisches Model so erweitert, dass der Einfluss einer erhöhten bzw. reduzierten Mineralisierungskinetik auf die BMDD untersucht werden konnte. Die Simulationen ergaben dabei, dass eine Verschiebung der BMDD zu niedrigerem Mineralgehalt im Knochen nicht nur durch eine erhöhte Umbaurate erreicht werden kann, sondern auch durch eine reduzierte Mineralisierungskinetik. Umgekehrt wird eine Verschiebung zu höheren Mineralgehalten dadurch erreicht, dass die Mineralisierungskinetik erhöht oder die Umbaurate reduziert wird. Der Unterschied der beiden Prozesse liegt bei einer Verschiebung zu niedrigeren Mineralgehalten in der Übergangsphase, während sich bei einer Verschiebung zu höheren Mineralgehalten der Gleichgewichtszustand des Knochens unterscheidet.
Durch die neuartige Auswertung von drei-dimensionalen *in vivo* Mikro-Computertomographieaufnahmen (mikro-CT), wurde der Einfluss von mechanischer Belastung auf die Mineralisierung des Knochens erforscht. Auf der Basis dieser Daten konnte zusätzlich zum Einfluss der mechanischen Belastung auf die Mineralisierung, auch die Mineralisierung in den einzelnen Bereichen *in vivo* im Knochen quantifiziert werden. Die Auswertung der mikro-CT-Aufnahmen bestätigte, die schnellere Mineralisierung im neugeformten und die langsamere in bereits vorhandenem Knochen. Es konnte gezeigt werden, dass mechanische Stimulation die Mineralisierung im Knochen beschleunigt. Außerdem wurde erstmals *in vivo* gezeigt, dass abgebauter Kno-

chen entmineralisiert, bevor er vollständig abgebaut wird.
Wie der Umbauprozess im kompakten Knochen gesteuert sein kann, wurde mit Hilfe eines Algorithmus quantifiziert. Mit diesem wurden zwei-dimensionale Bilder erzeugt, in die nach und nach Knochenbausteine eingesetzt wurden. Die Bilder wurden mittels Berechnung der Autokorrelationsfunktion ausgewertet und mit den experimentellen Daten verglichen. Die Anordnung der Knochenbausteine ließ sich beschreiben, indem es für einen Knochenbaustein verboten war innerhalb einer definierten Zone eines anderen Bausteins gebildet zu werden. Diese Zone ließ sich am besten durch einen normalverteilten Radius, mit einer dazugehörigen Variabilität beschreiben.
In der vorliegenden Arbeit konnten die Mineralisierung und der Umbauprozess getrennt voneinander betrachtet und quantifiziert werden. Mittels Computersimulationen wurden die beiden Prozesse so verändert, dass deren Einfluss auf den Knochen besser verstanden bzw. unterschieden werden kann.

Abstract

Bone material structure is the result of the interplay of two dynamic processes known as remodeling and mineralization. Remodeling is the process during which existing bone is replaced by new, initially soft material. Mineralization on the other hand is the process during which stiff mineral particles are incorporated into the soft material. The complex interplay between these processes influences the performance of bone throughout life and results in a heterogeneous material. This interplay can be perturbed by bone diseases, which can lead to material failure. However, it remains unclear to which degree each of these two processes contributes during diseases. Additionally, while the remodeling process is known to be mechanically controlled, it is unclear how mechanical stimuli affect the mineralization process.

The heterogeneous mineral distribution in trabecular bone is the result of the complex interplay between the mineralization and the remodeling process and is called bone mineralization density distribution (BMDD). The BMDD is similar for all healthy adult humans. A deviation from this healthy distribution is indicative of bone diseases. The influence of the measuring process on the distribution is first quantified by deconvolution of the BMDD, revealing a narrower distribution. Subsequently, a mathematical model is modified in such a way that the influence of an increased or decreased mineralization kinetics on the BMDD can be characterized. In the simulations, it is demonstrated that a shift of the mineral distribution to lower mineral contents can be achieved not only by an increase in the remodeling process, but also by a reduction in the mineralization kinetics. In the steady state, the resulting distributions are almost indistinguishable while differences occur during the transition phase. For a shift to higher mineral contents, the situation is reversed. The time evolution of the distributions has a very similar behavior, whereas the final steady state is different.

The influence of mechanical stimuli on the mineralization is investigated by a novel three-dimensional analysis of *in vivo* micro-computed tomography images (micro-CT) of the vertebra in a mouse tail. It was shown that mechanical stimulation accelerates mineralization in the non-remodeled bone and it is possible to quantify the rapid mineralization of newly formed bone compared to non-remodeled bone. For the first time it could be shown that the bone is demineralized before it is completely resorbed.

An algorithm was developed to understand how the remodeling process can be influenced in the compact bone of horses. This algorithm produces images which are gradually filled with specific building blocks. The image is evaluated by calculating the autocorrelation function, which is then compared to the experimental data. The arrangement of the building blocks could be described when such a block could only be placed within a defined zone of another building block. This zone could be best

quantified when its radius was normally distributed with a corresponding standard deviation.

The present work attempts to better understand the mineralization and remodeling processes in bone using computer modeling. These processes could be influenced and quantified in such a way that their consequences on the bone material could be characterized.

Contents

Nomenclature

BMDD	Bone mineralization density distribution
qBEI	quantitative backscattered electron imaging
BMDD parameters	
Ca_{Peak}	Most frequent calcium content
Ca_{Mean}	Mean calcium content
Ca_{Width}	Full width at half maximum (FWHM)
Ca_{Std}	Standard deviation of calcium content)
Deconvolution of the BMDD, section 3.1	
$\boldsymbol{g}$	measured BMDD
$\boldsymbol{f}$	deconvolved 'true' BMDD
$\boldsymbol{A}$	matrix relating $\boldsymbol{f}$ and $\boldsymbol{g}$
λ	regularization parameter
BMDD model with modified mineralization kinetics, section 3.3	
t_a	time of formation of a bone packet given in years
t	time given in years
$m(t-t_a)$	healthy mineralization law
$v(t-t_a)$	healthy mineralization velocity
g	parameter scaling the mineralization velocity
$h(t)$	introduced function to change the mineralization law with time
t_{ch}	Effective time describes how fast $h(t)$ changes
$M(t,t-t_a)$	mineralization law depending on $t-t_a$ and time t
Mineralization process *in vivo*, chapter 4	
micro-CT	micro-computed tomography
GL	gray level
mg HA/cm^3	unit of mineral content given in mg of hydroxyapatite (HA) per cubic volume
Spatial arrangement of osteons, chapter 5	
R_{ca}	Haversian canal radius of one osteon
R_{excl}	exclusion radius
ACF	auto correlation function
SDD	shortest distance distribution

1 Introduction

The human skeleton protects vital organs and mechanically supports the stature and the locomotion of the living organism throughout life [1, 2]. This remarkable performance of bone is on the one hand due to the hierarchical organization of the bone tissue from the macrometer down to the nanometer scale, and on the other hand its ability as a living tissue to adapt its structure to external stimuli [3, 4]. This adaptation of bone structure is largely determined through the interplay of two interconnected processes, known as remodeling and mineralization. Remodeling is the process during which existing bone material is replaced by newly formed, initially soft bone material [5]. Mineralization, however, is the process during which the soft bone material is reinforced by the incorporation of stiff mineral particles [2]. The complex interplay of these processes influences the performance of bone throughout life and results in a heterogeneous material [6]. The delicately balanced relationship between bone remodeling and mineralization can be perturbed by bone diseases, such as osteoporosis, often leading to an increased likelihood of fracture [7, 8]. Drug treatments against diseases can increase the material quality. However, it remains unclear to which degree each process contributes in the healthy or the diseased case. A proper understanding of the underlying physics which lead to deviations from the healthy state is needed in order to optimize the treatment and medication against bone diseases and further, to be able to evaluate their effectiveness. Most experiments are static snapshots of the bone that do not capture the development of bone over time. Computer simulations, on the other hand, can be used to predict such deviations for each process of remodeling and mineralization separately, and can thus provide vital support for interpretation of experimental results. Therefore, the mineralization and the remodeling process are studied with mathematical and numerical tools in this thesis by considering the bone at the micrometer level.

The mineralization process is a main contributor to the stability of the bone material since it stiffens by the incorporation of mineral [9]. Together with the remodeling these two processes lead to a bone material, which is heterogeneous in mineral content. The heterogeneity could be quantified by mineral distributions, which turned out to be similar in healthy adult humans. A deviation from this healthy distribution is indicative

of bone diseases such as osteoporosis, which is, amongst other things, characterized by a reduced mineral content. Such deviations from the healthy mineral distribution are measurable and diagnostic for specific bone diseases [6]. It is known that a shift towards lower mineral content can be achieved by an increase in bone remodeling. The consequence of changing the mineralization process on the mineral distribution, however, is not known. In order to investigate such deviations *in silico* in this thesis, the influence of the measuring process on the distribution is first quantified by deconvolution of the mineral distribution, to exclude measurement artifacts. The deconvolved distribution is used as input in a mathematical model that describes the influence of an altered remodeling process (but healthy mineralization) on mineral distribution [10]. This model is modified such that an increased or decreased mineralization can be characterized. The aim is to find out whether a change in the mineralization process acts differently on the mineral distribution than a change in the remodeling process and which consequences would follow from this study for the diagnosis of bone diseases.

To distinguish between the effects of bone remodeling and mineralization separately a detailed knowledge about the kinetics of both processes is essential. However, obtaining experimental evidence about the mineralization kinetics in bone *in vivo* is still lacking. Moreover, while the remodeling process is known to be mechanically controlled, it is unclear how mechanical stimuli affect the mineralization process. Therefore, the relatively new technique *in vivo* micro-computed tomography (micro-CT) is applied, which allows not only detecting the architecture of trabecular bone *in vivo* [11] but also to get information about its mineral content [12] over distinct time intervals. The advantage of this method is that in small animals the same bone can be examined over time reducing enormously the amount of animals needed. Usually lots of animals are sacrificed to obtain a time series of the investigated quantity. A disadvantage is, however, that this method is not yet applicable for humans due to the restricted size of the samples. A time series of three-dimensional images was provided, which were taken from a vertebra in a mouse tail [13]. With the provided data, not only the mineralization can be followed but also the influence of the mechanical stimuli on the mineralization process can be studied. The proposed evaluation aims to quantify the mineralization process in the bone with time.

In the third and last part, the aim was to understand how the remodeling process can be influenced in the compact bone. Compact bone is the bone that is found in the mid shaft of long bones such as the thigh bone. The long bones in, e.g. our legs, carry our weight every day without fracturing. In order to study the remodeling process in the compact bone, the arrangement of its basic building blocks on the micrometer scale is

investigated by using light microscopy images of horse bones. An algorithm was developed to quantify the arrangement of these building blocks. The simulated images are compared to the experimental images. Furthermore, the ordering is related to a more physiological meaning which should quantify the nutrient supply of bone cells embedded in the bone tissue. These cells have presumably crucial functions, e.g. controlling bone remodeling.

In order to understand the present work, first the background of this thesis is given, where the current knowledge about bone and its features are described. In chapter 3 the heterogeneous mineral distribution is studied, by showing first how it is deconvolved and second how an decreased/increased mineralization kinetic can be simulated and compared to changes in the remodeling rate. In chapter 4 the analysis of the micro-CT images is presented in order to quantify the mineralization process *in vivo*. In the last chapter 5 the algorithm is introduced to quantify the arrangement of the building blocks in cortical bone. Finally a short conclusion is given summarizing the results.

Bone mineralization and remodeling are complex and dynamic processes; however, it is important to understand these mechanisms as they have strong relevance to bone diseases. This work lends credence to the idea that computer modeling is a powerful tool for investigating these complex processes and even more powerful tool when used in cooperation with experimental data.

2 Background

Bone is a multifunctional organ which can also be considered as a biological material. It is composed of a soft protein matrix, mineral particles and water. The term bone material used in the following refers to the highly specialized type of dense connective tissue of its constituents. Since changes in the bone material are studied in section 3.3, the complex organization of the bone composite is explained before. In the first section the hierarchical structure of bone is presented in order to show the different structural motifs of trabecular and cortical bone. In the following sections, an overview of the current understanding of the remodeling and the mineralization process (section 2.2.1 and 2.2.2, respectively) is presented together with theoretical and computational models which are used to understand the relation between the structural adaptation and the dynamic processes in bone (section 2.2.3). The influence of a change in the remodeling and the mineralization process on trabecular bone is investigated in sections 3 and 4.
In the following section the bone mineralization density distribution (BMDD) is presented which is used as quantity to compare simulation and experiment (chapter 3). How the BMDD is measured and characterized is shown in detail in section 2.3.1. A mathematical model which describes the time evolution of the BMDD [14] is also presented. This model will be extended in section 3.3 to consider also dysfunctions of the mineralization process.
In the last two sections (2.4.1 and 2.4.2), experimental data are described which were kindly provided from cooperation partners. With the provided micro-computed tomography images the mineralization process is investigated *in vivo*. Finally light-microscopy images of the cortical bone of horses are used to study the remodeling process.

2.1 Bone as a material

Bone is hierarchically structured, i.e. going from the centimeter down to the nanometer scale bone shows at each level different structural motifs [3, 1, 15, 9, 2]. The motifs in one level provide the building blocks for the superior level.
In this thesis the two different bone types are investigated which can be distinguished

at a centimeter level, see longitudinal cut of a long bone in Figure 2.1A. One is called cortical bone which is the solid tissue of low porosity, found in the mid-shaft of the long bone. The second type is found in the broad ends of the long bones. There the cortical shell becomes thinner which surrounds a complex three-dimensional structure, called trabecular bone. Trabecular bone is investigated regarding the mineralization process (see section 2.2.2) in the chapters 3 and 4. Cortical bone and the arrangement of its building blocks, the osteons, is the topic in the last chapter of this thesis.

Trabecular bone is a complex sponge-like structure, see Figure 2.1A. Its porosity is about 80%. The structure consists of struts that can be rod- or plate-like [16] being about 100-300 μm thick and roughly 1 mm long [17], see Figure 2.1B right, obtained by scanning electron microscopy. A single strut consists of bone packets made of lamellar bone [18]. The bone packets are the basic building blocks of trabecular bone, approximately 50 μm thick, several hundred μm long and aligned approximately with the shape of the trabecular [19]. In the right Figure 2.1C a cross section of one strut is presented showing the different bone packets. Each bone packet has a different gray level which corresponds to a different mineral content. Bright gray represents a high amount, darker gray a low amount of mineral in the bone packet [20]. The differences in mineral content are the result of the remodeling and the mineralization process (see following sections).

Cortical bone is much denser (porosity of about 6%) than trabecular bone [2]. A typical feature of the cortical bone are its cylindrically shaped building blocks which are called osteons. A cross section through the cortical bone of a long horse bone shows the arrangement of osteons in Figure 2.1B (light microscopy). In three dimensions the osteons are approximately cylindrically shaped which a diameter of about 200-250 μm, as shown by the scheme in Figure 2.1C left. Their long axis runs approximately parallel to the long axis of the bone. The black circle marks a canal, the so-called Haversian canal, which remains free for nerves and a blood vessel. The black dots in the image mark the cavities of bone cells which are called osteocytes. All the osteocytes are interconntected by small channels called canaliculi building a network that intersperses the bone. The Haversian canals together with small pits housing bone cells which are interconnected by gap junctions, are the voids which are responsible for the low porosity of cortical bone [2]. The osteocytes probably sense the mechanical deformation of bone and therefore play an important role in the adaptation process of bone (see below). To maintain the network between them, the cells have to be well supplied with nutrients. In chapter 5 an algorithm is presented with which the arrangement of osteons can be quantified and related to nutrient supply in cortical bone.

The bone packets in trabecular and the osteons in cortical bone are made of lamellar

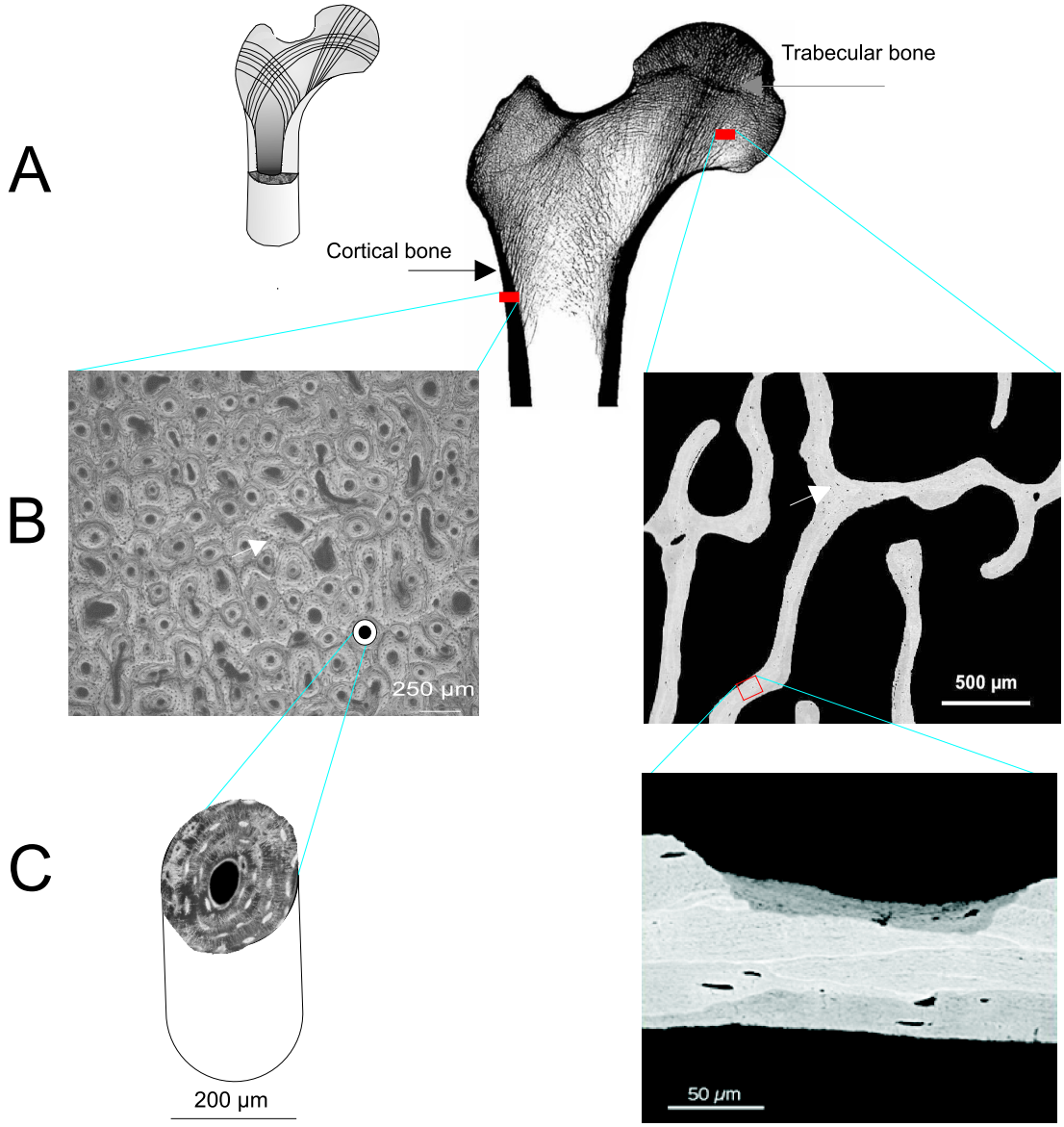

Figure 2.1: Hierarchical structure of bone. A: Cross-section through a long bone (proximal femur) showing cortical and trabecular bone. B left image: Zoom of the cross section of cortical bone shows the arrangement of osteons (courtesy of Ron Shahar). C left: Sketch of one cylindrically shaped osteon. In the middle a canal for the blood vessel and nerves remains free. The white spots show the osteocytes which are connected to each other (courtesy of M. Kerschnitzki). B right: Cross-section of the trabecular structure. C right image: arrangement of bone packets with different mineral content, represented by different gray values (from [9] with permission).

bone. Lamellar bone consists of sub-layers each consisting of parallel arranged fibers [3, 21]. The thickness of a lamella is approximately 5-7 μm [18] and the diameter of each fiber is about 1μm [15]. The fibers in lamellae are made of collagen fibers reinforced with calcium phosphate particles. It was found with transmission and scanning electron microscopy that the fiber direction spirals around an axis perpendicular to the layer [22]. The bone packets in human trabecular bone reveal a different arrangement than in cortical bone. The mineral particles, as measured with small-angle X-ray scattering

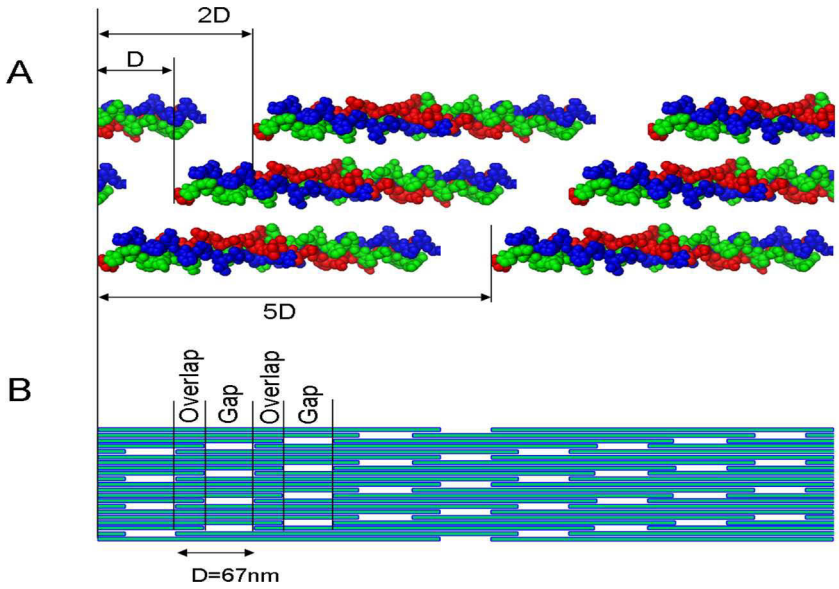

Figure 2.2: Periodical arrangement of the collagen molecules. A: The triple helix of the collagen molecules is indicated by the differently colored chains (image of a collagen molecule was kindly provided by N. Timofeeva). The molecules are periodically arranged in a staggered manner with the period D which is the overlap plus the gap regions. B: Array of molecules showing that one out of five molecules is missing in the gap regions.

[23, 24], are arranged parallel to a common direction instead of rotating around one axis. The fibers in the lamellae are a composite of a protein matrix, mainly collagen, mineral particles and water. The collagen molecules are arranged in a staggered manner [25]. The staggering leads to gaps and overlap regions which are arranged periodically with a period of D = 67 nm [25](Figure 2.2). The gap zones are probably the spots where the mineralization of the collagen matrix starts [26, 27]. The mineral particles are a version of calcium phosphate whose unit cell contains hydroxyapatite ($Ca_5(PO_4)_3(OH)$). The formed crystals can contain impurities, e.g. phosphate ions (PO_4^{3-}) are often replaced by carbonate groups (CO_3^{2-}), therefore the mineral in bone is often called carbonated

hydroxyapatite [28]. The mineralized collagen fibrils consist of an array of approximately 300 nm long and 1.5 nm thick triple helical collagen molecules. Measurements with small-angle X-ray scattering (SAXS) revealed size, shape and distribution of the crystals in the bone [29]. They are roughly 3 nm thick and 30 nm long [30] and mostly in alignment with the collagen fibrils [9]. 90% of the organic matrix is the structural protein collagen type I. The missing 10% are non-collageneous proteins, which probably play a role in controling the mineralization process [31].

Material properties of bone

The combination of the soft and tough collagen ($E \approx 1.5$ GPa [32]) with the stiff and brittle mineral (Young's modulus $E \approx 114$ GPa [32]) gives the bone the ability to be stiff enough to lift weights, i.e. not to deform under loads, and to be loaded without fracturing [33]. A model for the stiffness of the composite material bone at the nano-scale was developed by Jäger and Fratzl [34]. It estimates how the stiffness of bone depends on the staggered arrangement of the stiff mineral platelets embedded in the soft protein matrix. Under applied tensile load most of the load is carried by the mineral platelets by tensile stresses while the protein layer transfers the stress between the platelets via shear [35].
Not only that the bone combines this remarkable properties bone is also able to adapt to its environment. The orientation in the trabeculae, indicated by the lines in the small sketch in Figure 2.1A led to the assumption that there exists an adaptive process of bone to external mechanical stimuli [36]. The structural adaptation to mechanical stimuli was first proposed in the 19th century. The paradigm that bone is formed and resorbed where there is a mechanical need became known as the Wolff-Roux law [37, 38]. More information about the theory of structural adaptation is given in section 2.2.3. The mechanism which allows bone to adapt to its mechanical environment and to maintain the material properties are the remodeling and the mineralization process which are explained in the following sections.

2.2 Dynamic processes in bone

2.2.1 Bone remodeling

During bone remodeling discrete packets of bone are removed and replaced [5], (see Figure 2.3). This process is going on throughout life and is carried out by a complex interplay between specialized bone cells.

The remodeling process probably exists for structural and metabolic reasons. On the one hand it provides a mechanism to adapt to the external mechanical stimuli, to repair micro fractures and fatigue damages that appear after repetitive cycles of mechanical loading [39, 40]. On the other hand the skeleton is the largest calcium reservoir in the body and the remodeling process preserves the balance of minerals in the body. This so-called calcium homeostasis is regulated by reducing or increasing the amount of minerals in the surrounding fluid [39]. Although the remodeling process is not the only way the mineral exchange can occur [41, 42, 43, 44] it is presumably the main contributor. The homeostasis is independent of the site where the bone is remodeled as long as the mechanical performance is maintained. The repair of micro-damaged bone is obviously site-dependent and also the adaptation to mechanical stimuli is not random but driven to reinforce weak sites in the bone. These observations led to the suggestions of two kinds of bone remodeling: one being stochastic, in the sense of being not site-dependent which is called non-targeted remodeling and the second that it is targeted toward specific sites [45, 46, 47, 48, 39]. However, how the bone cells know what they have to do is unknown. In the following the remodeling process is explained in trabecular bone together with the terms used in the mathematical model in section 2.3.3. Additionally the remodeling process is explained for cortical bone since this process is investigated with respect to the nutrient supply of the bone in the last chapter of the thesis (see chapter 5).

On the surface of a trabecular strut cells are activated to turn into resorbing cells, the so-called osteoclasts [49]. At this site they start to remove bone by building an acidic environment and probably dissolve first the mineral and then digest the collagen [50, 49, 51]. The osteoclasts create a resorption lacuna within 2-4 weeks. After resorption the bone forming cells, the osteoblasts, are activated [52]. The time period of this recruitment is termed quiescent period and takes roughly 1-2 weeks [52]. The osteoblast refill the lacuna with (lamellar) bone [53] which takes roughly 2-6 month [52, 54]. The new deposited bone starts to mineralize during the mineralization process, where mineral is incorporated in the collagen matrix (see section 2.2.2).

When cells participating in the remodeling process are acting in a coupled manner, i.e. resorption being followed by formation, they are named the basic multicellular unit (BMU) [55]. The product of the work of a BMU is called bone structural unit (BSU) which corresponds to the bone packet in trabecular and to the osteon in cortical bone. The time the BMUs need to remodel a volume of bone which is equal to the actual trabecular bone volume is called turnover time. In humans this turnover time is approximately 5 years [56].

In healthy individuals equal volumes are removed and formed during the remodeling

process. Roughly 10^6 active BMUs first resorb and then form bone simultaneously in the human skeleton [54]. The so-called remodeling space, which includes the volume of resorbing and forming cavities, varies with the number of active BMUs [57]. The amount of active BMUs increases from age 35 to age 60 which leads to a decrease of bone volume [58]. Lack of hormones after menopause further increases the number of BMUs and the loss of bone is even more drastic. Such an increase in BMUs is also called increased turnover, analogously decreased turnover for a decreased number of BMUs. The loss

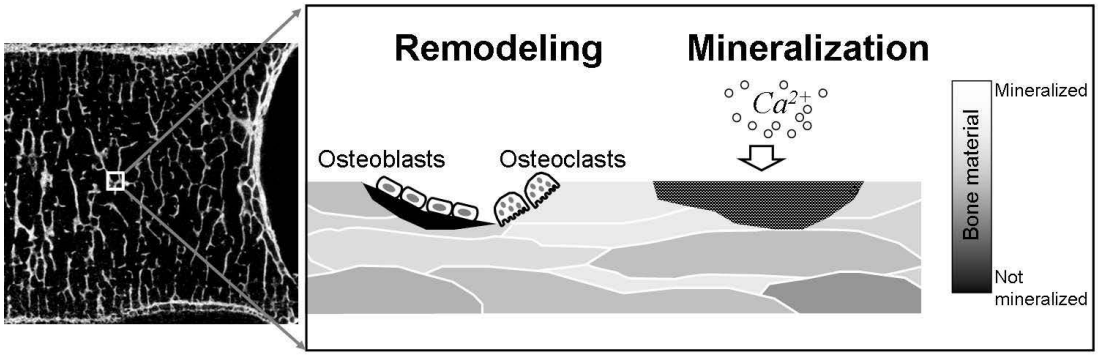

Figure 2.3: Left, the network of trabecular bone inside a human vertebra. Right, schematic zoom on one trabecula (strut). The trabecula consists of packets with different mineral content. This material heterogeneity is the result of bone remodeling and mineralization. During remodeling, a packet of old bone is resorbed from the surface by osteoclasts and new unmineralized bone is deposited by osteoblasts. (From [59] with permission from Springer Science.)

of bone observed during osteoporosis is induced by an increased turnover scenario [60]. In the literature the increased loss of bone is also referred to as the extension of the remodeling space [61, 62].

In cortical bone the osteoclasts drill a canal through the cortex [53]. The drilled canal is shaped like a cone, the so-called cutting cone with active osteoclasts at its tip. The osteoblasts refill the cone by producing collagen which is deposited in concentric layers as bone lamellae. The deposition continues until a small canal for the blood vessel remains in the middle [53]. Some osteoblasts are buried in the lamellae and form osteocytes [63] which are connected to each other by little channels, called canaliculi. The dense network of osteocytes reflects the orientation of the collagen [64]. The osteocytes probably sense mechanical stimuli [65, 66], transfer it to the environment and control the remodeling process [67]. To fulfill this task they have to be well supplied with nutrients. How the cortical bone manages to keep the osteocytes alive is investigated by quantifying the

arrangement of osteons in the cortical bone of horses in section 5.

2.2.2 Bone mineralization

The mineralization process starts after deposition of new bone. The mineralization process leads to a stiffening of the soft collagen matrix. The amount of mineral is beside the material properties of the organic matrix one important determinant that contributes to the stiffness of the bone material [9]. The influence of a disturbed mineralization process on the bone material is studied in section 3.3 and how the mineralization can be measured *in vivo* is presented in section 4. Therefore the mineralization process is described in more detail in the following.

The current understanding of the initial steps which lead to the mineralization of the new deposited collagen is that mineral clusters are formed in the surrounding fluid and are believed to bind to distinct regions in the collagen matrix [68]. In *in vitro* studies it was demonstrated that this binding is the result of electrostatic interaction between the positively charged gaps and the negatively charged clusters. Once arrived in the matrix, the clusters diffuse through its fibrils [69] and solidify into an amorphous mineral phase with the help of the collagen [70]. Later the amorphous phase crystallizes into carbonated hydroxyapatite[1] [68]. This mechanism is possibly similar *in vivo* since the amorphous mineral phase is found in zebra fish fin bones [71, 72] and in tooth enamel [73]. An alternative theory is that, ions from the surrounding fluid could 'travel' through bone forming cells which place them at the final deposition site in the bone [74, 75]. Yet the ongoing processes in the cell are unknown.

Most organisms (invertebrates) use calcium carbonate[2], not apatite [76]. Why apatite is used to mineralize vertebrates is unknown [77]. It presumably suits the functional demand, like for example in teeth dentin where apatite platelets are tightly controlled to match and redistribute chewing forces [78]. A different orientation is also observed at the bone/cartilage interface (e.g. intervertebral disk and vertebra). The mineral particles are aligned perpendicular to the interface in the cartilage and parallel to it in bone suggesting a mechanical role for the two elastically different materials [79]. Recently it was found in the mandible of a crayfish that apatite oriented normal to the surface covers a softer base which is reinforced with amorphous calcium carbonate and phosphate [80]. The combination of apatite and amorphous minerals in this animal leads to a hardness profile similar to mammalian teeth.

In bone approximately 70% of the total mineral content of a bone packet is reached in

[1] Hydroxyaptite: $Ca_5(PO_4)_3(OH)$
[2] Calcium carbonate: $CaCO_3$

the first days to weeks. In the following months the crystals grow and the bone packets increase further their mineral content [81]. The fast increase in mineral content followed by slower increase is known as primary and secondary mineralization and was quantified by a mineralization law [14]. The mineralization law relates the mineral content of a bone packet to its age (see also Figure 2.6 in section 2.3.3). In young bone the increase in calcium is large, while in older bone packets it is much slower.
The mineralization process can be disturbed during bone diseases such as osteomalacia[3] which reveals a decreased amount of mineral while the collagen matrix is believed to remain unchanged [82] and/or the amount of collagen is slightly increased [5]. In osteogenesis imperfecta[4] the mineral crystals become thinner and less well aligned with age (as shown in a mouse model). These changes of the crystal presumably contribute to the brittleness of the bone, as measured with small angle X-ray scattering and quantitative backscattered electron imaging (qBEI) [83, 84]. Osteoporosis is mostly related to an increased turnover scenario which leads to a less mineralized bone [6]. Recently it was shown (with qBEI) that the osteoporotic bone material reveals a large variety of differently mineralized areas at fracture sites [85]. How the mineralization process is disturbed during osteoporosis is not well known [8].
Drugs against osteoporosis can influence the remodeling and/or the mineralization process. A relatively new drug against osteoporosis is Strontium ranelate. This drug probably decreases the bone turnover and during the mineralization process 5% of the calcium atoms are substiuted by the larger strontium atoms [86]. Strontium has a larger atomic number than calicum. In backscattered electron imaging more electrons are backscattered from the Sr atoms than from the Ca atoms which leads to a 'brighter image'(see section 2.3.1). It seems that the collagen matrix is filled faster with mineral simply because the strontium is embedded in the matrix. Yet the kinetics of the mineralization process in the matrix is unchanged, i.e. the thickness and length of the mineral platelets are not affected during the treatment [87].
In section 2.3.1 methods are presented which can be used to quantify the spatial heterogeneity of the mineral content in trabecular bone.

2.2.3 Theories and computer models of dynamic processes in bone

Until now it is widely accepted that the structure of trabecular bone is the result of a load adaptive process. A quantitative formulation in terms of mathematical laws that relate the remodeling and the mineralization process to local stress and strain is still

[3] Osteomalacia is called rickets in children and is related to softening and deformation of the bone.
[4] OI leads to a stiffening of the skeleton and is known as brittle bone disease

missing. Yet many attempts have been made to quantify these processes in trabecular bone by assuming such remodeling rules and simulate the pattern formation of a homogeneous material [88, 89, 90, 91].
The first qualitative formulation of structural adaptation to mechanical stimuli was first proposed in the 19th century [37, 38]. The paradigm that bone is formed where mechanically need and resorbed where there is no need became known as the Wolff-Roux law [37, 38]. Further, Thompson pointed out that a "condition of strain [...] is a direct stimulus to growth" [92]. Based on these ideas Frost introduced a minimum effective strain threshold, which must be reached before bone adaptation starts. He called the mechanically controlled feedback loop a 'mechanostat' [93]. The question to be asked is how the mechanical control of the adaptation can be implemented in the biological system bone [94].
In most of the presented models in literature, the architecture of trabecular bone is simulated by application of external loading on the bone and considering different local control rules by mechanosensing cells [88, 95, 96, 97]. The implemented control rules inducing bone remodeling follow the idea of Frost's mechanostat. This means remodeling is considered as active over and inactive below a chosen threshold value which is given by simulated strain or stress values. The outcome of such a study is a loose agreement of the orientation of the evolving architecture and the orientation of the externally applied forces when a homogeneous material is assumed [88]. The mechanical stimulus is besides biochemical reactions, not the only influence on the cells. Introducing probabilities for bone deposition and bone resorption seems appropriate to consider the different influences [90, 91, 98]. In the simulations the trabecular architecture changed by losing struts and by thickening of the remaining ones [90, 91].
In the previous mentioned studies the mineral content plays only a minor role, although it is a main contributor to the stiffness of the bone material [9]. A relatively new technique is micro-computed tomography (micro-CT)(see also section 2.4.1) which allows not only detecting the architecture of trabecular bone *in vivo* [11] but also to get information about its mineral content [12]. This technique is combined with finite element analysis to relate the mineral content to the corresponding stress and strain values in the trabecular architecture [99].
With time not only the architecture of the bone changes but also the material due to the mineralization process. A mathematical quantification of this process in trabecular bone was found only recently. The relation between the age and the mineral content of a bone packet in trabecular bone became known as the mineralization law [14]. This law is the outcome of a continuity equation that relates the remodeling and the mineraliza-

tion process at a material level. The model could validate the outcome of a treatment against osteoporosis [10]. Considering the mineralization law together with stochastic remodeling rules in a simulation resulted in a mineral distribution that could successfully compared to experimental results [98]. In the following it is explained how this mineral distribution is measured together with the mathematical formulation of the model since it is used in section 3.3.

2.3 Quantification of the dynamic processes in trabecular bone

2.3.1 Quantitative backscattered electron imaging (qBEI) on human trabecular bone

The different mineral contents of the bone packets in trabecular bone are experimentally accessible by quantitative micro radiography (qMR) [100, 101, 102], synchrotron radiation micro-computed tomography (SRμCT) [103, 104] and quantitative backscattered electron imaging (qBEI) using a scanning electron microscope [105, 106, 107, 108, 109]. All these methods are invasive and require bone biopsies or autopsies[5]. In qMR the two-dimensional bone samples are usually 100 μm thick and are irradiated with a soft X-ray beam which is absorbed by the bone sample. The heterogeneity is evaluated by measuring the distribution of the X-ray attenuation in the pixels of the microradiograph within the plane of a bone sample. The resolution of qMR is around 2.6 μm. But due to the relatively thick samples artifacts occur coming from projection errors [110]. In SRμCT, monochromatic X-ray beams from a synchrotron source are transmitted through a three-dimensional bone sample. Due to the monochromaticity of the beam a direct conversion from the attenuation coefficient, represented by gray levels in the image, to mineral content is possible. This method is rather new and continuously developed in the last years. Its resolution increased from 10 μm [111, 112, 113] to 1.4 μm [103, 104]. The drawback of this method is the rather small sample size ($2 \times 2 \times 2\ mm^3$ at most). With a resolution down to 1 μm, qBEI is the best validated approach to quantify the mineral heterogeneity of the bone material [114]. This method is discussed in more detail since the influence of the stochastic backscattering process of the electrons on the measured result is characterized and mathematically described in section 3.1. In qBEI a bone sample of several square centimeters is scanned with an electron beam. Roughly 30% of the incident electrons are elastically backscattered from the surface. These electrons are referred to as backscattered electrons (BE) when the electron trajectory is changed by

[5] sample surgically removed from a living (biopsy) or dead (autopsy) subject

more than 90° from the initial direction of motion, i.e. the electron scatters back into the hemisphere of the original beam [115]. The electrons being backscattered from each

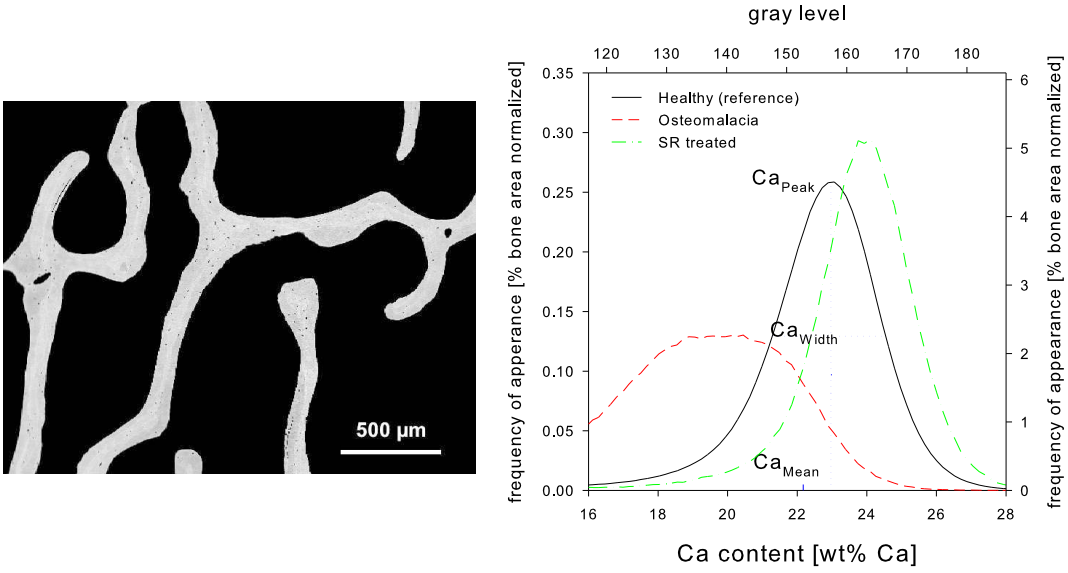

Figure 2.4: Bone mineralization density distribution (BMDD, see section 2.3.2) (right) obtained from a qBEI image (left, courtesy of P. Roschger) of trabecular bone after conversion from gray level into calcium content. The BMDD is constant for healthy adults and deviation from this reference (black) are detected for osteomalacia (red). The BMDD (green) obtained after treatment against osteoporosis with Strontium ranelate is shown depending on gray level (top x-axis). For the conversion from gray level in calcium content see text and section 3.3.3.

beam position on the sample, are detected and the intensity is converted into a gray value. After the entire scanning of the sample, a gray level image is obtained, see Figure 2.4 left. A gray level of a sample area within the image reflects either a pure element with a certain atomic number Z or a material being composed of several elements having an averaged atomic number (Z_{mean}). The backscattering coefficient η for homogeneous samples is the fraction of BE divided by the incident electron beam. The coefficient increases monotonically with an increase of the atomic number. This dependence is known as Z contrast. A sample being a mixture of homogeneous elements, η is approximately the sum of the individual constituents weighted by their mass concentration C_i (namely the weight percent wt% of the i-th atom)

$$\eta = \sum_i C_i \eta_i \tag{2.1}$$

where i denotes each constituent [115].
In a bone sample, the element calcium dominates the influence on the backscattered electrons since it is the element with the largest atomic number, among the organic matrix consisting of the elements H, C, N, O, S. The mineral hydroxyapatite is made of the elements P, O, H beside Ca. A calibration is necessary to convert the BE signal represented by gray levels into calcium content given as wt%. Roschger et al. use the material contrast of carbon (Z = 6) and aluminum (Z = 13). They determine the gray levels of the elements by adjusting the detector such that for carbon a gray value of $GL_C = 25$ and $GL_{Al} = 225$ for aluminum is obtained. The gray level for bone lies between these values. The outcome is a linear correlation between the BE gray level and the calcium concentration, $GL_{qBEI} = \frac{Ca[wt\%]+4.332}{0.1733}$ [114]. To validate the calibration the bone sample was additionally measured by quantitative energy dispersive X-ray (EDX). Areas in the bone sample showing distinct gray levels in the qBEI image are picked to analyse the corresponding element composition. The measured frequency of the appearing elements, which is mostly calcium, corresponds to the gray level.
The drawback of qBEI is the finite acquisition time. The backscattering of electrons is a stochastic process. Only an infinite acquisition time would give an accurate result. This is obviously not possible for practical reasons, but a too long acquisition time would induce significant damage to the bone tissue. In section 3.1 a mathematical solution is given to overcome this limitation.

2.3.2 The bone mineralization density distribution (BMDD)

By the use of quantified BEI, histograms of the gray level images return a frequency distribution of the calcium content in the bone sample. The normalized frequency distribution of these images is called the bone mineralization density distribution (BMDD) [114]. The BMDD quantifies the probability to find bone with a given mineral content in a bone sample. Since the BMDD is usually a bell-shaped curve, it can be characterized by its peak position, Ca_{Peak}, and the peak width defined as full width at half maximum, Ca_{Width} (see Figure 2.4). In healthy human adults the BMDD is independent of sex, age, ethnicity and anatomical site [108]. This allows the definition of a reference BMDD for healthy individuals. The BMDD deviates from the healthy state when the bone is affected by various bone diseases like osteoporosis [116] and osteomalacia [108] (see Figure 2.4 right). Further deviations appear when the bone disease is treated with different drugs against osteoporosis like, e.g. parathyroid hormones (PTH) [117], bisphosphonates [118] or strontium ranelate [86, 87]. Thus the deviation from the reference BMDD serves as an important diagnostic indicator [6]. Predictions about the temporal changes in the

BMDD can be obtained with computer models, which therefore allow interpreting the observed deviations from the reference BMDD.
Usually osteoporosis is diagnosed by measuring the bone mineral density (BMD) of a given bone volume. Despite the similarity in the abbreviation the BMDD must not be confused with this quantity. The BMD is a single scalar that depends on the bone volume and the mean mineral content and is measured in a X-ray absorption experiment. The BMDD is a probability distribution that returns variations of local calcium concentrations in trabecular bone at the micrometer level. Yet the BMD and BMDD can be correlated by calculating the mean value of the BMDD in units of volume percent of hydroxyapatite. Multiplication of the mean value by the density of the mineral and the bone volume returns the volumetric BMD (vBMD) [119].
Concerns were raised about the validity of BMDD representing the true mineral distribution in bone. The main objections were that the BMDD changes its width with varying electronic beam currents [120]. The electron backscattering event is a stochastic process occurring with a certain probability. Therefore, probing an ideally homogeneous sample (consisting of only one Z) leads to a distribution of finite width of gray levels instead of an ideal δ-distribution. This effect together with the electronic noise from the instrument compromise the measured BMDD. Since the noise influences mostly the width of the peak, the "true" BMDD is obtained by deconvolution of the measured one. In a response [121] to the raised concerns it was estimated that under the standardized experimental conditions, the measured peak width of the BMDD would be no more than 5% apart from the width of the "true" BMDD.
To quantitatively understand the influence of the finite measurement time the BMDD is deconvolved in section 3 by the use of regularization methods. The deconvolved BMDD is further used as input of the mathematical model introduced in the next section (2.3.3) and for the model in section 3.3. The simulation outcomes are at the end 're-convolved' to allow for a better comparison between simulation and measurements.

2.3.3 The BMDD model

The bone mineralization density distribution (BMDD) is used in a mathematical model describing the material changes in trabecular bone [14]. The bell-shaped distribution is the result of the mineralization and the remodeling process and is similar for healthy humans. Since this model is used to study an increased/decreased mineralization kinetics on the BMDD (chapter 3) it is described here.
The remodeling and mineralization influence the BMDD in two different ways [10]. First, the action of the osteoclasts reduces the mineralized bone volume which results in a

lowering of the peak, see Figure 2.5 left. After a certain period, the quiescent period, the osteoblasts lay down new bone. This initially unmineralized bone is considered at zero mineral content and enters therefore at the left side of the BMDD. Second, during the mineralization process the bone packets continuously increase their mineral content, which leads to shift of the BMDD to higher values, see Figure 2.5 right. The temporal

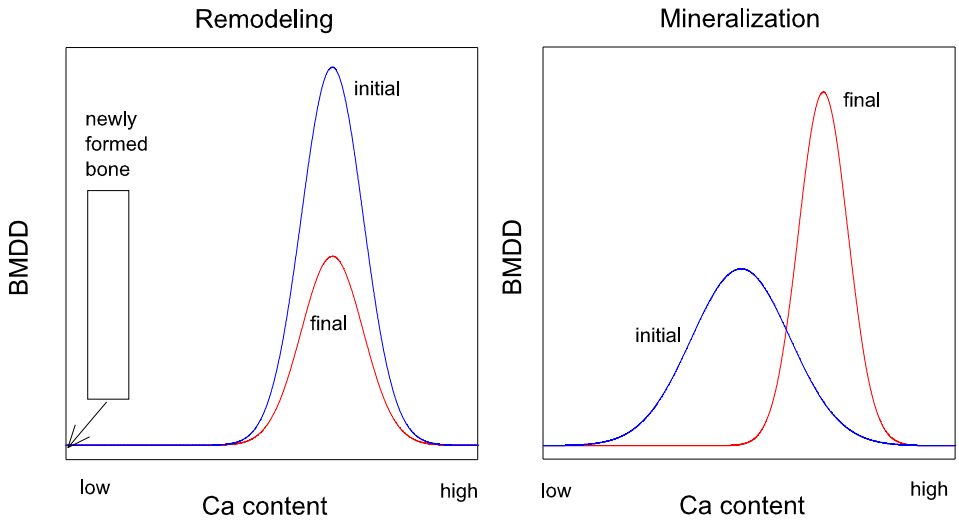

Figure 2.5: Schematic effect of the remodeling (left) and the mineralization (right) process on the BMDD. Bone resorption leads to lowering of the peak while bone deposition is considered as new unmineralized bone that enters at zero calcium content. The mineralization process leads to a right shift of the BMDD.

change of the BMDD is described by a continuity equation (2.3) which considers the mineralization and the remodeling process. The BMDD is given as a function $\rho(c,t)$ denoting the bone volume with a calcium content c within $[c, c+dc]$ at time t. The total bone volume at time t, is therefore $BV(t) = \int_0^{c_{max}} \rho(c,t)dc$ where c_{max} denotes the maximum concentration of calcium found in bone. The simulations start from a normalized initial condition with $BV(t=0) = 1$, but BV can change during simulations. Since the measured BMDD is normalized to 100% of mineralized area, the quantity $\rho(c,t)/BV(t)$ is used for comparison between simulation and experiment.
The remodeling process is considered by a sink of bone volume, $j_{Rs}(t)$ corresponding to resorption, and a source $j_F(t)$ corresponding to deposition, such that the change of bone volume BV with time is $\frac{d}{dt}BV(t) = \frac{d}{dt}\int_0^{c_{max}} \rho(c,t) = j_F(t) - j_{Rs}(t)$. Bone resorption is assumed to be independent of the calcium content c, therefore $j_{Rs}(t)$ is normalized by $\frac{\rho(c,t)}{BV(t)}$. Newly deposited bone is always non-mineralized. Therefore bone deposition

defines the boundary condition at $c = 0$. The mineralization kinetic is modeled by a mineralization law, $m(a)$ [14]. It relates the mineral content of a bone packet to its age a, see Figure 2.6. The mineralization law is a strictly monotonous function and

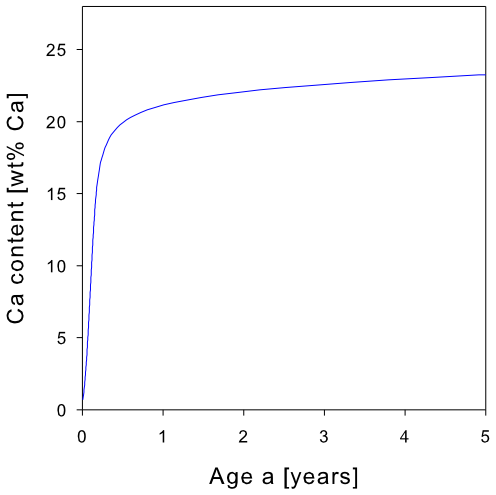

Figure 2.6: Mineralization law of a healthy bone packet connecting the calcium content to its age. The mineralization law is the result of equation 2.4.

therefore invertible. Consequently, the mineralization velocity $v(c)$ entering the time evolution equation of the BMDD, is $v(c) = \frac{d}{da}m(a)$. The time evolution of the BMDD finally is the following partial differential equation including the mineralization and the remodeling process:

$$\frac{\partial \rho(c,t)}{\partial t} = -\underbrace{\frac{\partial}{\partial c}[\rho(c,t)v(c)]}_{mineralization} - \underbrace{j_{Rs}(t)\frac{\rho(c,t)}{BV(t)}}_{remodeling}, \tag{2.2}$$

$$\rho(c=0,t)v(c=0) = j_F(t). \tag{2.3}$$

The model can be solved numerically for situations where the bone turnover, i.e. both the rate of resorbed and deposited bone volume, changes in time. Introducing only a single time constant t_{EFF}, these changes can be approximated by an exponential function, $j(t) = j^{final} + (j^{initial} - j^{final})exp(-t/t_{EFF})$. The BMU picture of the remodeling process (see section 2.2.1) is included by precedence of resorption before the corresponding changes in deposition [10]. To predict the time evolution of the BMDD, an initial BMDD $\rho(c, t = 0)$, initial and final values for $j_{Rs}(t)$ and $j_F(t)$, and the time constant of the changes, t_{EFF}, has to be known from experiment or be assumed [14].

The measured reference BMDD, which is the input for this model, is independent of anatomical site, sex, ethnicity and age in healthy human adults [108]. In the model the remodeling and the mineralization process are balanced in such a way that the shape of the BMDD remains unchanged in the healthy case. A reference BMDD independent of time can be interpreted as a steady-state of equations 2.2 and 2.3. With all the time dependencies disappearing, equations 2.2 and 2.3 can be solved in two ways [14]. First for a known BMDD the mineralization law is obtained

$$m^{-1}(c) = -t_{TO}\ln\left(\int_{c}^{c_{max}} \rho(c')dc'\right), \tag{2.4}$$

where t_{TO} corresponds to the turnover time. Second for a known mineralization law a steady-state BMDD can be calculated by

$$\rho(c) = -BV\frac{d}{dc}exp\left(-\frac{j}{BV}m^{-1}(c)\right). \tag{2.5}$$

In the simulation the value j is related to the turnover time t_{TO} by $j = \frac{BV}{t_{TO}}/year$. In the healthy case one unit volume is remodeled. When choosing a turnover time of $t_{TO} = 5y$ it means that 20% of the bone volume is remodeled per year. By changing j in equation (2.5), BMDDs are obtained which correspond the steady state reached after a change in the remodeling process. For a four times increased turnover, e.g., four times more bone volume is remodeled than in the healthy case, i.e. $j = 4\frac{BV}{t_{TO}}/year = \frac{BV}{1/4t_{TO}}/year$. Thus in equation (2.5) the value $j = 0.25$ has to be chosen to simulate a four times increase turnover. The effect on the steady state BMDDs resulting from a change in turnover were studied in [14]. They are adapted in chapter 3.3 to compare these results to effects resulting from a change in the mineralization kinetics.

2.4 Experimental data used in this work

2.4.1 Time-lapsed *in vivo* micro-computed tomography on mouse bone

Using *in vivo* micro-computed tomography (micro-CT) the same bone can be imaged in three dimensions at different time points in small animals like mice. By comparing two consecutive images, changes in the bone structure can be detected.
The setup used for micro-CT is usually an X-ray source and a detector at a fixed position where in between the investigated object is rotated around its long axis. At each angular adjustment the sample is penetrated by the X-rays resulting in a two-dimensional projec-

tion (or scan) of the image. The beam intensity is exponentially attenuated depending on the material, the penetrating distance and the energy spectrum of the X-ray source. This material constant, i.e. the attenuation coefficient, is defined as linear absorption coefficient and describes how much the beam is attenuated after passing an infinitely small distance. The measured final attenuation is the sum of all the local coefficients. The detected intensity is converted in a gray value. After a full rotation of the object, the two-dimensional scans can be used to reconstruct a three-dimensional gray level image representing the linear attenuation coefficients [122].
The gray level intensities of the μCT scans include additional information about the local mineral content [123]. However, the conversion from gray levels into mineral content is not straightforward using polychromatic X-rays of a conventional μCT. Lower energies are absorbed more by the sample than higher energies. The energy spectrum of the beam is not only lowered but shifts its peak to higher values. This effect is known as beam hardening [124] and can be reduced by placing filters in the X-ray path [125] or by applying correction algorithms to the images [126, 127]. The calibrations of varying hydroxyapatite concentrations allow an interpretation of the gray levels in terms of mineral content [123, 99, 128].
The detailed experimental setup is reported in [129, 130] and is only shortly described here. The sixth vertebra of the mouse tail (standard mouse: C57BL/6) is mechanically loaded with 8N at 10 Hz for 3000 cycles, 3 times per week for 4 weeks. The mechanical stimulus is applied to the vertebra via pins inserted in the neighboring vertebrae (Figure 2.7). In an unloaded control group the steel pins are inserted into the neighboring vertebrae in the same way, but no loading is applied. The control and the loaded group each comprises 9 mice. In both groups the bone structure is determined by weekly scans with *in vivo* micro-CT at a resolution of 10.5 μm in all three spatial dimensions.
The three-dimensional images provided for the analysis of the mineralization process *in vivo* in mice are obtained by the described procedure using a desktop micro-CT with a polychromatic X-rays. During the course of the experiment the very same vertebra of a mouse was investigated over five weeks. The images of the different time points of the same bone are aligned using computational tools [131]. By overlapping the images, regions of bone formation and resorption on the bone surface are identified (Figure 2.7 right). Bone volume present only in the earlier image, but not in the later one is defined as resorbed bone. Bone volume only present in the later images is defined as formed bone. Bone areas present in both images are considered as quiescent, i.e. not remodeled bone. The method was successfully validated in showing good agreement with formation parameters when compared with results from standard techniques (histomorphometry)

[13, 132]. Not only the remodeling rates are investigated with this experiment but also how an external mechanical stimulus influences the rates.
The provided μCT scans are used to investigate the mineralization process and the influence of the mechanical stimulus, Figure 2.7, on it in chapter 4. The heterogeneity in the mineral content is quantified by a frequency distribution, like the BMDD. The evaluation of the gray levels of the images focuses on trabecular bone only.

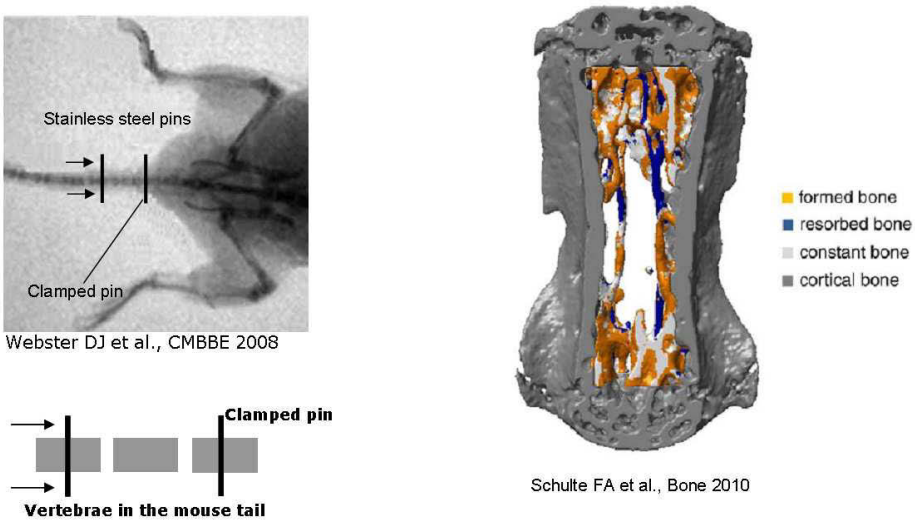

Figure 2.7: Prepared mouse bone and evaluated micro-CT scan. Left: The inserted steel pins in the neighboring vertebrae in the mouse tail are used to mechanically stimulate the middle vertebra. A procedure that is repeated three times a week for four weeks [13]. The middle bone is scan weekly with a micro-CT. Right: The alignment of the weekly scans allows determination of formed (yellow), resorbed (blue) and not remodeled, i.e. constant or quiescent (bright gray) regions.

2.4.2 Light microscopy images of osteonal bone of horses and dogs

In chapter 5 of this thesis an algorithm is presented which quantifies the arrangement of osteons and osteonal canals in cortical bone of horses. With this quantification conclusions about the underlying mechanisms of the remodeling process can be drawn.
Light microscopy images were provided, which were taken from cortical bone sections and which were cut from the middle part of the long bones in horses and dogs. The specific bones are the left radii and the metacarpus of two horses, see Figure 2.8. In

each sample four areas are investigated which are defined by their anatomical direction. The direction towards the head is called cranial and towards the tail caudal. The lateral direction is perpendicular to the cranial or caudal direction pointing away from the animal, while the medial direction points towards the animal, see Figure 2.8.
The images taken by reflective light microscopy of the samples show almost entirely osteonal bone. The investigated sites in the sample cover an area of 5.8 x 4.35 mm^2 at low resolution and 1.415 x 1.06 mm^2 at high resolution. The size and shape of the canals is more precisely defined at high resolution while the larger area captured at low

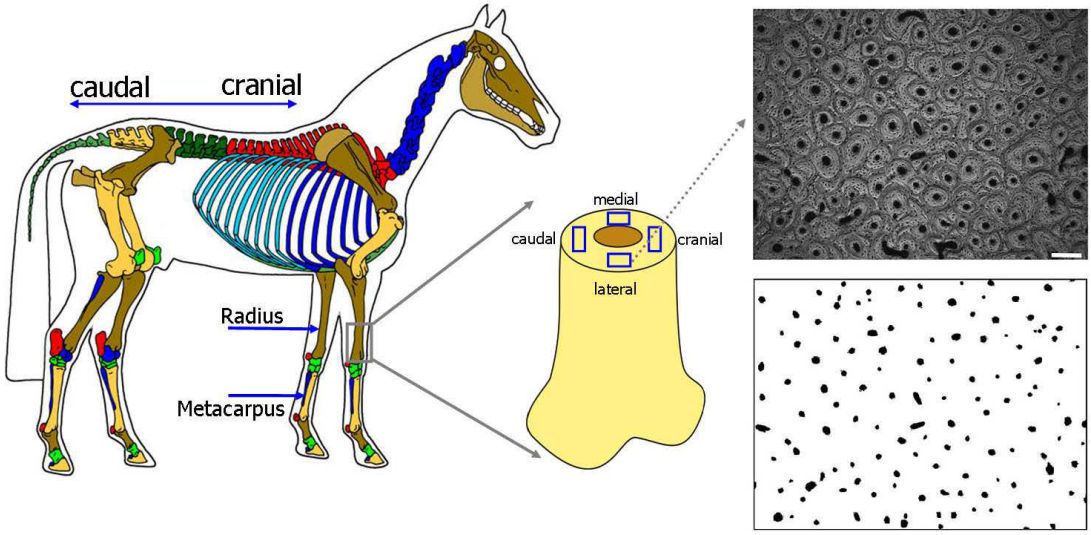

Figure 2.8: Investigated horse bones and corresponding nomenclature. Left: From the horse skeleton only the long bones, i.e. radius and metacarpus are analyzed (skeleton taken from [133]). Middle: Schematic drawing of a cut through a long bone visualizing the specific measurement sites in the study. From these sites images are taken by reflective light microscopy (upper right gray image). The scale bar denotes 250 μm. The lower right image is binarized, where the canal of the osteons is separated from the surrounding bone and is marked as black, while the surrounding is set to white.

resolution is statistically favorable in the analysis of the osteonal arrangement. High resolution and low resolution images are saved in images of a size of 1280 x 960 and 1230 x 890 pixels.
All light microscopy images are converted into binary images, see bottom right image in Figure 2.8. The canals of the osteons are marked in black and the rest is taken as white background. The canals and osteocyte lacunae are distinguished automatically based on their size and circularity using the "particle analysis" tool in the software ImageJ [134].

Remaining artifacts that are not recognized by the software have to be removed by hand. The binarized images are used to determine the spatial arrangement of the canals. The detailed description of the developed algorithm is presented in section 5.

3 Influence of mineralization kinetics and the measurement process on the bone mineralization density distribution (BMDD)

The shape of the measured bone mineralization density distribution (BMDD) can be influenced by several aspects starting with the measurement process and biological factors like bone diseases and drug therapies. In the following chapter a quantification of the different influences is presented, starting with the stochastic backscattering process in quantitative backscattered electron imaging (qBEI). For this purpose a detailed mathematical description of the measurement process is presented which results in an equation relating the measured (finite acquisition time) with the 'true' (infinite acquisition time) BMDD. By deconvolution this true BMDD is obtained from the reference BMDD and serves as input parameter for the simulation in the second part of the chapter.
In this second part we present a model which incorporates changes in the mineralization kinetics in trabecular bone. The model is based on a previously introduced model (see section 2.3.3) which considers the remodeling and the healthy mineralization process to describe changes on the BMDD [14]. The aim is to study the influence of a disturbed mineralization kinetics on the BMDD. These influences on the BMDD are then compared to changes resulting from a decreased/increased remodeling.

3.1 Influence of the measurement process

In this section the mathematical relation between the measured and the 'true' BMDD is derived which was published in [59]. The presented section follows the line of the published text.

3.1.1 Relation between the measured and the actual BMDD

The calculation is started by considering a qBEI experiment (see section 2.3.1) on a homogeneous material. The number of electrons hitting a small region of the sample is denoted as N and n the number of backscattered and detected electrons. N tends towards infinity for an infinitely long acquisition time, t_a. For such an ideal measurement the probability p that the incoming electron is backscattered and detected can be defined as $p = lim_{N\to\infty}\frac{n}{N}$. The probability to find a small region in the sample with a backscattering probability within $[p, p+dp]$ is defined as $f(p)dp$. A homogeneous material with scattering probability p_0 is therefore described by $f_{hom}(p) = \delta(p - p_0)$.
Although the sample is assumed homogeneous, the number of electrons backscattered from a small location on surface differs in a real experiment with finite acquisition time. This is due to the stochastic nature of the backscattering process. The ratio of backscattered and detected electrons to incident electrons is denoted as $x = \frac{n}{N}$. For a real experiment and an assumed homogeneous sample, the probability to find x within $[x - \Delta x/2, x + \Delta x/2]$ is denoted as $g_{hom}(x)\Delta x$. The probability distribution $g_{hom}(x)$ is given by a binomial distribution

$$g_{hom}(x) = N\binom{N}{xN}p^{xN}(1-p)^{(1-x)N} = a(x; N, p). \tag{3.1}$$

The scattering probability distribution of a heterogeneous sample in an ideal experiment is given by $f_{het}(p) = \int_0^1 f_{het}(p')\delta(p - p')dp'$. In a real experiment $g_{het}(x)$ is then the integral over p of the probability $a(x; N, p)$ weighted by the probability $f_{het}(p)$ to find p [121],

$$g_{het}(x) = \int_0^1 a(x; N, p) f_{het}(p)dp. \tag{3.2}$$

In the following only heterogeneous samples are considered, therefore the index *het* is removed. In the further procedure the aim is to solve equation (3.2) for f_{het}. Therefore a relation between the measured gray levels M and the ratio x is needed.
In a qBEI experiment, only a discrete number of different gray levels M is resolved. The detector is adjusted such that the measured gray level M and the fraction of backscattered and detected electrons x are linearly related. This relation is given as $M = ux + v$. Discretizing (3.2) in terms of the gray level M one gets

$$\boldsymbol{g = Af} \qquad or \qquad g_M = \sum_{\overline{M}=1}^{M_{max}} A_{M\overline{M}} f_{\overline{M}} \quad (M, \overline{M} = 1, ..., M_{max}). \tag{3.3}$$

$f_{\overline{M}}$ is defined as the probability to detect a gray level $\overline{M}$ in an idealized experiment with an infinite acquisition time t_a. In contrast, g_M is defined as the probability to detect M in a measurement of acquisition time t_a. The matrix elements $A_{M\overline{M}}$ are approximated as

$$A_{M\overline{M}} = \frac{1}{u} \cdot a(x = \frac{M - v}{u}; N, p = \frac{\overline{M} - v}{u}) \tag{3.4}$$

where the relation between p and mean gray level of the distribution, $\overline{M}$, is used. The matrix $\boldsymbol{A}$ describes the broadening of the intensity of each "true" gray level $\overline{M}$ into the measured gray levels M. In order to approach this broadening the variance of the distribution of (3.4) is calculated. The overall probability for backscattering for bone is roughly 10% [115]. Considering further the size and arrangement of the detector, p decreases by another order of magnitude. Therefore $p << 1$ is a valid assumption and the variance of the distribution can be approximated as

$$b^2(\overline{M}) = \frac{u^2 p(1-p)}{N} \approx \frac{u^2 p}{N} = \frac{u(\overline{M} - v)}{N}. \tag{3.5}$$

In the limit of an infinitely long acquisition time (i.e. $N \to \infty$), $b^2 = 0$, the matrix $\boldsymbol{A}$ becomes the identity matrix and, therefore, $\boldsymbol{g} = \boldsymbol{f}$. Considering the case of trabecular bone, the measured BMDD is then the true BMDD.

The measured BMDD in a qBEI experiment approximates the probability $g(x)$ as long as the measured sample is large enough, i.e. the number of pixels of a BE image, N_{pixel}, must be much larger than the number of gray levels, ($M_{max} << N_{pixel}$). In a typical qBEI experiment the number of different gray levels is $M_{max} = 256$ (8 bit gray scale resolution). The number of electrons hitting a region in the sample can be calculated. Knowing the probe current I and the total acquisition time of the image t_a, N is calculated by $N = \frac{I}{e} t_a \frac{1}{N_{pixel}}$, with e being the elementary charge. The time the electron beam hits a region is $\frac{t_a}{N_{pixel}}$ and one gets $N = \gamma t_a$, with $\gamma = \frac{1}{N_{pixel}} \frac{I}{e}$.

The unknown constants u and v in (3.4)-(3.5) can be determined based on a comparison with qBEI measurements. u and v are both changed by adjusting brightness or contrast [114]. When brightness is increased, u is decreased because the same number of counts is assigned a higher gray level. When contrast is increased, the histogram gets wider, therefore u is increased because there are more counts per bin. v is increased since the smallest gray level is shifted to higher counts.

As mention in section 2.3.1, the brightness and contrast in the SEM are adjusted so that in the range of the 256 gray levels, C and Al have mean gray levels of $\overline{M}_C = 25$ and $\overline{M}_{Al} = 225$. Experiments using different acquisition times t_a showed the linear behavior

expected from (3.5) between the width of the measured distribution and the inverse of the acquisition time,

$$b^2(\overline{M}) = k(\overline{M})\frac{1}{t_a} \tag{3.6}$$

with $k_C = k(\overline{M}_C) = 400$ and $k_{Al} = k(\overline{M}_{Al}) = 822$ [121]. Equating (3.5) and (3.6), results in $u = \gamma\frac{k_{Al}-k_C}{\overline{M}_{Al}-\overline{M}_c}$ and $v = \frac{k_{Al}\overline{M}_C - k_C\overline{M}_{Al}}{k_{Al}-k_C}$.
In the calculation, the material was assumed homogeneous with a fixed, but arbitrary $\overline{M}$. Therefore all the matrix elements $A_{M\overline{M}}$ from (3.3) can be obtained. Their dependence on acquisition time is given by

$$A_{M\overline{M}}(t_a) = \frac{1}{u}\cdot a(x = \frac{M-v}{u}; N = \gamma t_a, p = \frac{\overline{M}-v}{u}). \tag{3.7}$$

For a more intuitive understanding and to relate the results to [121], the binomial distribution is approximated by a Gaussian distribution. This approximation is valid if N is large enough and the conditions $Np > 4$ and $Np(1-p) > 4$ are fulfilled [135]. N is the number of electrons hitting a single location of a sample during the acquisition. When measuring for $t_a = 100s$ with a current $I = 0.11nA$ then N can be calculated by $N = \frac{It_a}{eN_{pixel}} \approx 2\cdot 10^5$. The approximated normal distribution is

$$A_{M\overline{M}}(t_a) = \frac{1}{\sqrt{2\pi\sigma^2}} exp(-\frac{(M-\overline{M})^2}{2\sigma^2}), \tag{3.8}$$

with

$$\sigma^2(t_a, \overline{M}) = \frac{u}{N}(\overline{M}-v) = \frac{2.11s}{t_a}(\overline{M}+164.6),$$

using $u = \gamma(2.11s)$ and $v = -164.6$. In the qBEI experiments, the current was always kept constant, $I = 0.11nA$. An image with $N_{pixel} = 512\times 650$ was recorded resulting in $\gamma = 2.06\cdot 10^3/s$. In the numerical implementation, the matrix $\boldsymbol{A}$ is normalized such that each column sums up to 1. Therefore (3.3) conserves the normalization of $\boldsymbol{f}$ and $\boldsymbol{g}$. Note that the width of the distribution in (3.8) defining the matrix $\boldsymbol{A}$ does not explicitly depend on γ, but only on acquisition time and gray level. For an infinitely long acquisition time, σ tends to zero. Then the matrix $\boldsymbol{A}$ approaches the unit matrix and the difference between the "true" BMDD $\boldsymbol{f}$ and the measured distribution $\boldsymbol{g}$ disappears. The inversion of $\boldsymbol{A}$ to calculate $\boldsymbol{f}$ from $\boldsymbol{g}$ is not straightforward, since the solution is not stable under small perturbations of the measured input data. Such an ill-posed problem can be handled using regularization methods [136, 137]. The Tikhonov regularization is usually the first choice as regularization method and will be applied in the following.

3.1.2 Deconvolution of the BMDD with Tikhonov regularization

The purpose of regularization is to stabilize the ill-posed problem and to single out a useful and stable solution. This is done by incorporating further information about the desired solution by side constraints [137, 136]. In other words, the main idea of regularization in the presented case, is to approximate the solution for $\boldsymbol{f}$ in (3.3) by solving a linear least-squares problem under additional side constraints. Using the Tikhonov method with a simple side constraint, the problem is to find $\boldsymbol{f}_{reg}$ being the minimizer of the weighted combination of the residual norm and the side constraint, such that

$$\boldsymbol{f}_{reg} = argmin\left\{||\boldsymbol{A}\boldsymbol{f} - \boldsymbol{g}||_2^2 + \lambda^2||\boldsymbol{f}||_2^2\right\}. \tag{3.9}$$

While the first term, $||\boldsymbol{A}\boldsymbol{f} - \boldsymbol{g}||_2$, is the residual norm, the second term, $||\boldsymbol{f}||_2$, which obviously has to be small enough, i.e. of small norm not to impose any artifacts and large enough to stabilize the problem. The regularization factor λ acts as a weighting factor between the two terms, and a reasonable result depends crucially on a skillful choice of λ. For a fixed λ (3.9) can be solved explicitly,

$$\boldsymbol{f}_{reg} = (\boldsymbol{A}^T\boldsymbol{A} + \lambda^2\boldsymbol{I})^{-1}\boldsymbol{A}^T\boldsymbol{g}, \tag{3.10}$$

with $\boldsymbol{I}$ being the unit matrix. The effect of λ on the solution $\boldsymbol{f}_{reg}$ can be demonstrated by factorizing $\boldsymbol{A}$ using singular value decomposition [138],

$$\boldsymbol{A} = \boldsymbol{U}\boldsymbol{\Sigma}\boldsymbol{V}^T, \tag{3.11}$$

where $\boldsymbol{U}$ and $\boldsymbol{V}$ are orthogonal and $\boldsymbol{\Sigma}$ is a diagonal matrix with the singular values of $\boldsymbol{A}$ in descending order. The ratio of the largest and smallest singular value is a measure for the invertability of the matrix $\boldsymbol{A}$. For practical acquisition times, the matrix $\boldsymbol{A}$ of (3.7) clearly fails this criterion of invertability.
Inserting (3.11) into (3.10), one obtains

$$\boldsymbol{f}_{reg} = \boldsymbol{V}\boldsymbol{D}\boldsymbol{U}^T\boldsymbol{g}, \tag{3.12}$$

where $\boldsymbol{D}$ is again a diagonal matrix with values $D_{ii} = \frac{\sigma_i}{\sigma_i^2+\lambda^2}$. The effect of λ is therefore to "mitigate" the small singular values of $\boldsymbol{A}$ at the cost of introducing a regularization error.
Plotting the residual norm $||\boldsymbol{A}\boldsymbol{f} - \boldsymbol{g}||_2$ versus the side constraint $||\boldsymbol{f}||_2$ on a double logarithmic scale, the so-called L-curve is obtained (Figure 3.1). If λ is small (vertical

branch), the error is dominated by the large norm of the solution. For large λ (horizontal branch), the error is dominated by the residual norm. The minimum as formulated in (3.9) is obtained by choosing λ in the corner of the L-curve.

3.2 Effects of the deconvolution on the reference BMDD

3.2.1 Deconvolved reference BMDD

The Tikhonov regularization method ((3.10)-(3.12)) is applied to deconvolve the reference BMDD. Figure 3.1 top shows the corresponding L-curve, with the balance between the error of the solution on the x-axis and the norm of the solution on the y-axis. Since a choice of the regularization parameter λ at the corner of the L-curve ($\lambda = 1.5 \cdot 10^{-3}$) results in unrealistic oscillations in the deconvolved reference BMDD, a slightly larger λ is chosen ($\lambda = 3.36 \cdot 10^{-2}$). The main parameters characterizing the BMDD, the position of the peak, Ca_{Peak}, and the width of the distribution, Ca_{Width}, are robust with regard to the choice of λ. An increase or decrease of λ by 50% results in a change of Ca_{Width} of less than 0.3% (Figure 3.1 top inset).
The deconvolved reference BMDD (Figure 3.1 bottom left) is again a bell-shaped distribution with a virtually unchanged peak position. Differences, however, can be seen in the width of the distribution, the deconvolved BMDD naturally being narrower. Since Ca_{Width} is defined as full width at half maximum, it decreases by 7.3% mainly due to an increase of the maximum height by 5.7%. From a given BMDD, one can calculate the mineralization kinetics using equation (2.4). Insertion of the deconvolved reference BMDD instead of the reference BMDD in equation (2.4), slightly different mineralization laws are obtained, see Figure 3.1 bottom right. The difference between the deconvolved and the reference law at an age $a = 1$ y is 0.07 wt% Ca.

3.2.2 Effect of different acquisition times on the measured and calculated BMDD

The reference BMDD can be calculated with $refBMDD(t_a) = \boldsymbol{A}(t_a) refBMDD(t_a \rightarrow \infty)$ for different acquisition times when the deconvolved reference BMDD and the matrix $\boldsymbol{A}$ (3.4) are known. Convolution with $\boldsymbol{A}(t_a = 100s)$ accurately reproduces the experimental reference BMDD as defined in [108]. This confirms that the proposed numerical deconvolution is a good approximation of the true inversion of $\boldsymbol{A}$. The error introduced by the regularization is small. The Figure 3.2 shows the BMDDs measured (left) with different acquisition times. With shorter acquisition time the measured distributions

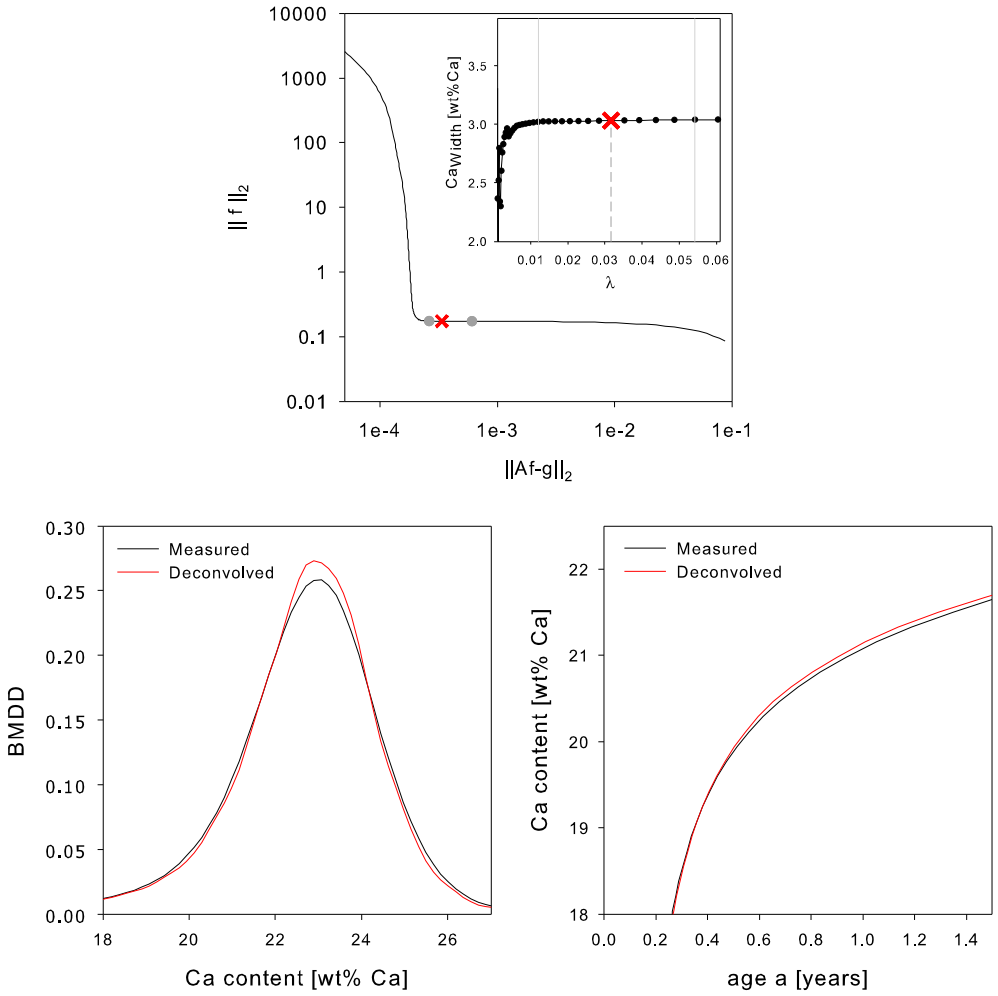

Figure 3.1: Choice of regularization parameter and corresponding distribution and mineralization law. Top: L-curve of the Tikhonov regularization method to deconvolve the measured reference BMDD. In the double-logarithmic plot the norm of the residual and the norm of the side constraint is plotted on the x and y-axis, respectively (see (3.10)). The regularization parameter λ is chosen a bit larger than the corner parameter to obtain a smooth deconvolved curve. The inset shows that the width of the deconvolved reference BMDD is robust against the choice of λ. Bottom left: The measured reference BMDD (black) and the resulting deconvolved distribution after application of the Tikhonov regularization method (red). The corresponding mineralization laws describing the increase in the mineral content in newly formed bone as function of the age of the bone. Plots are adapted from [59] with permission from Springer Science.

have a more wiggly appearance due to a deteriorated signal to noise ratio. According to the considerations above, the BMDDs become broader when the acquisition time is reduced. Figure 3.2 right shows the predicted distributions for different acquisition times. Comparison with the experimental results reveals good quantitative agreement. Only the effect of noise is absent in the calculations, which results in smoother predicted distributions. Note that the effect of t_a on Ca_{Width} is asymmetric: increasing $t_a = 100$ s by a factor of 10 then Ca_{Width} decreases by only 6.4%, while a decrease of t_a by a factor of 10 broadens the distribution by 44%.

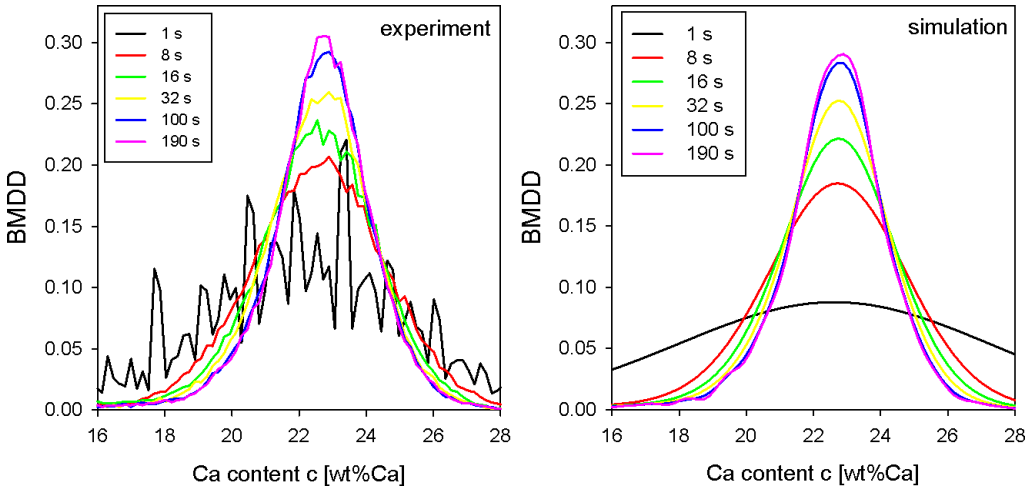

Figure 3.2: Influence of the acquisition time on measured and simulated BMDDs. For the calculation, the deconvolved reference BMDD was convolved with the matrix $\boldsymbol{A}$ (3.8) describing the compromising effect of the measurement. From [59] with permission.

3.2.3 Influence of interindividual variability on the definition of the reference BMDD

The reference BMDD for healthy adults is obtained by averaging over 52 BMDDs from samples taken at different skeletal sites and from individuals of different age, sex, and ethnicity [108]. In order to distinguish the effects of averaging and counting statistics, first all 52 individual BMDDs are deconvolved and then averaged instead of deconvolving the averaged reference BMDD as described above. For deconvolution, the Tikhonov regularization method is again used. The regularization factors have to be chosen individually for each deconvolution from the interval [0.0392; 0.1037]. The effect on the main BMDD parameters Ca_{Width} and Ca_{Peak} is shown in Figure 3.3. While decon-

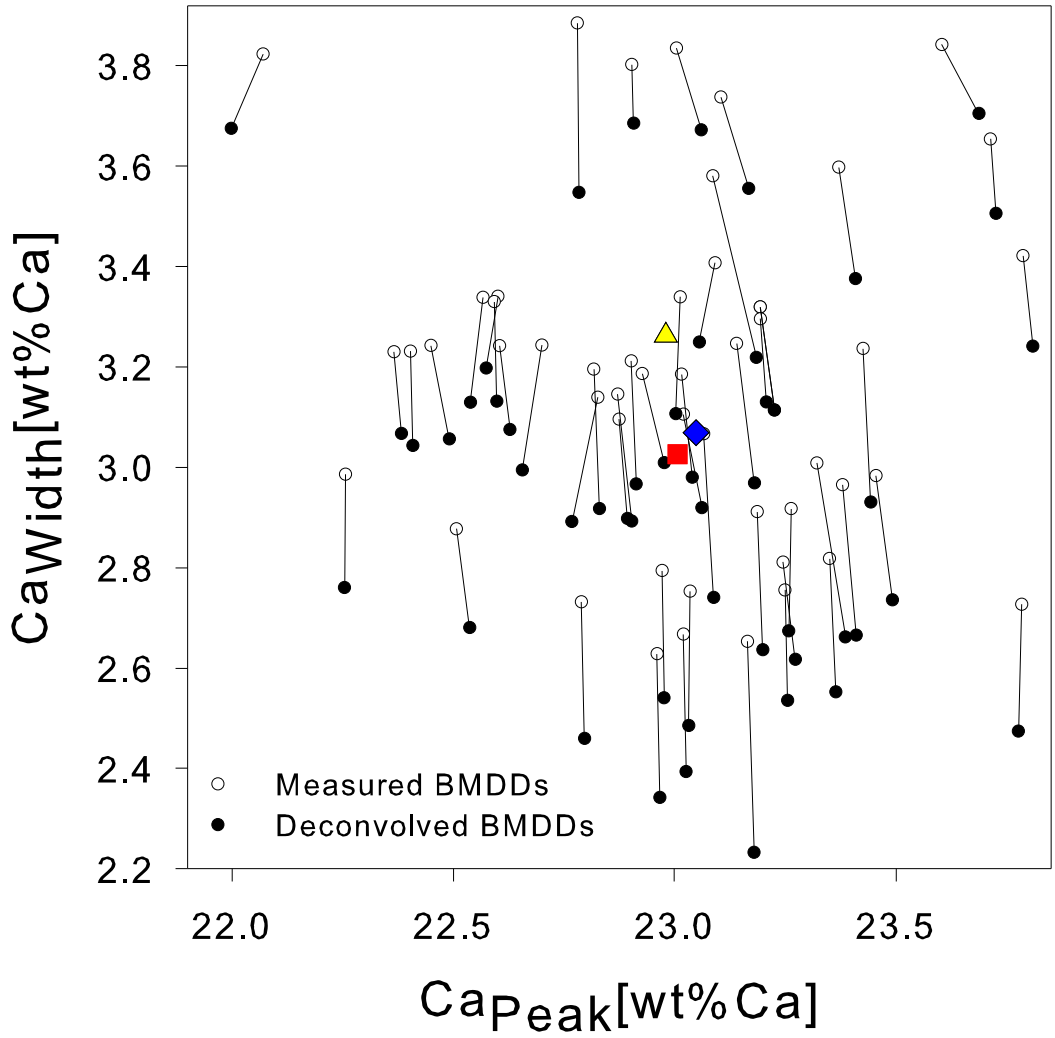

Figure 3.3: Parameters Ca_{Peak} and Ca_{Width} of all the 52 BMDDs from healthy adults of different age, sex and ethnicity, used to define the reference BMDD of healthy adults. Open circles correspond to parameters before deconvolution, full circles afterwards. Larger symbols denote Ca_{Peak} and Ca_{Width} for the reference BMDD (triangle), for the deconvolved reference BMDD (square) and for the BMDD obtained by averaging over all 52 deconvolved BMDDs (diamond). The star gives the mean value calculated by averaging the parameters of the 52 BMDDs. Adapted from [59] with permission.

volution leaves the peak position Ca_{Peak} virtually unchanged, Ca_{Width} is reduced on average by 0.2 wt% Ca. The resulting distribution hardly depends on whether the 52 BMDDs are first averaged and then deconvolved, or whether each of the 52 BMDDs is deconvolved and then averaged. The two possibilities denoted by a full square and diamond, respectively, are found close together in Figure 3.3.

3.3 Influence of disturbed mineralization kinetics on the BMDD

In this section a method to incorporate a disturbed mineralization kinetics in the BMDD model (see section 2.3.3) is presented. The aim of this part of the thesis is to distinguish the resulting influences on the BMDD from influences resulting from a disturbed remodeling process. Disturbed mineralization kinetics occur during bone diseases, drug treatment (see section 2.3.2) and diseases of the endocrine system[1], resulting e.g. in a lack of calcium and phosphate in the blood.
In the model the kinetics is disturbed by modifying the mineralization kinetics. The modified mineralization velocity is then inserted in the BMDD model which is solved numerically. The comparison between the effects on the BMDD originating from disturbed mineralization kinetics and a disturbed remodeling process is presented in two ways. First the behavior of the BMDD parameters (Ca_{Peak}, Ca_{Mean} and Ca_{Width}) in the steady state condition are shown which are obtained for differently 'strong' disturbances in both processes. Second, the time evolution of the BMDD is presented by showing the transients when the BMDD shifts either to higher or lower mineral contents compared to the reference BMDD. Finally the section 3 closes with a discussion about all the research results of this chapter.

3.3.1 Time dependent mineralization kinetics

The modified mineralization kinetics is introduced by changing the mineralization velocity with which a bone packet increases its mineral content. In the healthy case, i.e. the non-disturbed case, the mineralization velocity does not explicitly depend on time. It is given by the derivation of the mineralization law $c = m(a)$ which relates the mineral content c to the age a of a bone packet [14]. The mineralization law is strictly monotonous and can therefore be inverted returning the age $a = m^{-1}(c)$ of a bone packet. The mineralization velocity is then defined as $v(c) = \frac{dc}{da}$. The effect of this velocity on the

[1] system of glands which regulates functions like e.g. growth and development by the use of hormones

BMDD can be imagined as a shift of each bar in the BMDD histogram to higher calcium values and it shows for young bone packets a faster and for older bone packets a slower shift.

Bone diseases can lead to a undermineralized and overmineralized bone (see section 2.2.2). To model such diseases the mineralization kinetics has to be modified. The simplest way to do this is to multiply the mineralization velocity $v(c)$ with a new factor $g \neq 1$. $g < 1$ corresponds to a reduced mineralization compared to the healthy case, $g > 1$ to an increased mineralization.

Bone diseases do not fully develop instantly. There rather has to be a smooth transition between the healthy and diseased state. To describe this transition an exponential growth function is chosen which is given by

$$h(t) = \begin{cases} 1, & t \leq 0 \\ g + (1-g)e^{-t/t_{ch}}, & t > 0 \end{cases} \tag{3.13}$$

It is assumed that the change in the mineralization kinetics occurs at $t = 0$, therefore $h(t = 0) = 1$. In the limit $t \to \infty$, $h(t)$ tends to g. The time constant t_{ch} indicates how fast the change should occur in the bone. The new mineralization velocity w now explicitly depends on time, but also on the time of formation of the new bone packet, t_a. In the extended model it is described as

$$w(c, t, t_a) = h(t)\frac{d}{dt}m(t - t_a). \tag{3.14}$$

The term $t - t_a$ as argument of the mineralization law m corresponds to the age of the bone packet. It is convenient to define $m(t - t_a) = 0$ for $t - t_a < 0$. Integration of the mineralization velocity yields the new mineralization law, $M(t, t_a)$, which describes how the mineral content increases with time t in a bone packet formed at time t_a,

$$M(t, t_a) = \int_{t_a}^{t} h(t') \cdot \frac{d}{dt'}m(t' - t_a)dt'. \tag{3.15}$$

Partial integration of this expression gives the alternative result,

$$M(t, t_a) = h(t)m(t - t_a) + \frac{1-g}{t_{ch}} \int_{t_a}^{t} e^{-t'/t_{ch}} m(t' - t_a)dt'. \tag{3.16}$$

Figure 3.4 demonstrates the consequence of this modification on the mineralization law for the case $g > 1$ for three different bone packets, one formed at $t = 0$, when the mineralization kinetics changes, one before and one after this time point. A new feature

is that the mineralization laws of different bone packets can intersect, see Figure 3.4 left. Consequently, there is no one-to-one correspondence anymore between the age of the bone packet and its mineral content. A bone packet that was formed long before the change in mineralization, almost accomplished the incorporation of mineral, and therefore hardly feels the change. On the contrary, a bone packet formed after the change in mineralization, profits from the increase in the mineralization velocity and attains higher values of the mineral content compared to older bone packets. When plotted against the time of formation, t_a, the function is not monotonous anymore, demonstrating again that at the same time t the same value of the mineral content, c, can be obtained for bone packets with different formation times, t_a, Figure 3.4 right.

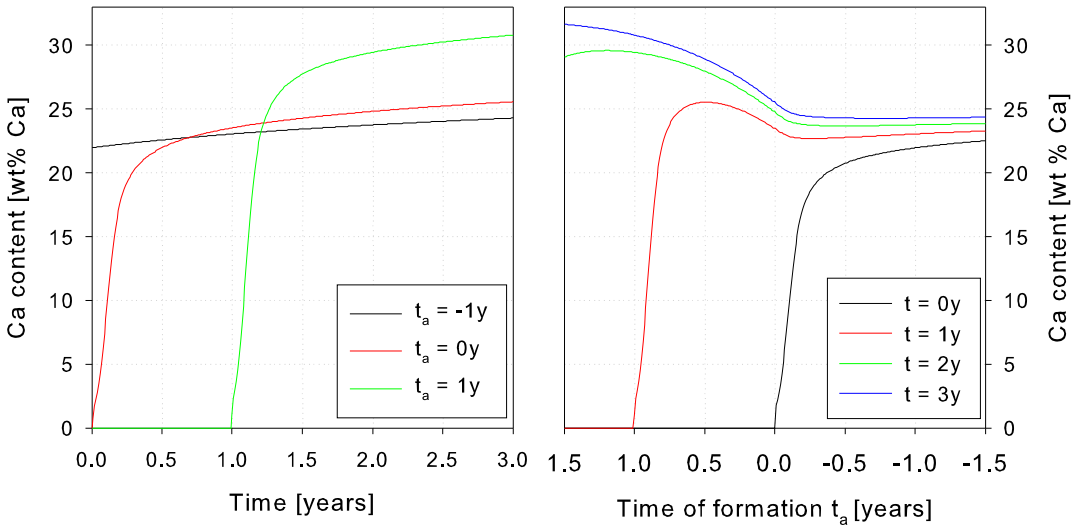

Figure 3.4: Consequence of a disturbed (here increased) mineralization kinetics on bone packets. Left: Mineralization laws showing the increase in mineral content as a function of time for the case that the mineralization kinetics is changed at time $t = 0y$ (see equation (3.15)). The chosen $g = 1.5$ corresponds to an overmineralization. The mineralization laws for three different bone packets are shown: one formed at $t_a = 0$ (red), one before the change in mineralization (black) and one after (green). The change of the mineralization kinetics results in an intersection of the mineralization laws, i.e. bone packets can exist, which have the same mineral content but differ in time of formation, t_a. Right: Mineral content of bone packets plotted as a function of the time of formation, t_a. The change of mineralization with increasing time t is reflected by a non-monotonous dependence on t_a. Note that t_a increases from right to left to improve readability of the plot.

3.3.2 Disturbed mineralization kinetics in the BMDD model

The above introduced mineralization kinetics from (3.14) is inserted in the BMDD model presented in section 2.3.3. In the original model the BMDD is described as a function $\rho(c,t)$ depending only on the calcium content c and the time t [139]. Now a function $f(c,t,t_a)$ is introduced depending also on the time the bone packet was formed t_a and which describes how likely it is to find bone at time t in a sample with calcium content $[c, c+dc]$ and formed at date $[t_a, t_a+dt_a]$. The BMDD is regained by integration over t_a:

$$\rho(c,t) = \int_{-\infty}^{t} f(c,t,t_a)dt_a. \tag{3.17}$$

With the age dependence of the bone packets the dimension of the function $f(c,t,t_a)$ is,

$$[f(c,t,t_a)] = \frac{\mu m^3}{day \cdot wt\%Ca}. \tag{3.18}$$

In the BMDD (2.2) the function $\rho(c,t)$ is replaced by $f(c,t,t_a)$ for a bone packet together with the corresponding velocity (3.14). The new equation yields

$$\frac{\partial f(c,t,t_a)}{\partial t} = \underbrace{-\frac{\partial}{\partial c}[f(c,t,t_a)w(c,t,t_a)]}_{mineralization} - \underbrace{j_{Rs}(t)\frac{f(c,t,t_a)}{BV(t)}}_{remodeling}. \tag{3.19}$$

Bone remodeling is described on the one hand as a sink of bone volume, $j_{Rs}(t)$, corresponding to resorption which is assumed to be independent of the calcium content c. Therefore $j_{Rs}(t)$ is normalized by $\frac{f(c,t,t_a)}{BV(t)}$. On the other hand bone formation is described as a source, $j_F(t)$, so that the change in bone volume BV yields

$$\frac{d}{dt}BV(t) = j_F(t) - j_{Rs}(t) = \frac{d}{dt}\int_0^{c_{max}}\int_{-\infty}^{t} f(c,t,t_a)dcdt_a. \tag{3.20}$$

A newly deposited bone packet is always non-mineralized. Therefore bone deposition defines the boundary condition at $c=0$ and $a=0$, thus

$$j_F = f(t=t_a, c=0, t_a)w(c=0, t=t_a, t_a) \tag{3.21}$$

The boundary condition at c_{max} is absorbing due to $w(c_{max})=0$. $t_{a_{max}}$ is chosen to be larger than the time period monitored in the simulation.
The time evolution equation (3.19) of a bone packet and the subsequent summing of all bone packets by (3.17) is used to investigate disturbed mineralization kinetics on the BMDD.

The time evolution equation of the BMDD (3.19) with the included modification in the mineralization kinetics is solved by inserting the modifications in an existing computer program [139] written in Matlab [140]. How the program is adapted to the introduced changes in the mineralization kinetics is demonstrated schematically in Figure 3.5 right. The old program (Figure 3.5 left) solves the continuity equation presented in section 2.3.3 including the remodeling process and the healthy mineralization kinetics. The new mineralization kinetics is inserted in the program, such that the numerical implementa-

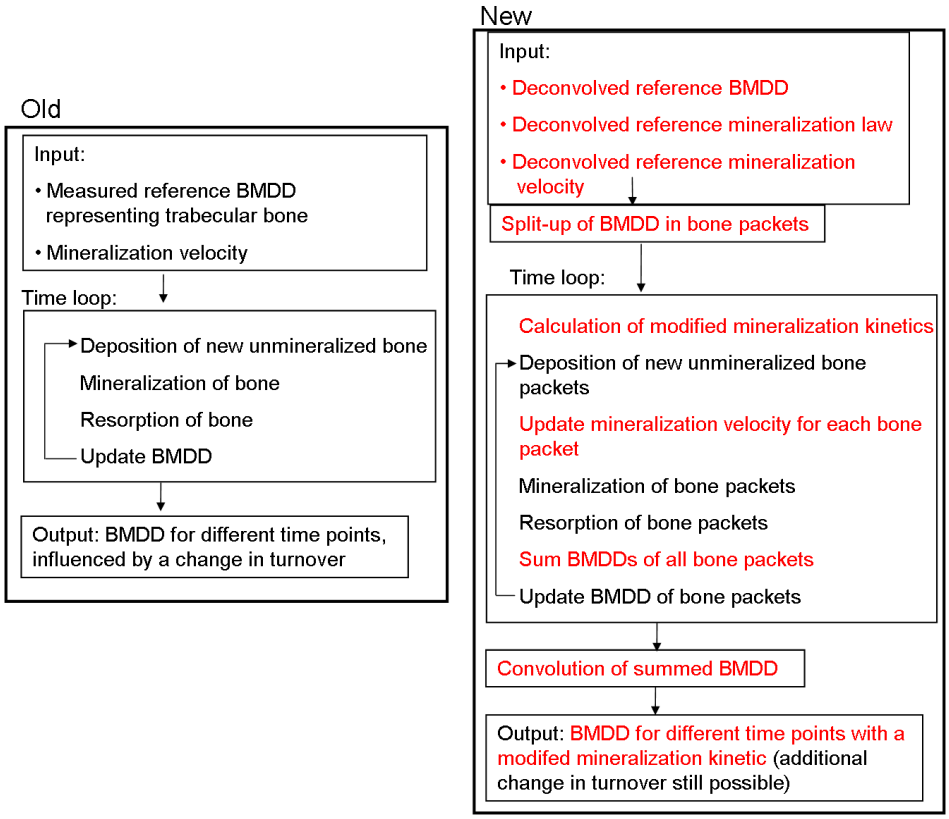

Figure 3.5: Left: Structure of BMDD model introduced in [139]. Right: The modified mineralization kinetics are introduced in the existing computer program. Changes are marked in red.

tion of deposition, mineralization and resorption of the old program does not have to be changed but can be used.

In the new program the deconvolved reference BMDD (see Figure 3.1) serves as new input together with the corresponding mineralization law and velocity. The BMDD is split in bone packets. In the time loop the new mineralization kinetics is calculated and with every new time step a bone packet is newly formed. For each bone packet (includ-

ing the new packets and the already existing ones) the modified mineralization kinetics is calculated which is needed for the mineralization in the next step. Subsequently the bone resorption occurs. Then the bone packets are summed to return the BMDD for a given time point. As a last step in the time loop all functions of bone packets are updated to give the input for the next iteration. After the simulation the BMDDs are convolved by using eq. (3.3) and (3.8). Finally as output the BMDDs are returned, which are affected by disturbed mineralization kinetics.

3.3.3 The effect of medication against osteoporosis

As mentioned earlier in section 2.2.2 the disease osteoporosis can be treated with a drug called strontium ranelate. This treatment causes the BMDD to shift to higher values. The drug probably slows down the remodeling process. However it is unclear how much of the shift results simply from the incorporation of strontium and how much is due to a reduced remodeling. Depending on the time of treatment with this drug a fraction of up to 5% of the calcium atoms in the mineral crystals is replaced by strontium atoms in the newly formed bone [87, 86]. The mineralization kinetics remains unchanged. To simulate the time evolution after strontium ranelate administration the effect of the Sr uptake is estimated.
The influence of the Sr uptake on the qBEI measurement can be estimated by calculating the mean value of the atomic number in bone, including 5% Strontium. The weighted averaged atomic number Z_{mean} of a sample in the qBEI experiment (see section 2.3.1) is calculated as

$$Z_{mean} = \frac{\sum \mathrm{N}_i \mathrm{A}_i \mathrm{Z}_i}{\sum \mathrm{N}_i \mathrm{A}_i}, \tag{3.22}$$

where N_i denotes the number of the i-th atom with atomic number Z_i and atomic mass A_i [141]. The composition of the synthetic apatite with the ratio $x = \frac{Sr}{Sr+Ca}$ of substituted Ca atoms is $(Sr_xCa_{1-x})_{10}(PO_4)_6(OH)_2$ [87].
The numerical value of g is estimated as the ratio of Z_{mean} of the 'Strontium apatite' $SrA = Sr_{10}(PO_4)_6(OH)_2$ and the normal hydroxyapatite $HA = Ca_{10}(PO_4)_6(OH)_2$. Insertion of the values for Z_i and A_i (taken from [142]) and application of (3.22) to HA and SrA yields for a 5% concentration of Sr atoms,

$$g = \frac{Z_{mean}((1-x)HA + xSrA)}{Z_{mean}(HA)} \overset{x=0.05}{=} 1.06. \tag{3.23}$$

The uptake of 5% Sr atoms in the bone can be simulated with a 6% increase in the mineralization kinetics. The dependence of g on the concentration x is shown in Figure

3.6. Note that a conversion from gray level into calcium content is not reasonable for a mineral phase which includes also strontium. For this reason the resulting BMDD (e.g.

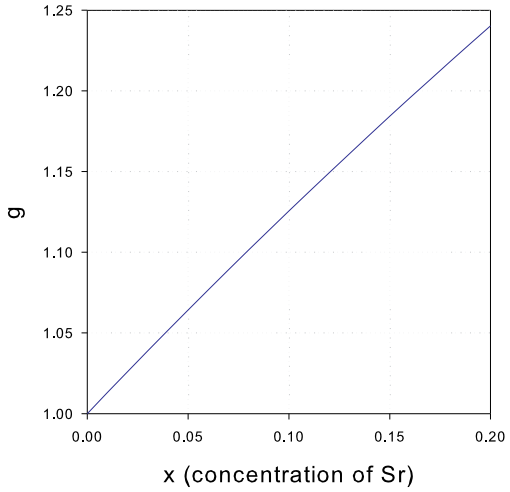

Figure 3.6: Estimation of g for changing concentration of Sr.

Figure 3.11) is plotted as a function of the Backscattered Electron Gray Level (BE-GL) or the 'apparent Ca content'.

3.4 Disturbed mineralization kinetics compared to turnover changes

Observed deviations from the healthy reference BMDDs are BMDDs that can be shifted to low and to high calcium contents. This shift however can have two different origins: a left shift of the BMDD is obtained by either reducing the mineralization kinetics or by increasing the turnover. A shift to a high calcium content is caused by an opposite scenario, namely an increase in mineralization kinetics or a decrease in turnover. Two parameters are changed to simulate the time evolution of the BMDD. For the mineralization kinetics this is the parameter g and in case of a turnover change we modify the turnover time t_{TO} (see section 2.3.3).
In the following, the differences between the effects on the BMDD obtained by a disturbed mineralization kinetics and a turnover change are presented in two ways. First BMDDs which approached the steady state for different g and for different turnover times t_{TO} are compared regarding the parameters Ca_{Mean}, Ca_{Peak} and Ca_{Width} (see section

2.3.2 for their definition). Additionally, two steady state BMDDs are shown for 6% increased and a 6% decreased mineralization kinetic together with steady state BMDDs having the same peak position but are obtained by a turnover change. The 6% increase is motivated by the treatment of osteoporosis with Sr ranelate (see section 3.3.3). For "reasons of symmetry" the decrease in mineralization kinetic is also 6%. In the second part, the transient phases of the BMDDs are investigated which result in the long run in the before described steady states. For the transient states, the time evolution $\mathrm{Ca}_{\mathrm{Width}}$ is presented. In the case of BMDDs with double peaks, the standard deviation $\mathrm{Ca}_{\mathrm{Std}}$ is calculated instead. The time constant with which the changes in the mineralization kinetic and in turnover occur, are the same and chosen as $t_{ch} = t_{EFF} = 1y$.

3.4.1 Steady state BMDDs

BMDD parameters of the steady state BMDDs

In steady state, all bone packets mineralize according to the same new mineralization law, i.e. $lim_{t->\infty} h(t) = g$ and (3.14) is $M(a) = g \cdot m(a)$. The obtained steady state distributions and the corresponding BMDD parameter are presented in the left column of Figure 3.7. All BMDD parameter linearly correlated to g and can be estimated as

$$\begin{aligned} Ca_{Mean} &\approx g \cdot 22.20 wt\% Ca \\ Ca_{Peak} &\approx g \cdot 22.94 wt\% Ca \\ Ca_{Width} &\approx g \cdot 3.30 wt\% Ca. \end{aligned} \tag{3.24}$$

This linear relationships are not found for BMDD parameters when the turnover is changed, see Figure 3.7 right. The corresponding parameters of the steady state BMDDs are adapted from [14]. An increase in turnover rate leads to a non-linear decrease in Ca_{Mean} and Ca_{Peak}. For a four times increased turnover time the corresponding Ca_{Width} reaches the smallest value.

Figure 3.7 returns a map which can be used to find out how g or t_{TO} must be changed to obtain an equal value for a BMDD parameter (gray dotted line in the Figure). For instance the same value for a 6% lowered Ca_{Peak} is obtained by either choosing a 6% reduced g or a four times increased turnover rate.

Similar BMDDs are obtained when either the mineralization kinetics is reduced or the turnover is increased. The corresponding BMDD parameters show a similar behavior in Ca_{Width} and Ca_{Peak}. This is not the case when comparing the parameters for an increased g and a reduced t_{TO}. For example, assuming a 6% increased Ca_{Peak} then the shift of the BMDD is obtained by increasing g by 6%. The turnover however has

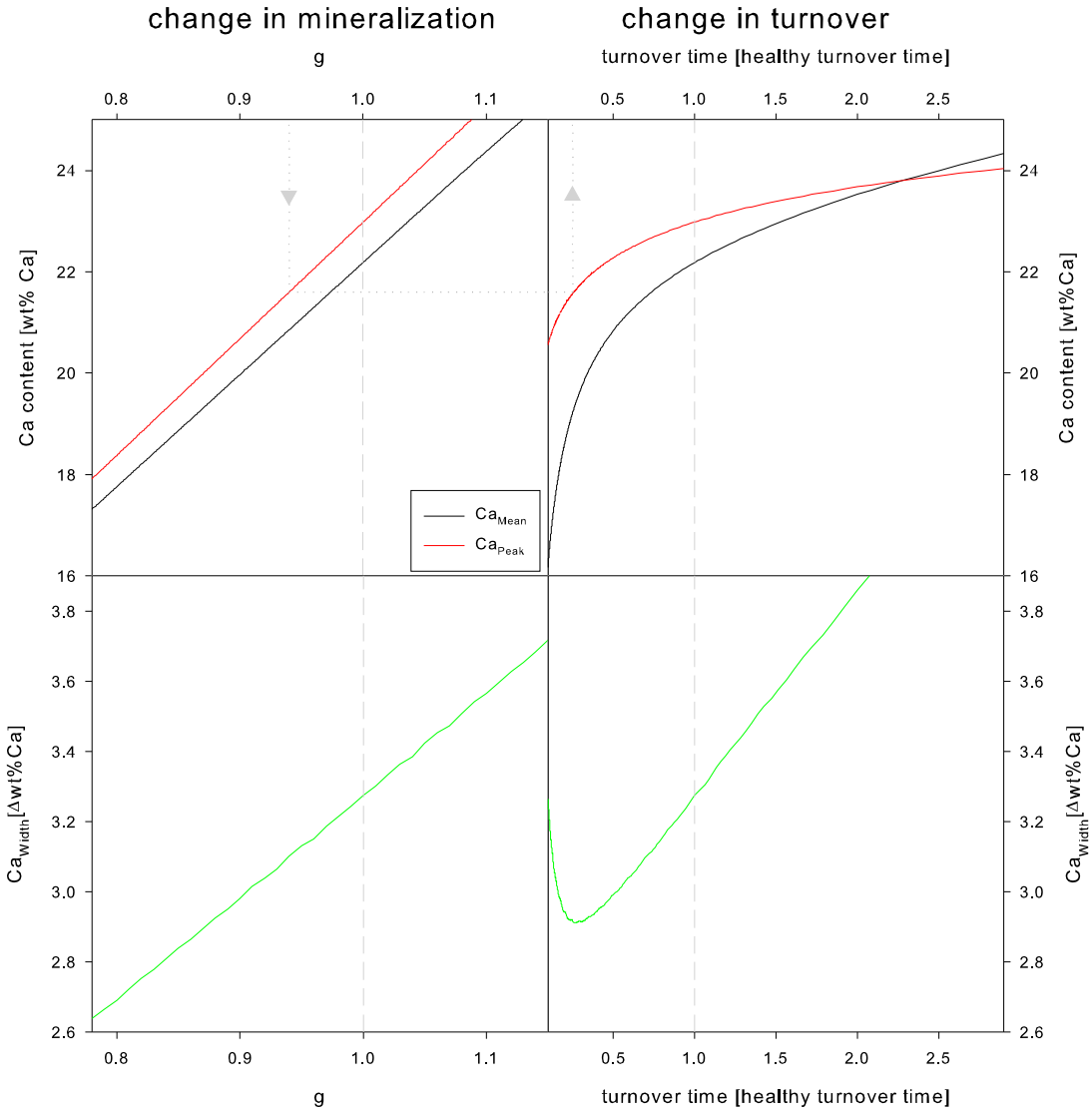

Figure 3.7: Analytically derived steady state parameter Ca_{Mean}, Ca_{Peak} and Ca_{Width} for different g (left) and different turnover times t_{TO} (right). Intersecting points of dashed lines for $g = t_{TO} = 1$ with parameters correspond to healthy reference values. Dotted line indicates which g should be chosen to obtained, e.g. for the same peak, with a changed t_{TO}. Note that $t_{TO} < 1$ corresponds to increased turnover, see section computermodels.

	Ca_{Peak}	Dev. Ref	Ca_{Mean}	Dev. Ref	Ca_{Width}	Dev. Ref
Healthy	22.98 wt%		22.20 wt%		3.26 wt%	
ML (-6%)	21.60 wt%	-6%	20.85 wt%	-6%	3.11 wt%	-5%
TO (4x)	21.60 wt%	-6%	19.20 wt%	-13%	2.92 wt%	-10%
ML (+6%)	24.35 wt%	+6%	23.50 wt%	+6%	3.45 wt%	+6%
TO (0.25x)	24.35 wt%	+6%	25.10 wt%	+13%	7.42 wt%	+128%

Table 3.1: BMDD parameter of the steady state shown in Figure 3.8 when either the mineralization is reduced or increased by 6% or when the turnover is 4 times increased or decreased. The deviation from the healthy values is given in the Dev. Ref. columns.

to be reduced by 75% to reach the same peak position. Also Ca_{Width} becomes much broader than for a change in the mineralization kinetics, see Table 3.1. In summary, by changing either the mineralization kinetics or the turnover similar BMDDs are only obtained when shifting them to lower calcium contents.

The BMDDs obtained for an either 6% increased or decreased g are shown in Figure 3.8 together with the BMDDs having the same peak position but which are obtained by a turnover change. The similar shape in case of a left shift of the BMDDs differs slightly in the higher amount of lowly mineralized bone when the turnover is increased. When

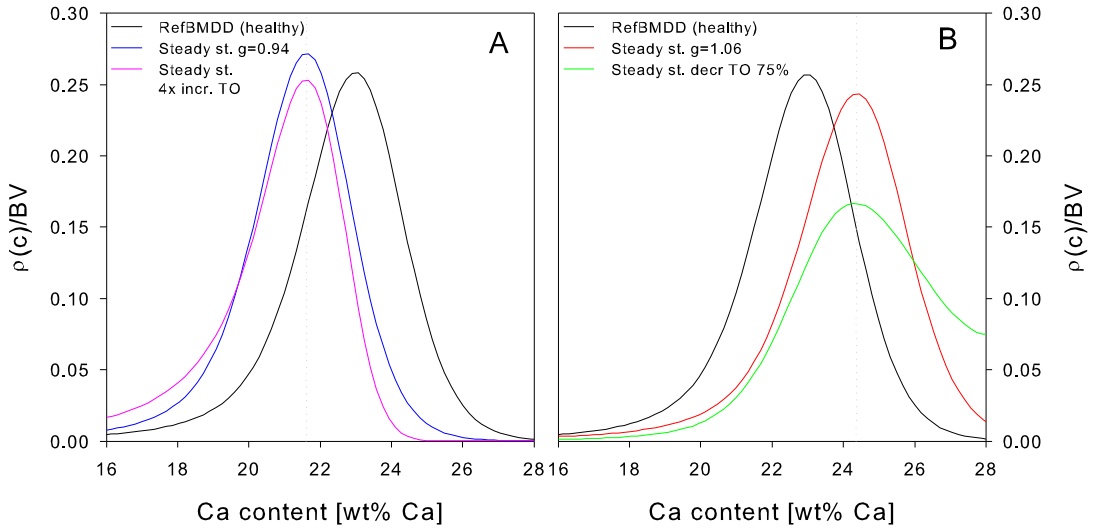

Figure 3.8: Steady state BMDDs reached for (A) mineralization reduced by 6% and turnover 4-fold increased and (B) mineralization increased by 6% and turnover 4 times reduced.

the BMDDs are shifted to higher calcium contents the amount of high mineralized bone is larger in the BMDD obtained by reduced turnover than increasing the mineralization kinetics. The corresponding BMDD parameters for the two scenarios are summarized in Table 3.1. The largest change in shape of the distribution is reflected by the large increase in width when the turnover is reduced. The 6% in the peak shift leads to 13% change in the mean value when the turnover is changed while this change is smaller (6%) when the mineralization kinetics is modified.

3.4.2 Transient states of the BMDD

Decreased mineralization kinetics compared to an increase in turnover

The reduction in the mineralization kinetics leads to a similar steady state when the turnover is increased. The transient states of these scenarios however, reveal a different behavior, see Figure 3.9. When the mineralization kinetics is reduced, the initial peak is slowly removed and gets narrower, Figure 3.9 A. The newly formed bone creates temporarily a new peak which enters at the left and slowly grows in time. The new peak

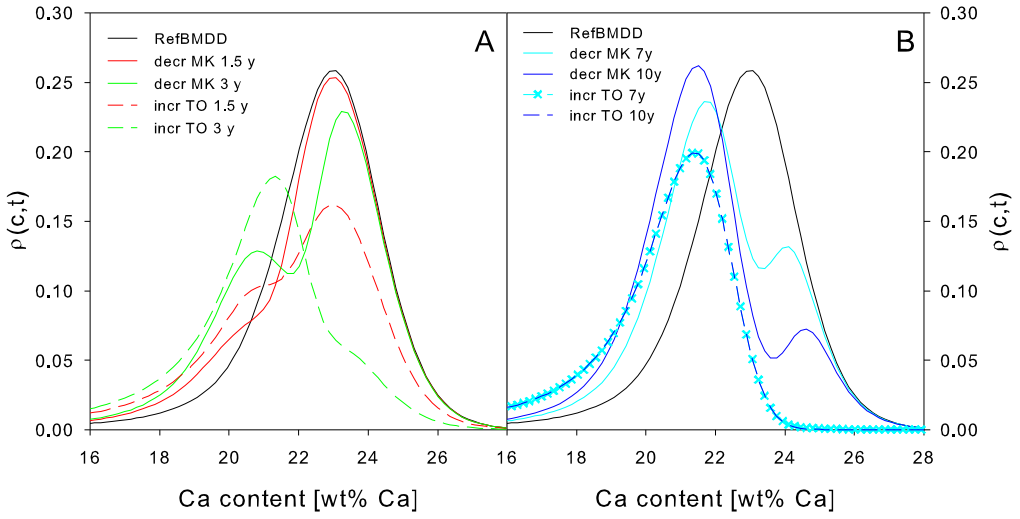

Figure 3.9: Shift of the BMDD to lower calcium contents with transient states. Decrease of mineralization kinetics by 6% (continuous lines) compared to 4 times increased turnover (dashed) scenario for early (A) and late (B) stages. The reduction of the mineralization kinetics leads to a slow lowering of the initial peak which is still present after ten years. The new equilbrium is reached faster with a turnover increase than with a reduction in mineralization kinetics.

becomes broader and slowly moves to its final position which is reached after roughly ten years. Old mineralized bone still present after ten years, is continuously removed, Figure 3.9 B.

In comparison with the time development of the BMDD obtained by an increased turnover, the initial reference peak is lowered faster and disappears virtually after three years. Also in this case new peak appears which grow fast, but the time during which the two peaks co-exist is shorter than in the first scenario. After about seven years the steady state is reached.

Due to the appearance of double peaks the corresponding standard deviations of the transient BMDDs are calculated (and not the width) and shown in Figure 3.10. A change in mineralization induces a small increase of the standard deviation in the first three years which continuously reduces with time. Increasing the time constant, which describes how fast the change in mineralization occurs, slows down this behavior and also reduces the standard deviation. The increase in turnover leads to a large increase of the standard deviation within three years. The steady state is reached very fast and Ca_{Std} remains high.

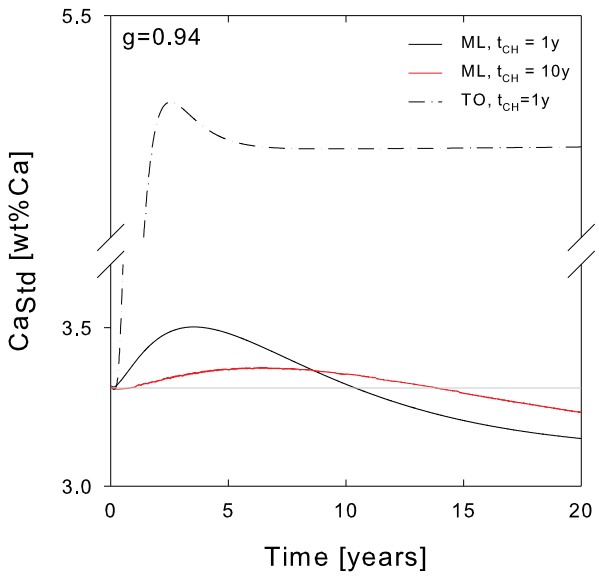

Figure 3.10: Time evolution of Ca_{Std} for BMDDs in Figure 3.9. Gray straight line shows the reference value. Continuous lines show Ca_{Std} for a decrease in mineralization kinetics for a time constant $t_{ch} = 1y$ and $10y$. The higher time constant shows a more homogeneous behavior as indicated by the slower increase in Ca_{Std}.

Increase in mineralization kinetics compared to a decrease in turnover

The increase in mineralization kinetics leads to a shift of the BMDD to high calcium contents. The shape of the BMDD differs from the distribution obtained by a reduced turnover as previously described. Their transient states however, are quite similar for a time period of approximately ten years, see Figure 3.11. In both cases the curves get narrower for longer time and shift to higher gray levels. During increased mineralization the BMDD is initially broader within the first year, becomes more homogeneous in the following and also moves a bit faster to higher values compared to the turnover changed BMDD.

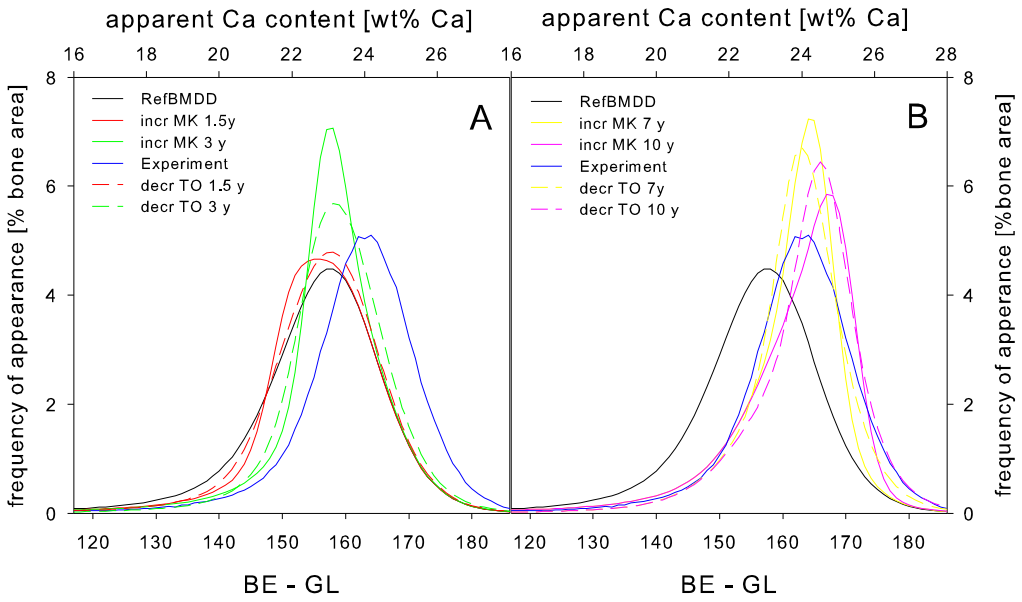

Figure 3.11: Shift of BMDDs to higher gray levels with transient states for early (A) and late (B) stages. In this scenario the shift of the BMDD is a bit faster when the mineralization kinetics (continuous lines) is 6% increased compared to a 4 times decreased turnover (dashed lines). The blue curve represents the BMDD after three years treatment with Sr ranelate (courtesy of P. Roschger).

Since the value of $g = 1.06$ is obtained by considering the incorporation of strontium in the bone the resulting BMDDs can be compared to experimental data. The experimental data in Figure 3.11 (blue curve) represents a BMDD after three years of treatment (courtesy of P. Roschger). Neither the increase in mineralization kinetics (continuous lines) nor a decrease in turnover (dashed lines) reaches the experimental BMDD after three years but only after seven years.

The time development of the corresponding width of the transient BMDDs is plotted in Figure 3.12. The most homogeneous configuration of the BMDD is obtained after 4.6 years where the width has the smallest value. The largest width is found for very late times. A ten times larger time constant leads to more homogeneous development of the BMDD. The initial broadening is less expressed and within 20 years this remains the largest width.

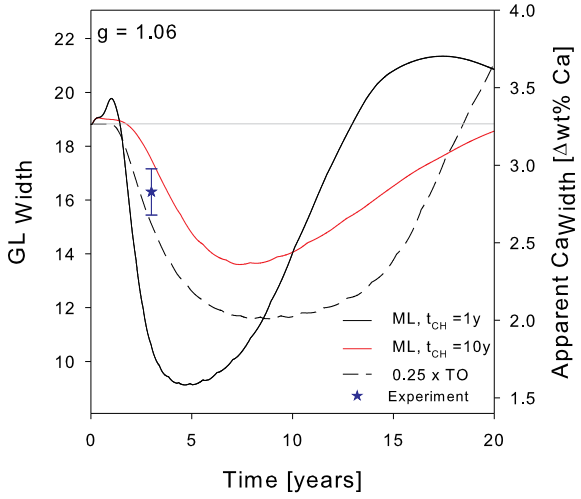

Figure 3.12: Width of the BMDDs for increased mineralization kinetics (continuous lines) for different time constants t_{CH} compared to width of BMDDs obtained by a decrease in turnover (dashed). Gray lines mark the width of the reference BMDD and the steady state BMDD simulated with increased mineralization kinetics (dotted). The width of the BMDD after treatment with Strontium ranelate is shown by the star.

3.5 Discussion

For a fruitful interplay between experiment and simulation, considerable effort has to be spent to make the outcome of both comparable. In particular, simulations always have to take into consideration the limitations of the experiment. Two corrections typically have to be made. First, whenever data from an experiment is used as model input, it has to be corrected for unwanted influences of the measurement process. Second, before the direct comparison between experimental and simulational results occurs, the theoretical results should be subjected to the same limitations as occurring in the experiment.
This approach is applied to measurements of the mineral heterogeneity of bone us-

ing quantitative backscattered electron imaging (qBEI). The experimental result is a probability distribution of the differences in the mineral content in bone (BMDD). The experiments are complemented by mathematical modeling. The model considers both the processes of remodeling and mineralization and allows predicting the time evolution of the BMDD.

Based on qBEI measurements of homogeneous materials (carbon and aluminum), the compromising influence of the measurement could be quantified in form of a matrix which connects the "true" and measured distributions. The small determinant and resulting poor invertability of the matrix makes the use of regularization for the (approximated) inversion indispensable. Using the Tikhonov regularization method, it is tested that the main parameters, Ca_{Width} and Ca_{Peak}, of the deconvolved distribution are robust to the choice of the regularization parameter λ, when λ stays within a range of +/- 50%.

Applying the deconvolution method to the reference BMDD is particularly important. Deviations from this reference BMDD are used for diagnostic purposes. Therefore an accurate definition of the healthy reference is needed. The present work demonstrates that the width of the reference BMDD is slightly overestimated due to two separate effects. The measurement by counting backscattered electrons causes a broadening, which can be estimated by deconvolving the distribution. The interindividual variability of healthy individuals makes it necessary to take the average over 52 BMDDs in defining the reference BMDD. This averaging also increases the width of the distribution. Both contributions have the effect that the corrected Ca_{Width} of the reference BMDD is about 8% smaller than the previously reported value [108]. We want to emphasize that this correction is nevertheless clearly within the 95% confidence interval of the reference BMDD, outside which bone diseases are diagnosed. In addition, an accurate definition of the reference BMDD is important since conclusions from it can be drawn about the mineralization kinetics. The mineralization law calculated from the deconvolved BMDD shows that the incorporation of mineral occurs faster during the first six months after bone formation. The deconvolved reference BMDD and the corrected mineralization law serves as input for the simulation of the disturbed mineralization kinetics.

In this second part, the aim is to quantify and distinguish the influence on the BMDD resulting from: a) a change in the mineralization kinetics and b) a change in the remodeling process. In the case a) of the simulation the remodeling process (i.e. the remodeling rate) remains unchanged, while in case b) the mineralization is kept normal.

Within a given range the same peak position of the BMDD can be reached by changing either the mineralization kinetics or the turnover. The left shift of the BMDD achieved through reduced mineralization or increased turnover leads in both cases to an increased

heterogeneity in the transition phase. The main difference between the two scenarios is that with a reduced mineralization velocity the steady state is reached slower than during an increased turnover scenario.
The shift of the BMDD to a higher calcium content, caused by increased mineralization kinetics or a reduced turnover, does not reveal large differences in the transition phase. Both processes lead transiently to a more homogeneous, i.e. narrower distribution. In this scenario the increased mineralization kinetics lead faster to the steady state than a reduction in turnover.
A right shift of the BMDD can be caused by the drug strontium ranelate which was given in a clinical study to a patient for three years. It probably reduces the turnover and is incorporated into the bone matrix in addition to calcium. This leads to an apparently increased mineral content in the BMDD even though there is no disturbed mineralization [116, 87]. This apparent increase was simulated by a 6% increased mineralization kinetics. After three years, the experimental curve is not reached, only after seven years there is an overlap with the measured BMDD. An additional reduction in turnover in the model does not lead to a further shift but a narrowing of the BMDD (data not shown). The mismatch between experiment and simulation may be due to an underestimation of the time dependent factor $h(t)$ which is assumed as exponential function with a time constant $t_{ch} = 1y$. However, a value of $t_{ch} = 0y$ corresponding to an immediate switch from normal to final (disturbed) mineralization kinetics also does not lead to a much faster shift of the BMDD to higher values. Therefore assuming another function $h(t)$ would not result in a faster shift of the BMDD to higher values. What actually leads to the shift of the experimental BMDD remains unclear. From this study it can be concluded that it is not only due to a substitution of calicum by strontium atoms.
The decrease in mineralization kinetics in the model can be interpreted as a lack of suitable space for the mineral to grow in the collagen matrix. The result would be a lowly mineralized bone which appears in the bone disease osteomalacia. Osteomalacia is related to a defective mineralization [82] and a degenerated collagen matrix. The matrix offers too few nucleation sites for the mineral to crystallize, thus inhibiting a further growth of the crystals which leads to a low mineralized bone. The corresponding BMDD shows a shift to low calcium contents, see Figure 2.4. The peak position is easily reached by decreasing the mineralization kinetics by 14%, however the experimental data also show a very broad distribution which is not obtained in the simulation. The transient BMDDs show a lowering and a strong broadening of the peak (not shown). Based on the simulations the measured BMDD can be interpreted as a transient state which would develop at low mineral contents when the effect of the disease continues.

4 Mineralization in trabecular bone observed *in vivo*

In this chapter a method is presented which allows evaluating the mineralization process in mice bone *in vivo* by the use of micro-CT images. The provided images are obtained from a measurement described in section 2.4.1. The aim of the image evaluation is manifold. The question is asked weather it is possible to quantify the mineralization process in newly formed and quiescent bone. Since the images monitor the time development of the same bone it can be asked if osteoclasts resorb bone with a higher/lower mineral content than average. As a lost point the influence of the mechanical stimulus on the mineralization process can be characterized.
In the first section the evaluation method is presented by showing the procedure for one mouse. Subsequently the results are presented which include the data of all mice of the experiment. The chapter is closed with a discussion about the results and the applied method.

4.1 Mineralization evaluation depending on the distance to the surface of trabecular bone

4.1.1 Data analysis - Division of trabecular bone into layers

The obtained micro-CT images allow investigating the mineralization process in the same bone of the same animal. Such a reconstructed three-dimensional image of an entire vertebral mouse bone and a lateral cut are shown in Figure 4.1. In addition regions of newly formed and resorbed bone can be identified when the images of the different time points are aligned and overlapped [13], see Figure 4.2 bottom. The overlapping of images with one week time distance allows categorizing the bone in regions of bone formation and bone resorption [13]. Bone only present in the earlier image is defined as resorbed and as formed bone in the later image. The unchanged, i.e. not remodeled bone volume is referred to as quiescent bone.
Before analyzing the images two problems have to be faced, which are first the partial

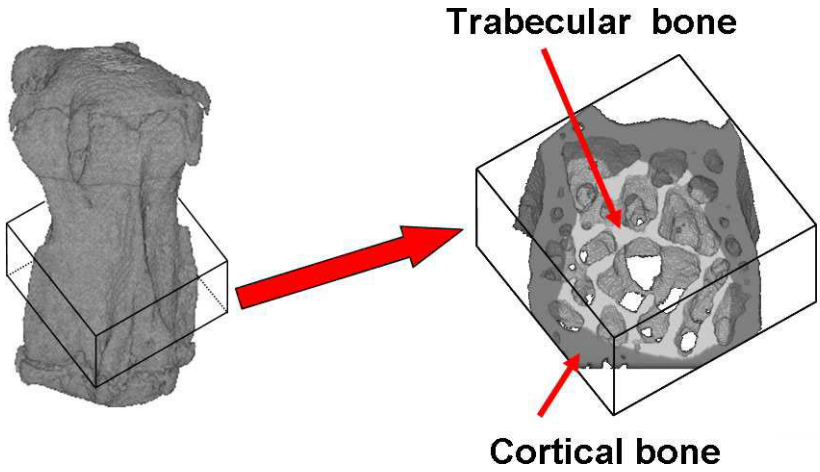

Figure 4.1: Example of the investigated vertebra in the mouse tail. Left: reconstructed scans of the vertebra in the mouse tail. Right: A cross section of the vertebra shows the cortical and the trabecular bone.

volume effect and second the beam hardening effect. The voxels of the surface of the bone are afflicted by the partial volume effect. The volume which is presented by the voxel at the surface could be partly filled with bone and partly filled with surrounding soft tissue (marrow blood etc). Therefore the voxel displays a gray level which is too low. Consequently, the surface layer is excluded in the evaluation. In the voxels beneath the surface the partial volume effect is marginal.

The second problem is the beam hardening effect (see section 2.4.1). It is known that beam hardening leads to a decrease in intensity when moving from the surface towards the center of cylindrical structures [143]. Therefore only voxels of the different bone categories are compared which have the same distance from the surface. For this purpose the whole trabecular bone is subdivided into 'layers'. Starting from the outer surface of the bone, always the outer layer is peeled off from the surface. Each layer has a thickness of one voxel. In this way the first layer (corresponding to the surface layer), second layer and so forth are defined (Figure 4.2 top middle shows this analysis up to the sixth layer). The trabecular architecture and the resolution of the μCT images implicate that the first layer consists of the largest amount of voxels (34%) compared to 28% in the second and 20% in the third layer. The evalution focuses on the second and third layer. The subdivision of the bone into layers is performed for every mouse and all the five time points.

The gray level images are evaluated in two ways. First, gray level histograms of bone formed or resorbed within one week are calculated for each mouse. The histograms are

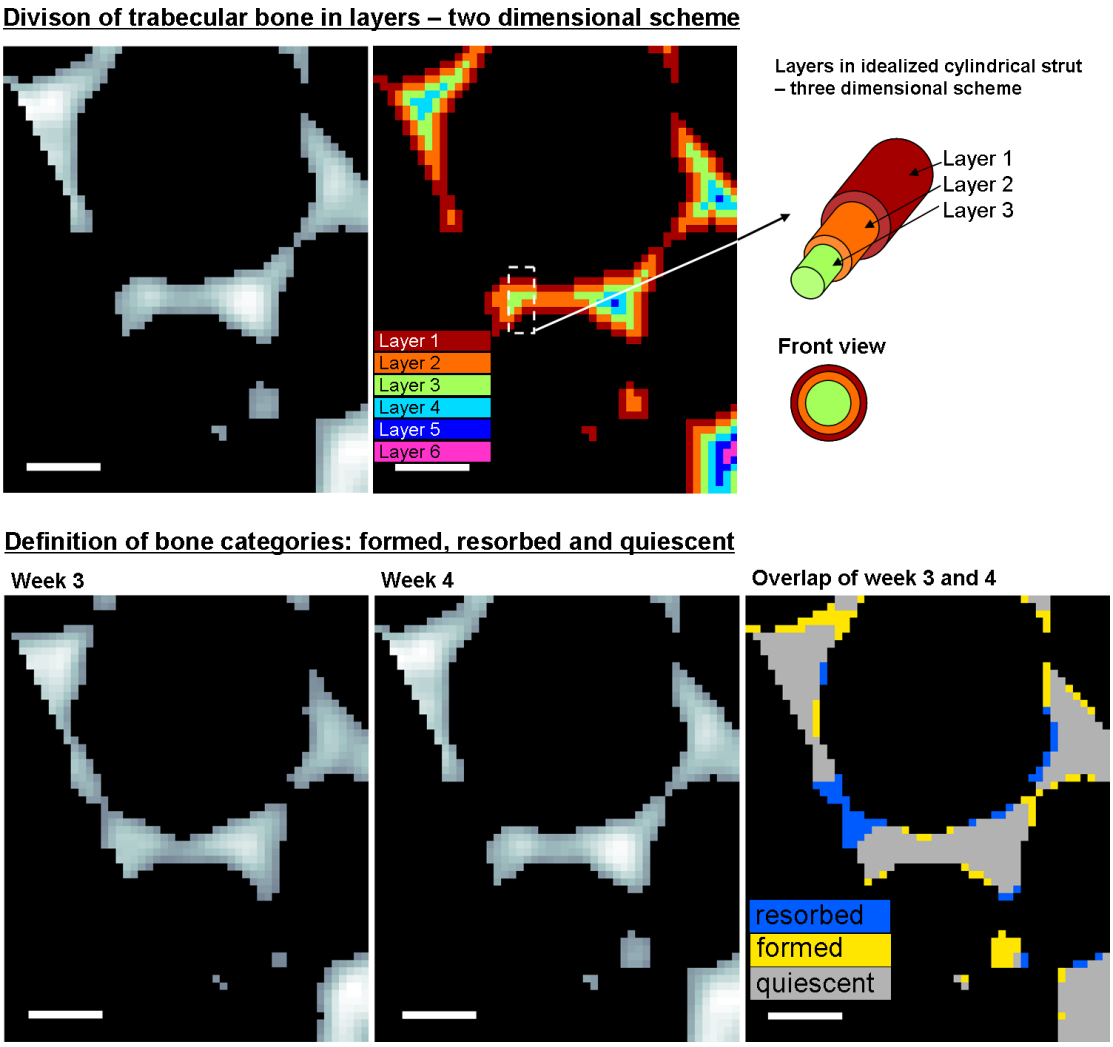

Figure 4.2: Procedure of image evaluation. Top left: Cross-sectional slice of trabecular bone. Brighter gray levels show higher, darker gray levels a lower amount of mineral in the bone. Top middle: The trabecular bone is divided into one voxel thick layers (indicated by the different colors) to confine the beam hardening effect (see text). Three dimensional scheme of the layer analysis is shown at the top right. Layer 1 comprises all voxels at the surface; layer 2 all nearest neighbor voxels of layer 1 and so on. Bottom left and middle: Two cross-sections showing the same part of the vertebra at two different time points in the living mouse. Bottom right: The comparison between the images allows the subdivision of the trabecular bone into three categories: formed (yellow), resorbed (blue) and quiescent (bright gray). The scale bars denote 105 μm.

normalized to have a total area of one. Therefore they display the probability to find resorbed (formed) bone with a given mineral content. In the same way, the distributions of quiescent bone are obtained. The probability distributions are averaged over all mice in each category (formed, resorbed or quiescent) in one group since no difference is found within one group (loaded or control). Thus one distribution for each category for one group is obtained which is compared to a reference distribution. The reference is calculated from all voxels in a given layer of the control group and contains all voxels independent of the category formed, resorbed or quiescent.
The second way to evaluate the images is to follow the mineral content of all the voxels corresponding to bone formed in the first week, over the consecutive three weeks. In the same way, all the bone resorbed in the last week is traced back in time. Due to the ongoing remodeling, a bone voxel initially in the second layer can change its layer with time. For example, the voxel can be found in the surface layer if bone above is resorbed. It can also move deeper inside if bone is deposited on top of it. Due to the beam hardening effect the beam intensity changes with the distance from the surface, i.e. from layer to layer. Therefore the most accurate way to evalute the changing mineral content with time, is to consider voxels which stay in the same layer over the entire time of observation. The same holds for the voxels, resorbed in the last week. Such evaluation allows a direct quantification of the mineralization kinetics after bone formation and the demineralization kinetics before resorption.
From the followed voxels the mineral distributions are calculated for each time point, mice and categories. A mean mineral content is calculated for each distribution returning nine values at every time point for each category. The mean values are averaged returning an averaged mineral content for each time point with a corresponding standard error.

4.1.2 Data analysis - Conversion of gray levels in mineral content

A quantification of the gray levels in terms of mineral content is possible after calibration of the images with a phantom containing different concentrations of hydroxyapatite [12]. Therefore a polynomial correction algorithm was applied before reconstruction of the images . The resulting images are also gray level images but their gray levels correspond to a defined mineral content $c(GL)$ given in mg of hydroxyapatite (HA) per cubic centimeter. The corresponding linear relation is given by

$$c(GL) = mGL + n. \tag{4.1}$$

The slope $m = 0.07\frac{\text{mg}HA}{cm^3}$ and the intercept $n = -193.41\frac{\text{mg}HA}{cm^3}$ are obtained from the algorithm and correspond to the slope and the intercept relating the mineral concentration to linear attenuation μ which equals the gray level GL. The linear relationship is shown in Figure 4.3. In the following all gray levels are converted into mineral content by using (4.1).

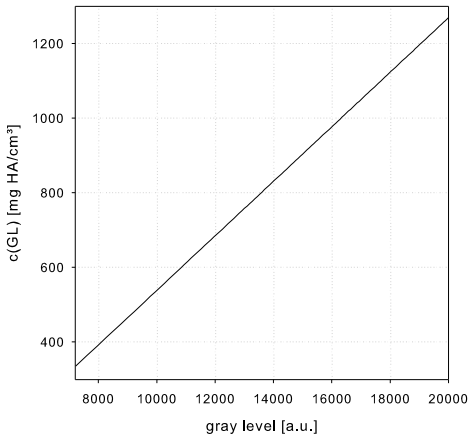

Figure 4.3: Linear relation between gray level and mineral content in units of $\frac{\text{mg}HA}{cm^3}$.

4.2 Results - Mineralization process in trabecular bone *in vivo*

The first result is shown in Figure 4.4. The left plot shows the gray level histograms as a function of the distance from the bone surface, i.e. as a function of the layer number. Only the histogram of the surface layer (first layer) is afflicted by the threshold ($\approx$320 $\text{mg}\frac{HA}{cm^3}$) since it coincides with the smallest value shown in the Figure. With increasing distance from the surface, the histogram shifts to larger values of the mineral content and becomes broader. The corresponding mean values of the mineral content (right Figure 4.4) are not different for the control group and the loaded group. The values lie within the error bars.

Next, the distributions of the mineral content are analyzed within the different categories of formed, resorbed and quiescent bone. All micro-CT images measured with one week time difference are considered, resulting in 36 data sets for the control and 36 for the loaded group. Within the one week time interval it is found that most of the bone in layer 2 and layer 3 is not remodeled (see Table 4.1). Not surprisingly, the amount of remodeled bone is even less in layer 3 compared to layer 2. In Figure 4.5, the correspond-

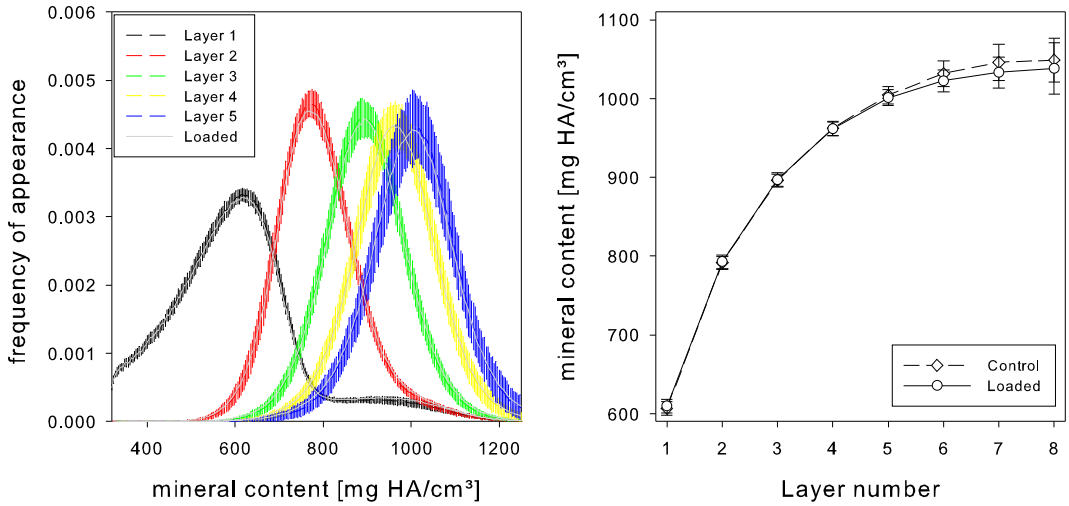

Figure 4.4: Mineral content depending on the distance from the trabecular surface. Left, mineral distributions for bone as a function of the layer number. The threshold value for the binarization of the micro-CT images corresponds to the lowest value of the x-axis in the diagram. Colored curves correspond to the control group, the gray lines to the loaded group. Error bars correspond to the standard deviation. Right, mean values of the mineral content with standard deviation as a function of the layer number.

		layer 2	layer 3
formed	control	2.93 ± 1.35%	0.27 ± 0.21%
	loaded	4.27 ± 2.36%	0.62 ± 0.82%
resorbed	control	5.21 ± 3.09%	1.74 ± 1.37%
	loaded	3.73 ± 1.82%	1.09 ± 0.74%
quiescent	control	91.86 ± 4.08%	97.99 ± 1.45%
	loaded	92.00 ± 4.00%	98.29 ± 1.48 %

Table 4.1: Amount of voxels in the different categories. The percentage of voxels in each animal group (control and loaded) and in each category (formed, resorbed and quiescent) for layer 2 and 3. Layers include voxels with the same distance from the trabecular bone surface. Reported errors correspond to standard error.

ing mineral density distributions are shown for layer 2 and 3. They are averaged within the loaded and unloaded group for newly formed and resorbed bone. For formed bone (Figure 4.5 left), the distributions are shifted to lower values of the mineral content with respect to the reference distribution. The peak position of the distribution of layer 2 is shifted by 74 mg HA/cm^3, that of layer 3 by 132 mg HA/cm^3 to lower mineral contents compared to the reference. In addition, for layer 2 the distribution is narrower than that of the reference. Also for resorption (Figure 4.5 right), the distributions are shifted to the left in comparison with the reference, but less and with less difference between the two layers: 46 mg HA/cm^3 for layer 2 and 48 mg HA/cm^3 for layer 3. Observed differences between the loaded and the control group are within the standard error. With most of the bone in layer 2 and layer 3 not being remodeled (see Table 4.1), the distribution of quiescent bone (not shown) is almost identical to the reference distribution.

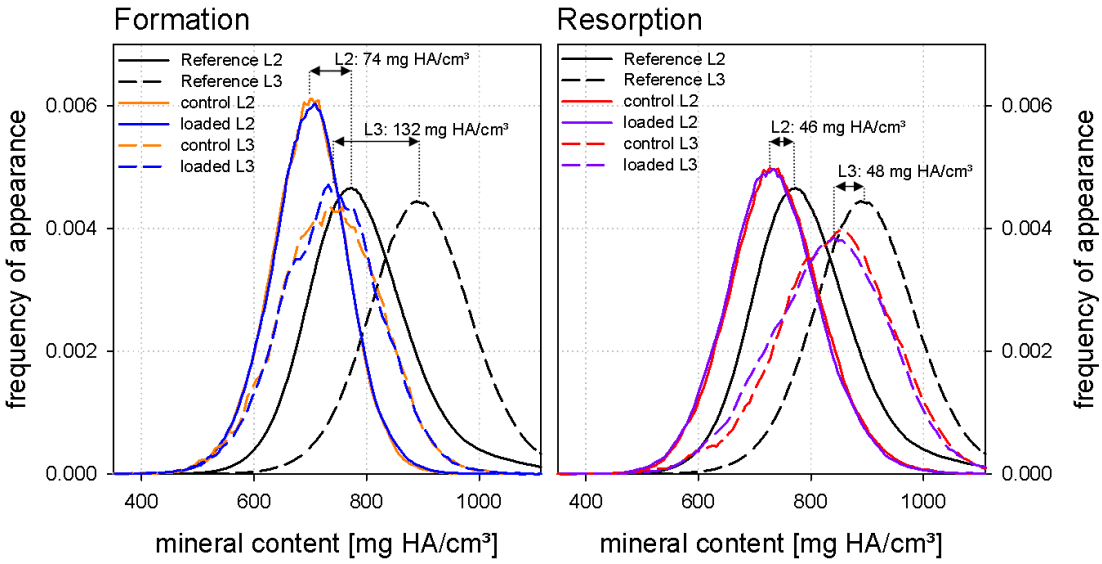

Figure 4.5: Distributions of mineral content of formed and resorbed bone compared to the reference distributions. The presented distribution are averaged from all distributions obtained for the first one-week interval and every mouse. Left: The distributions of formed bone of the control and the loaded group are both shifted in layer 2 and layer 3 to lower mineral contents compared to the corresponding references. Right: The distance between the distributions of resorbed bone and the reference show that in the second and third layer, lowly mineralized bone is resorbed. Since the distributions only show the bone that was resorbed within one week, the last step of the resorption process is seen, indicating that the bone is already demineralized. What happened before this step is demonstrated in Figure 4.6.

The time evolution of the averaged mineral content in formed, resorbed and quiescent bone is shown in Figure 4.6. In the analysis of bone in layer 2 (Figure 4.6, left) formed bone starts with the lowest value of the mineral content, reaching after three weeks 97% of the reference value. Also for quiescent bone the mean values of the mineral content increases, but the starting point is slightly above the reference value. Interestingly, considering resorbed bone, the mineral content dropped by 4% one week prior to resorption. The analysis of the third layer (Figure 4.6, right) give qualitatively similar results. A linear regression of the data demonstrates that the slopes for quiescent bone is higher for the loaded group in comparison with the control group. The difference between the slopes is roughly $5 mgHA/cm^3$ per week when considereing layer 2 and layer 3. Furthermore, comparison of the slope of quiescent and formed bone show that the mineralization kinetics is faster. Here the difference between the slopes is about $22 mgHA/cm^3$ per week.

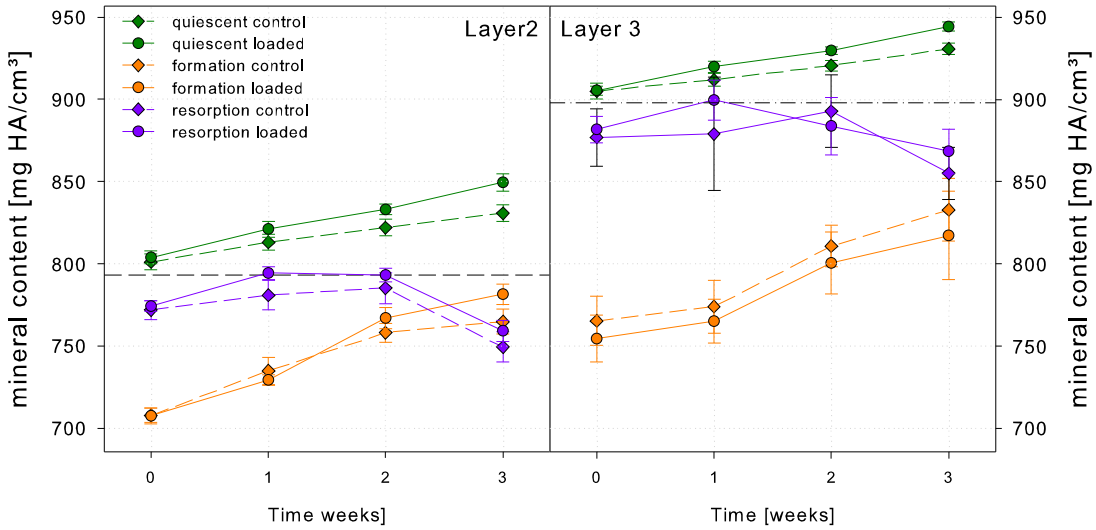

Figure 4.6: Time evolution of averaged mineral contents in layer 2 (left) and layer 3 (right). Both layers give qualitatively similar results. The increase of mineral content with time is faster in formed bone than in quiescent bone in both layers (see text). Considering resorbed bone, the mineral content dropped by 4% one week prior to resorption. A slightly larger increase in mineral content is seen in the loaded group in quiescent bone.

4.3 Discussion

In this study the structural changes of trabecular bone in a mouse vertebra as detected by in vivo micro-CT are analyzed. On the one hand, the trabecular architecture changes due to bone remodeling. This architectural change can be detected by determining differences between aligned micro-CT-images of the same vertebra at different time points. On the other hand, the material within the trabeculae changes due to mineralization. The gray levels of micro-CT images give information of local differences of the mineral content within the trabeculae. Combination of the information on both hierarchical levels allows a quantification of the mineralization kinetics after bone formation and the demineralization kinetics before bone resorption.

The evaluation of the gray levels of micro-CT-images shows that the further away the bone is from the surface the higher is its mineral content (Figure 4.4) which is in agreement with [144]. This is contrary to what is expected for a homogeneous material under effect of beam hardening [143]. The increase of the mineral content with the distance from the surface can be explained as an age effect. On average younger bone is found closer to the surface and older bone more in the middle of the trabeculae. Older bone had more time to mineralize, which explains the higher mineral content of bone in the core of the trabeculae.

The mineralization kinetics can be quantified by monitoring all the bone which is newly formed within the first week over the consecutive three weeks. In the same way the mineral content of quiescent bone and bone before resorption can be quantified. The most important findings are: (i) newly formed bone mineralizes faster than quiescent bone by almost a factor of two. This result is in agreement with the known slowing down of the mineralization process with the classification in a fast primary mineralization and a slower secondary mineralization [14]. (ii) Mechanical load increases the rate of mineral incorporation into bone. Here the increase is roughly 40%. Due to the much larger number of voxels included in the analysis, this result is highly significant for quiescent bone, but not for newly formed bone. (iii) In the week before the bone is resorbed the mineral content decreases. This is also in agreement with reports in literature. Osteoclasts first dissolve the mineral by building and acidic environment around the resorption site, before the collagen matrix is degraded [49, 51]. The presented method allows for the first time to quantify the kinetics of this demineralization. Since the surface layer is always excluded form the analysis, it has to be emphasized that really a demineralization is observed and not already bone resorption. (iv) Furthermore, the question can be addressed whether the osteoclasts have a preference to resorb bone with a particularly

high or low mineral content. A high mineral content would be expected when osteoclasts remove micro-damaged bone, which is on average older and therefore higher mineralized [145]. The contrary that osteoclasts resorb bone of low mineral content is based on the rationale that resorption initiates from the surface, where the mineral content is lower [91, 98]. The mineral distribution of the bone one week prior to resorption (Figure 4.5) seems at first sight to endorse neither of the two hypothesis: as this bone has the same mineral content distribution as the reference bone two to three weeks before resorption (Figure 4.6) the investigations give no evidence that osteoclasts prefer to resorb bone of a particularly high or low mineral content.

The limitations of the proposed method are set by the accuracy of the determination of the structural changes. As discussed in [13] in weekly measurements the resolution of 10.5 μm is sufficient to obtain volumes of formed and resorbed bone. The volumes are large enough to be detected, although an even higher resolution would be desirable. An imperfect alignment of images of the same bone taken at different time points results in a systematic error of the obtained rates of bone formation and resorption towards too large values. The good agreement with results from histomorphometry testifies about a successful alignment of the images. The current study further support that the used alignment algorithm is working and that it is possible to monitor a defined bone volume in time. Only based on a reasonable alignment of the images, the obtained mineralization kinetics of newly formed bone (Figure 4.6) can be understood.

The main problem for a quantitative interpretation of the measured gray levels in terms of local changes in the mineral content is the beam hardening effect. In the present study its effect is minimized due to the following reasons. Firstly the cortical shell results in a pre-hardening of the beam. Secondly, a correction algorithm was applied in comparison with a hydroxyapatite phantom including 200 mgHA/cm^3 [12]. Thirdly, it was shown that particular care to avoid beam hardening artifacts is necessary when bone samples of different size are analyzed [146]. In our case, the studied vertebrae are not only of similar size. The five micro-CT-images that are aligned and evaluated have virtually even the same microarchitecture. Fourthly, in the analysis only bone is included, which is positioned in the same way in the trabecular architecture. Bone is considered to stay in the same "layer" (see Figure 4.2) and therefore has a similar distance from the trabecular surface. The beam hardening can only be avoided by using monochromatic x-ray radiation as offered by a synchrotron. However, while the radiation dose, to which the animal is exposed in a series of micro-CT measurements, does not interfere strongly with bone biology [147], the same statement is doubtable when using synchrotron radiation. It has to be emphasized that the main results of the study are independent of a perfect

beam hardening correction. This is because the results are obtained by comparison between the gray level distributions of the three different categories of formed, resorbed and quiescent bone in the same layers in the loaded and control group.
The detailed analysis of structural changes due to bone remodeling and mineralization with *in vivo* micro-computed tomography will be limited to small animals like mice for the near future. With the availability of diverse disease models in these animals the presented method allows to study changes in the mineralization kinetics in bone diseases like osteomalacia or osteogenesis imperfecta. A further important application is the study of how pharmaceutical therapies interfere with bone mineralization.

5 Remodeling in cortical bone of horses

In this section a new approach to quantify the spatial arrangement of osteons in cortical horse bone is presented. The aim is to go beyond simple counting of osteons and their classification within an area of cortical bone. The idea is to link the arrangement to a possible physiological meaning in terms of nutrient supply of the osteocytes in the bone. In order to quantify the spatial arrangement a simple model is introduced which produces images that are gradually filled with osteons. The simulated images are compared to the experimental images by calculating first the autocorrelation function (ACF), which describes the probability of finding two canals separated by a given distance and second the shortest distance distribution (SDD), which describes the probability that a site within bone is located at a given distance from the nearest canal. This model was published in [148]
The discussion about all the experimental results can be found in appendix C. The comparison between the experimental and simulated results should provide insights in the 'laws' governing the remodeling process in cortical bone therefore a more physiological interpretation of the introduced model is presented in the discussion of this chapter.

5.1 Quantification of the osteonal arrangement in horse bones

5.1.1 Simulation of the ordered arrangement of osteons

Cortical bone is considered as a two-phase material in which the blood-filled canals (depicted in black) are one phase and the bone tissue (depicted in white, including lamellae, osteocyte lacunae, cement lines, etc.) as a second phase. In the computer model the hypothesis is tested whether an "effective repulsion" between canals can explain the observed order. To test this hypothesis the following rule is introduced in the model: each added osteon, represented by its canal, is encircled by a given area within which it is forbidden to place another osteon. The circular exclusion area around each canal, is described by the exclusion radius, R_{excl}. This model is usually referred to as cherry-pit model [149].
The simulation starts with an empty image with dimensions slightly larger than those of

the experimental images. This allows placing canals also at the boundary of the image. Only a region of interest identical to that of the experimental images is used for the analysis. New canals are created sequentially using an algorithm of three steps. The canals are assumed as a circle of uniform size with a defined canal radius. This radius is an averaged value obtained from the experimental images and is for the horse $R_{ca} = 28.17$ μm. In the first step of the algorithm, a potential position of a new canal is chosen randomly. In the second step, it is tested, whether the new canal would overlap with

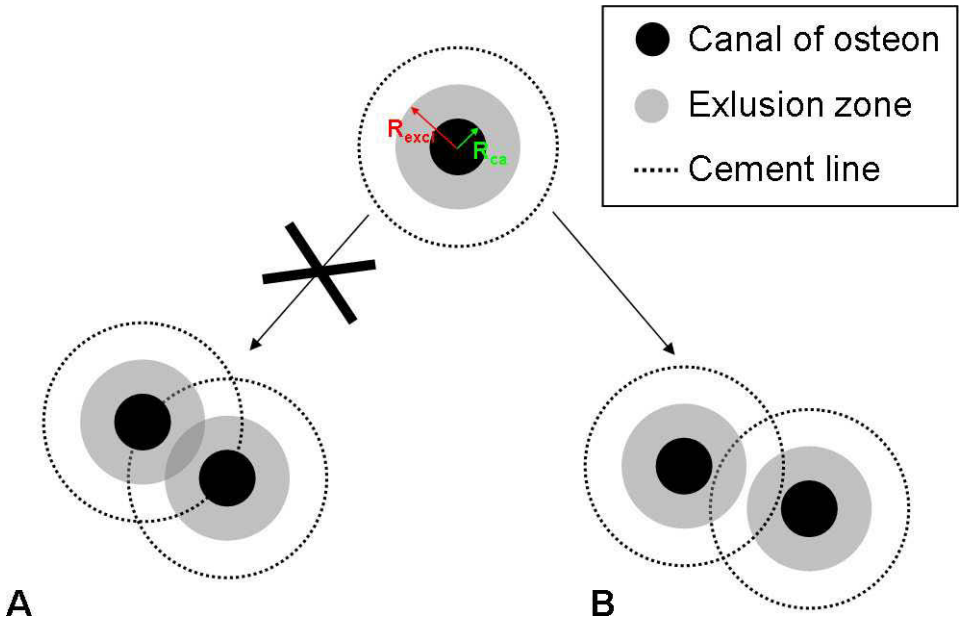

Figure 5.1: A sketch of the RSA of osteons highlighting the process of adding a new osteon In the model an osteon is characterized by the size of its canal (marked in black), R_{ca}, and by its exclusion zone (gray) given by the exclusion radius, R_{excl}. A: An unsuccessful addition occurs if the exclusion zones of two osteons overlap. B: A successful addition occurs in the simulation if there is no overlap of the exclusion zones.

another exclusion zone. In the third step, the algorithm offers two possibilities. If there is no overlap of exclusion zones of any of the existing canals (Figure 5.1, Case B), the new canal is added to the simulation image. In the case of an overlap (Case A), an alternate position for a new canal is again chosen randomly. This random sequential addition (RSA) [149] process is continued until the appropriate density of canals (determined from an average of the experimental images) is obtained. The choice of a too large exclusion radius would make it impossible to reach the designated density of osteons. The model is intended to produce an arrangement of osteons with some order, but not

to precisely mimic the remodeling process. Therefore, removal of old osteons by the formation of new ones is not included in the model. The analysis rather concentrates on the spatial organization of the canals (the structure factor) and not on the effect of the different sizes and shapes of the canals (the form factor).
From the obtained image the auto correlation function (ACF) is obtained. The auto correlation function is a standard function to describe order in a structure with two phases [149], e.g. objects dispersed in a matrix. The ACF has been used to analyze biological structures such as the arrangement of tubules in dentin [150] and capillaries in the prostate gland [151]. The ACF is calculated by subtracting the area fraction ϕ from the calculated two-point correlation function, $S_2(r)$. The latter quantifies the probability to find two black pixels in the image at a distance r. The ACF yields

$$ACF(r) = S_2(r) - \phi^2 \tag{5.1}$$

The subtraction of ϕ has the convenient consequence that the ACF approaches zero for large values of r indicating the loss of spatial correlation over large distances. Figure 5.2 shows three instructive examples of extremes in terms of order of circular canals depicted in black (Figure 5.2, middle row) and their corresponding ACFs (Figure 5.2, top). All three arrangements contain the same number (and size) of canals, but they differ clearly in their spatial arrangement, ranging from perfect (quadratic) order (left) to a completely random arrangement of the canals (right). The central image is an actual binarized image of cortical horse bone. For small distances, the ACF is almost identical for all cases, since only information about the average size and shape of the objects is rendered. The location of the first zero of the ACF is related to the average size of the canals. The first minimum gives the distance at which it is least likely to find another neighboring canal. For a random arrangement, the ACF becomes zero for values larger than the diameter of the canals, corresponding to a lack of correlation between the positions of the canals (Figure 5.2, top row, right). Deviations from zero are only due to the finite size of the image, which is comparable to the size of the experimental images. The ACF for the perfectly ordered arrangement of canals displays clear oscillations with well-defined peaks. The position of the first peak corresponds to the smallest distance between the centers of two canals. Likewise, the position of the second peak, third peak and so forth correspond to the distance between the second nearest canals, third nearest canals, and so forth. The partial order in the arrangement of canals is reflected in the oscillations of the ACF (Figure 5.2, top row, center). The oscillation dampens out rather quickly, showing only two clear peaks, which suggests that the order in the

osteonal arrangement is relatively short-ranged, over a distance of ≈ 500 μm.
The second function used to investigate the structural organization of osteons is the shortest distance distribution (SDD). The SDD describes how far away a region of bone material is from its nearest canal. As the blood vessel within the canal serves as source of nutrients for bone tissue, the SDD has a direct physiological significance; it reflects the efficiency of the nutrient supply to the bone. The starting point of the calculation of the SDD is the shortest distance map (Figure 5.2 right), which gives the minimum distance for each bone pixel to the nearest surface of a canal. The SDD is then the

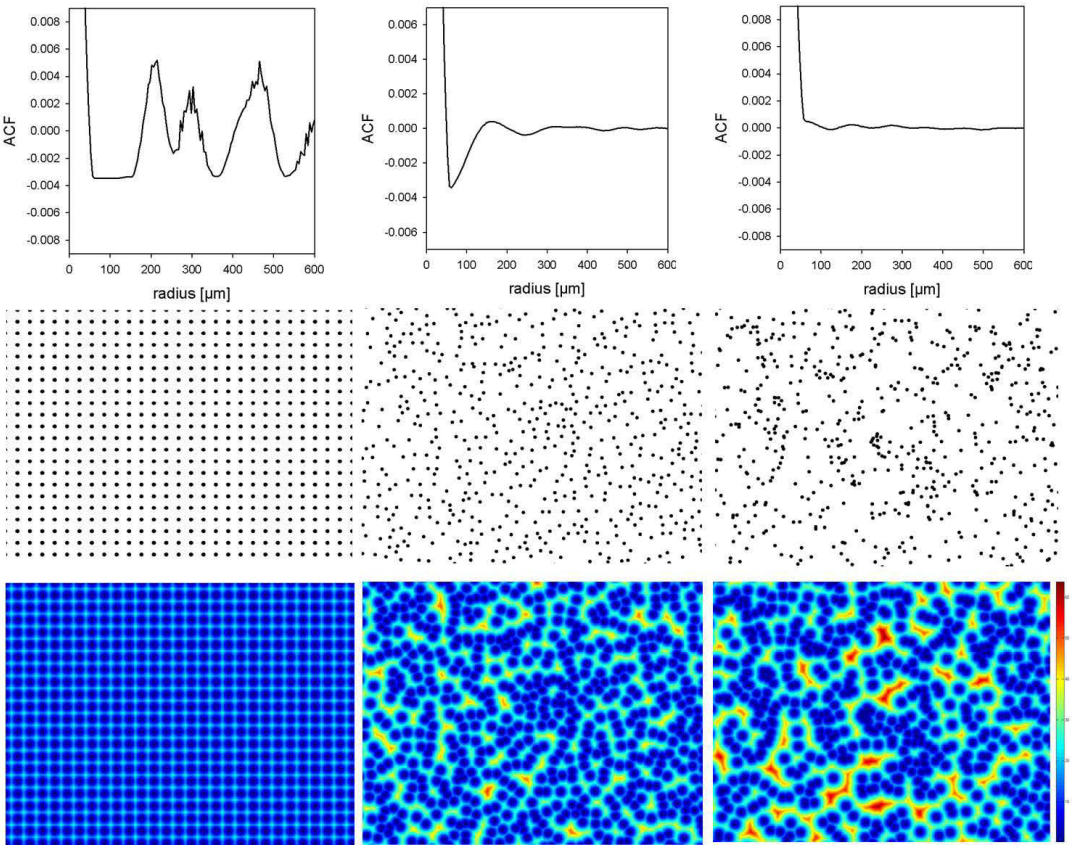

Figure 5.2: ACFs (upper row) and shortest distance maps (lower row) for three types of images (middle row). All three images have the same area fraction of black circles. The left column describes a perfectly periodic organization of the black circles, while the right column refers to a completely random distribution. The middle column refers to the arrangement of canals as observed in an horse image, where the canals are replaced by black circles of uniform size. The shortest distance maps are used to calculate the SDDs between the canals and the surrounding bone. Adapted from [148] with permission.

frequency distribution (or histogram) of distances found within such an image.
In the model the same density of canals as in the experimental image is used. This allows a direct comparison with experimental results. With such a model the influence of a larger or smaller exclusion radii on the ordered arrangement of the osteons can be investigated. Or in other words how a varying "repulsion" between osteons influences their order. A certain variability of the exclusion radius has to be introduced to be in agreement with experiments which is assumed to be normally distributed, with the standard deviation σ as second parameter of the model.
Figure 5.3 shows the influence of the two parameters of the normal distribution, the mean (=exclusion radius) μ and its standard deviation σ, on the auto correlation function (ACF). An increase in μ (Figure 5.3, right) increases the order, as demonstrated by the deep first minimum and clear first maximum of the ACF. An increase in σ (Figure 5.3, left) reduces the order. In addition, the slope between the first minimum and first maximum distinctly increases as σ increases. The results were averaged over multiple simulation runs.
The parameters in the simulation are adapted to model the order in bone tissue of the

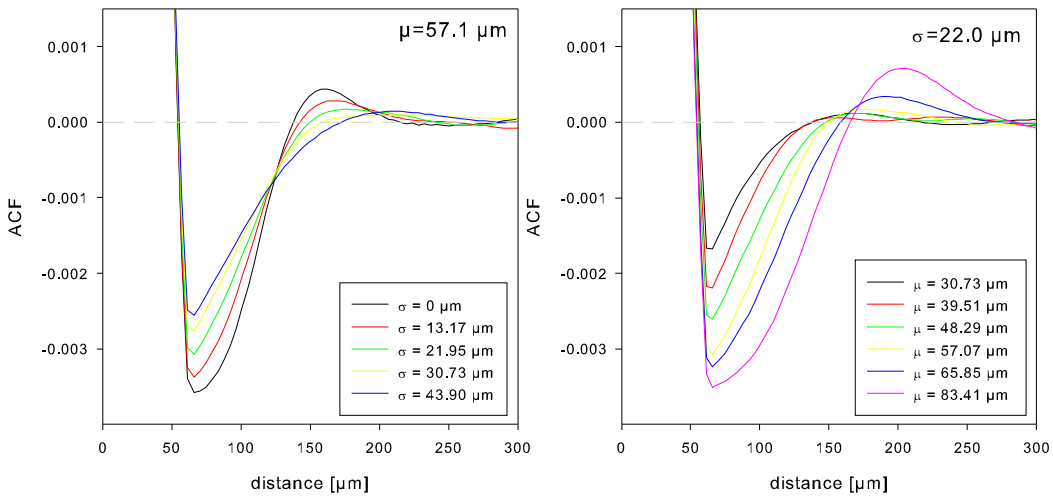

Figure 5.3: ACFs of simulated images of the arrangement of canals. The exclusion radii of the osteons placed in the image following a RSA process are assumed normally distributed, with mean μ and standard deviation σ. The influence on the ACF function is different in the case of constant σ and different values of μ (left), or constant μ and different values of σ (right).

horse radius and the different anatomical locations in the metacarpal of the horse. The best matching parameters for the exclusion radius R_{excl} and the corresponding standard

deviation σ are chosen by calculation of the mean squared error (MSE). The MSE is used to quantify the difference between the measured and the simulated function. It is calculated with the following equation

$$MSE = \frac{1}{N}\sqrt{\sum_{i=1}^{N}(ACF_{exp} - ACF_{sim})^2} \tag{5.2}$$

where N is the number of observations and corresponds to the number of entries in the ACF. The error is calculated for ACFs for a maximum distance of 300 μm. MSE ranges from 0 to 1 with 0 indicating the smallest and 1 the largest difference between simulation and experiment. For all chosen R_{excl} and corresponding σ the MSE had a value in the order of 10^{-4}.

5.2 Results - Spatial arrangement of osteons

From the experimental and simulated images the autocorrelation function and the shortest distance distribution are calculated in order to quantify the spatial arrangement of osteons in bone. The different anatomical directions in the radius (see Figure 2.8 for the definition of bone names) do not show distinguishable ACFs (not shown) considering the error bars of the measurement. Therefore only the averaged ACF is considered for the radius. The analysis of the cranial and lateral location in the metacarpal bone of the horse showed clear differences. Their first minimum of the ACF is almost identical. Yet the slope of the ACF from the first minimum to the following maximum is steeper for the cranial direction than for the lateral direction. This results in a lower first maximum occurring at a smaller distance.

In the simulation the exclusion radius and the standard deviation are varied. The ACF of the lateral location of the metacarpus in the horse show good agreement with the simulated ACF when an exclusion radius of approximately three times the canal radius ($R_{ca} = 28.14\mu m$) is chosen. The corresponding standard deviation of the exclusion radii is $0.58 \cdot R_{ca}$ (Figure 5.4, left). The simulation, however, predicts a slightly deeper first minimum than measured experimentally. The same exclusion radius of the lateral location is obtained for the ACF of the averaged three locations (medial, lateral and cranial) in the horse radius. Yet its standard deviation is larger and is $1.4 \cdot R_{ca}$. Finally, the best agreement with the experimental ACF for the cranial location of the metacarpal is obtained by choosing the same small standard deviation as for the lateral location ($\sigma = 0.58 \cdot R_{ca}$), but with an exclusion radius of only $2.18 \cdot R_{ca}$.

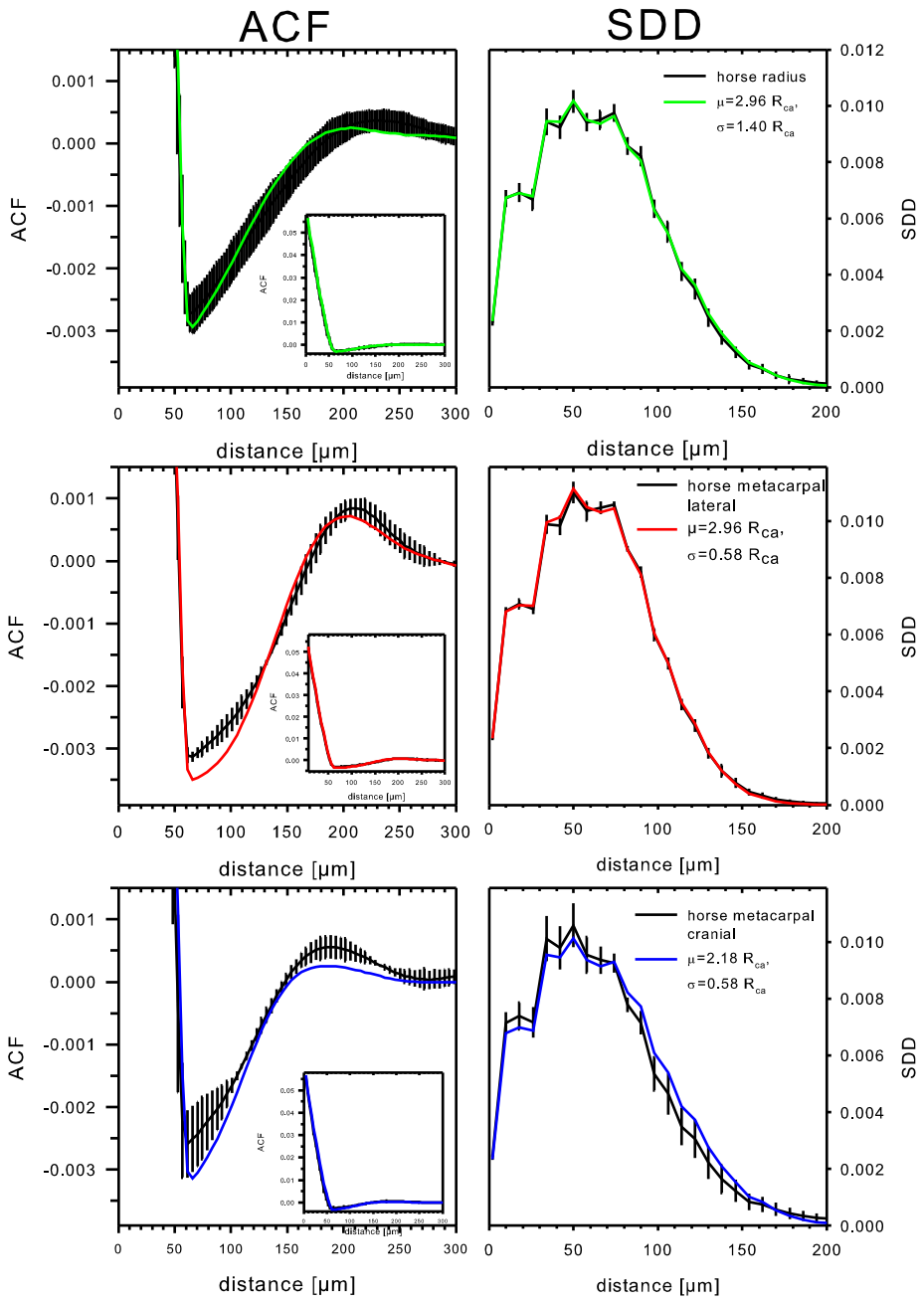

Figure 5.4: Left: Zoom of the simulated ACF that fits best the experimental ACF is plotted as a continuous line. The experimental ACF is in black and error bars denote the standard deviation. In the small inset the entire range of ACF demonstrates the good agreement between experiment and simulation. Right: Comparison of experimental and simulated SDD of the lateral location in the horse bone.

The simulated images are also evaluated with respect to the SDDs. With the same values of R_{excl} and σ good agreement of the experimental and simulated SDD is achieved. In Figure 5.4 right the SDDs are shown. The larger order in the osteonal arrangement of the lateral part of the horse metacarpal (middle) compared to the cranial part (bottom) is reflected by a slightly narrower SDD. The bone material in the lateral location is thus on average closer to a blood vessel than in the cranial cortical bone. All the experimentally obtained SDDs of the osteonal arrangement lie between the extreme cases of a fully ordered quadratic arrangement and a random arrangement of the canals.

5.3 Discussion

In this study the arrangement of osteons in compact bone of horses were detected and quantified. The theoretical model illustrates how the observed order in the canal arrangement can be explained by introduction of an exclusion zone. Only poor agreement could be obtained between experiment and simulation when assuming a single value of the exclusion radius. It was necessary to introduce some degree of variability into the model by assuming a normal distribution of the exclusion radii.

The physiologic interpretation of the exclusion radius would be that a new osteon could be created in an area as long as this area is not already well supplied by an existing osteon (i.e. within the so-called exclusion radius). Such a mechanism could produce a partly ordered arrangement of canals in a self-organized way. A simple biological mechanism for creating such an exclusion zone would be an inhibitory signaling factor, which migrates into the bone from the canal and would therefore exhibit a decreasing concentration gradient as the distance from the canal increases. Such factors have been proposed already in bone, for example the effect of proteins (called sclerostin) in controlling the final size of the canal [152]. A larger exclusion radius would correspond to a stronger source of the inhibitory factor at the canal.

The variability of the exclusion zone could be partly the result of the large variability in the size of the canals. Other factors that are not included in our simple model could also modify the size of the exclusion zone, for instance, differences in osteon size. While the size of the osteon is determined by the action of osteoclasts, the diameter of the canal results from the infilling of the osteoblasts. The model does not account for any interplay between the different bone cells.

Based on this model, the limit of introducing too much order in the canal arrangement by increasing the exclusion radius is that it becomes more and more difficult to find an allowed region for creating a new osteon. Similar self-organizing processes on larger

scales leading to patterning of a collection of organisms are observed in many other systems in nature. The observed order can be explained by a combination of attractive and inhibitory factors. Examples include the patterning seen in vegetation in arid regions [153], of tree density in boreal forest landscapes [154], the self-organization of nests of the African fish tilapia [155] and in the pattern formation within mussel beds [156].
The main limitation of the analysis of the spatial arrangement of osteons is the rather small number of samples (three images per anatomical location of the radius of two horses and metacarpal of one horse). Therefore from general conclusions about the order of canals in different bones has to be abstained. To draw specific firm conclusions about intraindividual, interindividual and interspecies differences, more samples have to be analyzed.
The limitations of the computational model is that once canals are placed in the model they are fixed and cannot be removed by further remodeling events. Running time dependent simulations, which introduce more realistic dynamics of bone remodeling, could show how the ordering of canals varies with time.

6 Conclusions

In this thesis different influences on the mineralization and the remodeling process were investigated and quantified. Starting with the bone mineralization density distribution (BMDD), which is the result of these two processes, it could be shown that the measurement process has only a minor effect on the width of the BMDD, once the acquisition time is $t > 100\ s$. The resulting corrected BMDD of this study is a bit narrower than the BMDD used until now. Also the averaging of the 52 measured BMDDs which is performed to obtain the reference BMDD, changed the width only to a small extend. In the entire study the peak position remained unchanged. Therefore it can be concluded that the reference BMDD was confirmed as good tool to diagnose bone diseases.
In the following the BMDD model [14] was modified in such a way that the effect of an increased/decreased mineralization process on the BMDD could be investigated. The obtained effects on the BMDD were compared to effects resulting from a decreased/increased remodeling process. The outcome of this study was that it is difficult to distinguish which effect causes the changes in the BMDD. For example, when the BMDD shifts to lower mineral contents then in both simulations, i.e. decreased mineralization and increased remodeling, the BMDD becomes more heterogeneous. For a right shift both simulations reveal more homogeneous distributions. The only significant difference between the two processes on the BMDD lies in the time evolution. For a left shift an increased remodeling rate reaches faster a steady state, while this is the case for the mineralization process when the BMDD shifts to the right. A suggestion to distinguish these effects with qBEI would be to make additional measurements at a later time point, if possible.
The mineralization process could be quantified in the living animal by evaluation of micro-computed tomography images. The evaluation showed that the mineralization process is faster in newly formed than in quiescent bone. This is in agreement with proposed theories in literature and further confirms the mineralization law which was obtained by solving the BMDD model [14]. Furthermore it could be demonstrated that the mechanical stimulus on the bone accelerates the mineralization process. For the first time it could be shown *in vivo* that bone demineralizes before it gets resorbed. In

conclusion micro-computed tomography is a remarkable new method to study dynamic processes in bone.

In the last section of this thesis the spatial arrangement of osteons was studied in the cortical bone of horses. The study was a combination of image analysis and computer simulation. It was found that the canals of the osteons are partially ordered. The observed order could be reproduced by a computer simulation using an exclusion radius in which the new osteons are unlikely to be formed in the close vicinity of another one. Furthermore the found order in the bone could be related to a physiological interpretation. A new osteon could be created in an area as long as this area is not already well supplied by an existing osteon. The proposed analysis method shows an approach of how static images of bone and its osteonal arrangement can be used to obtain information about how the remodeling process is controlled.

Appendix A - List of Publications

Manuscripts

R. Shahar, C. Lukas, S. Papo, J. W.C. Dunlop, and R. Weinkamer.
"Characterization of the Spatial Arrangement of Secondary Osteons in the Diaphysis of Equine and Canine Long Bones"
The Anatomical Record 294:1093-1102 (2011)

C. Lukas, P. Kollmannsberger, D. Ruffoni, P. Roschger, P. Fratzl, and R. Weinkamer.
"The Heterogeneous Mineral Content of Bone-Using Stochastic Arguments and Simulations to Overcome Experimental Limitations"
Journal of Statistical Physics 144:316-331 (2011)

C. Lukas, D. Ruffoni, F. Lambers, F.A. Schulte, G.A. Kuhn, P. Kollmannsberger, R. Weinkamer, and R. Müller.
"Quantification Of The Interplay Between Mineralization And Remodeling In Trabecular Bone Assessed By *In Vivo* Micro-Computed Tomography"
To be submitted

C. Lukas, P. Kollmannsberger, P. Roschger, D. Ruffoni, P. Fratzl, and R. Weinkamer.
"Effects of disturbed mineralization kinetics on the bone mineralization density distribution compared to effects resulting from turnover changes"
To be submitted

Talks

C. Lukas, H. Engel, P. Fratzl, P. Roschger, K. Klaushofer, and R. Weinkamer.
DPG Spring Meeting 2009, Dresden, Germany

"Mineralization kinetics and heterogeneity of mineral content in bone"

C. Lukas, P. Fratzl, P. Roschger, K. Klaushofer, and R. Weinkamer.
IV International Conference on Computational Bioengineering 2009, Bertinoro, Italy
Simulation of the mineral heterongeneity of bone in health and disease

C. Lukas, R. Shahar, J. Dunlop, S. Papo, and R. Weinkamer.
DPG Spring Meeting 2010, Regensburg, Germany
"The ordered arrangement of secondary osteons in long bones"

Poster Presentations

R. Weinkamer, J. Dunlop, S. Papo, C. Lukas, and R. Shahar.
IBMS Davos Workshop: Bone Biology and Therapeutics, 2010, Davos, Switzerland
"Quantification of the Order in the Spatial Arrangement of Secondary Osteons in Equine and Canine Long Bones"

C. Lukas, P. Kollmannsberger, D. Ruffoni, P. Roschger, P. Fratzl, and R. Weinkamer.
3rd Joint Meeting of the European Calcified Tissue Society & the International Bone and Mineral Society 2011, Athens, Greece
"The Effect of a Disturbed Mineralization Process on the Bone Mineralization Density Distribution (BMDD)"

C. Lukas, F. Lambers, D. Ruffoni, F.A. Schulte, G.A. Kuhn, P. Kollmannsberger, R. Weinkamer, R. Müller.
3rd Joint Meeting of the European Calcified Tissue Society & the International Bone and Mineral Society 2011, Athens, Greece
"Quantification Of The Interplay Between Mineralization And Remodeling In Trabecular Bone Assessed By *In Vivo* Micro-Computed Tomography"

Appendix B - Lukas et al. 2011, Journal of Statistical Physics

Find the article here!

Appendix C - Shahar et al. 2011,The Anatomical Record

Find the article here!

Appendix D - Lukas et al. 2012, Manuscript

Bibliography

[1] Jae-Young Rho, Liisa Kuhn-Spearing, and Peter Zioupos. Mechanical properties and the hierarchical structure of bone. *Medical Engineering & Physics*, 20(2):92 – 102, 1998.

[2] P. Fratzl and R. Weinkamer. Nature's hierarchical materials. *Progress in Materials Science*, 52(8):1263–1334, 2007.

[3] S. Weiner and H. D. Wagner. The material bone: Structure mechanical function relations. *Annual Review Of Materials Science*, 28:271–298, 1998.

[4] E. Seeman. Bone quality: the material and structural basis of bone strength. *Journal of Bone and Mineral Metabolism*, 26:1–8, 2008.

[5] A. G. Robling, A. B. Castillo, and C. H. Turner. Biomechanical and molecular regulation of bone remodeling. *Annual Review of Biomedical Engineering*, 8:455–498, 2006.

[6] P. Roschger, E. P. Paschalis, P. Fratzl, and K. Klaushofer. Bone mineralization density distribution in health and disease. *Bone*, 42(3):456–466, 2008.

[7] E. Seeman and P. D. Delmas. Mechanisms of disease - bone quality - the material and structural basis of bone strength and fragility. *New England Journal of Medicine*, 354(21):2250–2261, 2006.

[8] G. Boivin and P. J. Meunier. The mineralization of bone tissue: a forgotten dimension in osteoporosis research. *Osteoporosis International*, 14:S19–S24, 2003.

[9] P. Fratzl, H. S. Gupta, E. P. Paschalis, and P. Roschger. Structure and mechanical quality of the collagen-mineral nano-composite in bone. *Journal Of Materials Chemistry*, 14(14):2115–2123, 2004.

[10] D. Ruffoni, P. Fratzl, P. Roschger, R. Phipps, K. Klaushofer, and R. Weinkamer. Effect of temporal changes in bone turnover on the bone mineralization density

distribution: A computer simulation study. *Journal of Bone and Mineral Research*, 23(12):1905–1914, 2008.

[11] R. Müller, T. Hildebrand, H. J. Häuselmann, and P. Rüegsegger. In vivo reproducibility of three-dimensional structural properties of noninvasive bone biopsies using 3d-pqct. *Journal of Bone and Mineral Research*, 11(11):1745–1750, 1996.

[12] A. J. Burghardt, G. J. Kazakia, A. Laib, and S. Majumdar. Quantitative assessment of bone tissue mineralization with polychromatic micro-computed tomography. *Calcified Tissue International*, 83(2):129–138, 2008.

[13] F. A. Schulte, F. M. Lambers, G. Kuhn, and R. Müller. In vivo micro-computed tomography allows direct three-dimensional quantification of both bone formation and bone resorption parameters using time-lapsed imaging. *Bone*, 48(3):433–442, 2011.

[14] D. Ruffoni, P. Fratzl, P. Roschger, K. Klaushofer, and R. Weinkamer. The bone mineralization density distribution as a fingerprint of the mineralization process. *Bone*, 40(5):1308–1319, 2007.

[15] J.D. Currey. *Bones-Structure and Mechanics*. Princeton University Press, 2002.

[16] Tor Hildebrand, Andres Laib, Ralph Müller, Jan Dequeker, and Peter Rüegsegger. Direct three-dimensional morphometric analysis of human cancellous bone: Microstructural data from spine, femur, iliac crest, and calcaneus. *Journal of Bone and Mineral Research*, 14(7):1167–1174, 1999.

[17] I. Singh. Architecture of cancellous bone. *Journal of Anatomy*, 127(OCT):305–310, 1978.

[18] W.S.S. Jee. *The Bone Mechanis Handbook- Section I Basic Biology*. CRC Press, 2 edition, 2001.

[19] P. Lips, P. Courpron, and P. J. Meunier. Mean wall thickness of trabecular bone packets in the human iliac crest: Changes with age. *Calcified Tissue International*, 26:13–17, 1978.

[20] P. Roschger, H. Plenk, K. Klaushofer, and J. Eschberger. A new scanning electron-microscopy approach to the quantification of bone-mineral distribution - backscattered electron image grey-levels correlated to calcium k-alpha-line intensities. *Scanning Microscopy*, 9(1):75–88, 1995.

[21] W. Wagermaier, H. S. Gupta, A. Gourrier, M. Burghammer, P. Roschger, and P. Fratzl. Spiral twisting of fiber orientation inside bone lamellae. *Biointerphases*, 1:1–5, 2006.

[22] S. Weiner, T. Arad, I. Sabanay, and W. Traub. Rotated plywood structure of primary lamellar bone in the rat: Orientations of the collagen fibril arrays. *Bone*, 20(6):509 – 514, 1997.

[23] S. Rinnerthaler, P. Roschger, H. F. Jakob, A. Nader, K. Klaushofer, and P. Fratzl. Scanning small angle x-ray scattering analysis of human bone sections. *Calcified Tissue International*, 64(5):422–429, 1999.

[24] P. Roschger, B. M. Grabner, S. Rinnerthaler, W. Tesch, M. Kneissel, A. Berzlanovich, K. Klaushofer, and P. Fratzl. Structural development of the mineralized tissue in the human l4 vertebral body. *Journal of Structural Biology*, 136(2): 126–136, 2001.

[25] A.J. Hodge and J.A. Petruska. *Aspects of protein structure. In Ramachandran.* New York: Academic Press, 1963.

[26] Wolfie Traub, Talivion Arad, and Stephen Weiner. Origin of mineral crystal growth in collagen fibrils. *Matrix*, 12(4):251 – 255, 1992.

[27] W.J. Landis, M.J. Song, A. Leith, L. McEwen, and B.F. McEwen. Mineral and organic matrix interaction in normally calcifying tendon visualized in three dimensions by high-voltage electron microscopic tomography and graphic image reconstruction. *Journal of Structural Biology*, 110(1):39 – 54, 1993.

[28] S. Mann. *Biomineralization. Principles and concepts in bioinorganic materials chemistry.* Oxford University Press, 2001.

[29] P. Fratzl, S. Schreiber, and A. Boyde. Characterization of bone mineral crystals in horse radius by small-angle x-ray scattering. *Calcified Tissue International*, 58 (5):341–346, 1996.

[30] P. Fratzl, N. FratzlZelman, K. Klaushofer, G. Vogl, and K. Koller. Nucleation and growth of mineral crystals in bone studied by small-angle x-ray-scattering. *Calcified Tissue International*, 48(6):407–413, 1991.

[31] Melvin J. Glimcher. Bone: Nature of the calcium phosphate crystals and cellular, structural, and physical chemical mechanisms in their formation. *Reviews in Mineralogy and Geochemistry*, 64(1):223–282, 2006.

[32] D. B. Burr. The contribution of the organic matrix to bone's material properties. *Bone*, 31(1):8–11, 2002.

[33] M. F. Ashby, L. J. Gibson, U. Wegst, and R. Olive. The mechanical-properties of natural materials.1. material property charts. *Proceedings Of The Royal Society Of London Series A-Mathematical And Physical Sciences*, 450:123–140, 1995.

[34] I. Jager and P. Fratzl. Mineralized collagen fibrils: A mechanical model with a staggered arrangement of mineral particles. *Biophysical Journal*, 79(4):1737–1746, 2000.

[35] H. J. Gao, B. H. Ji, I. L. Jager, E. Arzt, and P. Fratzl. Materials become insensitive to flaws at nanoscale: Lessons from nature. *Proceedings of the National Academy of Sciences of the United States of America*, 100(10):5597–5600, 2003.

[36] R. Huiskes. If bone is the answer, then what is the question? *Journal of Anatomy*, 197:145–156, 2000.

[37] Wilhelm Roux. *Der Kampf der Teile im Organismus.* Leipzig: Engelmann, 1881.

[38] Julius Wolff. *Das Gesetz der Transformation der Knochen.* Berlin: A. Hirschwald, 1892.

[39] D.B. Burr. Targeted and nontargeted remodeling. *Bone*, 30(1):2 – 4, 2002.

[40] A. M. Parfitt. Targeted and nontargeted bone remodeling: relationship to basic multicellular unit origination and progression. *Bone*, 30:5–7, 2002.

[41] A. M. Parfitt. Misconceptions (3): calcium leaves bone only by resorption and enters only by formation. *Bone*, 33(3):259–263, 2003.

[42] D. W. Talmage and R. V. Talmage. Calcium homeostasis: How bone solubility relates to all aspects of bone physiology. *Journal of Musculoskeletal & Neuronal Interactions*, 7(2):108–112, 2007.

[43] Lynda F. Bonewald. Osteocytes as dynamic multifunctional cells. *Annals of the New York Academy of Sciences*, 1116(1):281–290, 2007.

[44] Anna Teti and Alberta Zallone. Do osteocytes contribute to bone mineral homeostasis? osteocytic osteolysis revisited. *Bone*, 44(1):11 – 16, 2009.

[45] R. B. Martin. Porosity and specific surface of bone. *Crc Critical Reviews in Biomedical Engineering*, 10(3):179–222, 1984.

[46] S. Mori and D.B. Burr. Increased intracortical remodeling following fatigue damage. *Bone*, 14(2):103 – 109, 1993.

[47] A.M. Parfitt, G.R. Mundy, G.D. Roodman, D.E. Hughes, and B.F. Boyce. Theoretical perspective: A new model for the regulation of bone resorption, with particular reference to the effects of bisphosphonates. *Journal of Bone and Mineral Research*, 11(2):150–159, 1996.

[48] Z. H. Han, S. Palnitkar, D. S. Rao, D. Nelson, and A. M. Parfitt. Effects of ethnicity and age or menopause on the remodeling and turnover of iliac bone: Implications for mechanisms of bone loss. *Journal of Bone and Mineral Research*, 12(4):498–508, 1997.

[49] Steven L. Teitelbaum and F. Patrick Ross. Genetic regulation of osteoclast development and function. *Nat Rev Genet*, 4(8):638–649, 2003.

[50] Steven L. Teitelbaum. Bone resorption by osteoclasts. *Science*, 289(5484):1504–1508, 2000.

[51] Deborah V. Novack and Steven L. Teitelbaum. The osteoclast: Friend or foe? *Annual Review of Pathology: Mechanisms of Disease*, 3(1):457–484, 2008.

[52] E. F. Eriksen. Normal and pathological remodeling of human trabecular bone - 3-dimensional reconstruction of the remodeling sequence in normals and in metabolic bone-disease. *Endocrine Reviews*, 7(4):379–408, 1986.

[53] A. M. Parfitt. Osteonal and hemi-osteonal remodeling: The spatial and temporal framework for signal traffic in adult human bone. *Journal of Cellular Biochemistry*, 55(3):273–286, 1994.

[54] B. L. Riggs and A. M. Parfitt. Drugs used to treat osteoporosis: The critical need for a uniform nomenclature based on their action on bone remodeling. *Journal of Bone and Mineral Research*, 20(2):177–184, 2005.

[55] Harold M. Frost. Tetracycline-based histological analysis of bone remodeling. *Calcified Tissue International*, 3:211–237, 1969.

[56] E.F Eriksen, F Melsen, E Sod, I Barton, and A Chines. Effects of long-term risedronate on bone quality and bone turnover in women with postmenopausal osteoporosis. *Bone*, 31(5):620 – 625, 2002.

[57] Z. Jaworski. Lamellar bone turnover system and its effector organ. *Calcified Tissue International*, 36:S46–S55, 1984.

[58] R. B. Martin. On the significance of remodeling space and activation rate changes in bone remodeling. *Bone*, 12(6):391–400, 1991.

[59] C. Lukas, P. Kollmannsberger, D. Ruffoni, P. Roschger, P. Fratzl, and R. Weinkamer. The heterogeneous mineral content of bone-using stochastic arguments and simulations to overcome experimental limitations. *Journal of Statistical Physics*, 144(2):316–331, 2011.

[60] P. Roschger, B. M. Grabner, P. Messmer, D. W. Dempster, F. Cosman, J. Nieves, R. Lindsay, J. P. Bilezikian, E. S. Kurland, E. Shane, P. Fratzl, and K. Klaushofer. Influence of intermittent pth treatment on mineral distribution in the human ilium: A paired biopsy study before and after treatment. *Journal of Bone and Mineral Research*, 16:S179–S179, 2001.

[61] R. P. Heaney, A. J. Yates, and A. C. Santora. Bisphosphonate effects and the bone remodeling transient. *Journal Of Bone And Mineral Research*, 12(8):1143–1151, 1997.

[62] A. M. Parfitt. Bone remodeling and bone loss - understanding the pathophysiology of osteoporosis. *Clinical Obstetrics and Gynecology*, 30(4):789–811, 1987.

[63] Tamara A. Franz-Odendaal, Brian K. Hall, and P. Eckhard Witten. Buried alive: How osteoblasts become osteocytes. *Developmental Dynamics*, 235(1):176–190, 2006.

[64] Michael Kerschnitzki, Wolfgang Wagermaier, Paul Roschger, Jong Seto, Ron Shahar, Georg N. Duda, Stefan Mundlos, and Peter Fratzl. The organization of the osteocyte network mirrors the extracellular matrix orientation in bone. *Journal of Structural Biology*, 173(2):303 – 311, 2011.

[65] E. H. Burger and J. Klein-Nulend. Mechanotransduction in bone - role of the lacuno-canalicular network. *The FASEB Journal*, 13(9001):101–112, 1999.

[66] J. Klein-Nulend, A. van der Plas, C. M. Semeins, N. E. Ajubi, J. A. Frangos, P. J. Nijweide, and E. H. Burger. Sensitivity of osteocytes to biomechanical stress in vitro. *FASEB J.*, 9(5):441–445, 1995.

[67] S. Zhao, Y. Kato, Y. Zhang, S. Harris, S. S. Ahuja, and L. F. Bonewald. Mlo-y4 osteocyte-like cells support osteoclast formation and activation. *Journal of Bone and Mineral Research*, 17(11):2068–2079, 2002.

[68] Helmut Colfen. Biomineralization: A crystal-clear view. *Nat Mater*, 9(12):960–961, 2010.

[69] S. S. Jee, L. Culver, Y. P. Li, E. P. Douglas, and L. B. Gower. Biomimetic mineralization of collagen via an enzyme-aided pilp process. *Journal of Crystal Growth*, 312(8):1249–1256, 2010.

[70] F. Nudelman, K. Pieterse, A. George, P. H. H. Bomans, H. Friedrich, L. J. Brylka, P. A. J. Hilbers, G. de With, and N. A. J. M. Sommerdijk. The role of collagen in bone apatite formation in the presence of hydroxyapatite nucleation inhibitors. *Nature Materials*, 9(12):1004–1009, 2010.

[71] Julia Mahamid, Amnon Sharir, Lia Addadi, and Steve Weiner. Amorphous calcium phosphate is a major component of the forming fin bones of zebrafish: Indications for an amorphous precursor phase. *Proceedings of the National Academy of Sciences*, 105(35):12748–12753, 2008.

[72] J. Mahamid, B. Aichmayer, E. Shimoni, R. Ziblat, C. H. Li, S. Siegel, O. Paris, P. Fratzl, S. Weiner, and L. Addadi. Mapping amorphous calcium phosphate transformation into crystalline mineral from the cell to the bone in zebrafish fin rays. *Proceedings of the National Academy of Sciences of the United States of America*, 107(14):6316–6321, 2010.

[73] Elia Beniash, Rebecca A. Metzler, Raymond S.K. Lam, and P.U.P.A. Gilbert. Transient amorphous calcium phosphate in forming enamel. *Journal of Structural Biology*, 166(2):133 – 143, 2009.

[74] Julia Mahamid, Amnon Sharir, Dvir Gur, Elazar Zelzer, Lia Addadi, and Steve Weiner. Bone mineralization proceeds through intracellular calcium phosphate loaded vesicles: A cryo-electron microscopy study. *Journal of Structural Biology*, 174(3):527 – 535, 2011.

[75] J. Mahamid, L. Addadi, and S. Weiner. Crystallization pathways in bone. *Cells Tissues Organs*, 194(2-4):92–97, 2011.

[76] Heinz Lowenstam and Stephen Weiner. *On Biomineralization*. Oxford University Press, 1989.

[77] J. D. Pasteris, B. Wopenka, and E. Valsami-Jones. Bone and tooth mineralization: Why apatite? *Elements*, 4(2):97–104, 2008.

[78] Anke Märten, Peter Fratzl, Oskar Paris, and Paul Zaslansky. On the mineral in collagen of human crown dentine. *Biomaterials*, 31(20):5479 – 5490, 2010.

[79] I. Zizak, P. Roschger, O. Paris, B. M. Misof, A. Berzlanovich, S. Bernstorff, H. Amenitsch, K. Klaushofer, and P. Fratzl. Characteristics of mineral particles in the human bone/cartilage interface. *Journal of Structural Biology*, 141(3): 208–217, 2003.

[80] Shmuel Bentov, Paul Zaslansky, Ali Al-Sawalmih, Admir Masic, Peter Fratzl, Amir Sagi, Amir Berman, and Barbara Aichmayer. Enamel-like apatite crown covering amorphous mineral in a crayfish mandible. *Nat Commun*, 3:839, 2012.

[81] A. Boskey. Bone mineral crystal size. *Osteoporosis International*, 14:16–21, 2003.

[82] P. Chavassieux, E. Seeman, and P. D. Delmas. Insights into material and structural basis of bone fragility from diseases associated with fractures: How determinants of the biomechanical properties of bone are compromised by disease. *Endocrine Reviews*, 28(2):151–164, 2007.

[83] P. Fratzl, O. Paris, K. Klaushofer, and W. J. Landis. Bone mineralization in an osteogenesis imperfecta mouse model studied by small-angle x-ray scattering. *Journal of Clinical Investigation*, 97(2):396–402, 1996.

[84] N. Fratzl-Zelman, R. Morello, B. Lee, F. Rauch, F.H. Glorieux, B.M. Misof, K. Klaushofer, and P. Roschger. Crtap deficiency leads to abnormally high bone matrix mineralization in a murine model and in children with osteogenesis imperfecta type vii. *Bone*, 46(3):820 – 826, 2010.

[85] Jochen G. Hofstaetter, Stefan G. Hofstaetter, Kamilla Nawrot-Wawrzyniak, Helmut Hiertz, Josef G. Grohs, Klemens Trieb, Reinhard Windhager, Klaus Klaushofer, and Paul Roschger. Mineralization pattern of vertebral bone material following fragility fracture of the spine. *Journal of Orthopaedic Research*, 30(7): 1089–1094, 2012.

[86] P. Roschger, I. Manjubala, N. Zoeger, F. Meirer, R. Simon, C. H. Li, N. Fratzl-Zelman, B. M. Misof, E. P. Paschalis, C. Streli, P. Fratzl, and K. Klaushofer. Bone material quality in transiliac bone biopsies of postmenopausal osteoporotic

women after 3 years of strontium ranelate treatment. *Journal of Bone and Mineral Research*, 25(4):891–900, 2010.

[87] C. H. Li, O. Paris, S. Siegel, P. Roschger, E. P. Paschalis, K. Klaushofer, and P. Fratzl. Strontium is incorporated into mineral crystals only in newly formed bone during strontium ranelate treatment. *Journal of Bone and Mineral Research*, 25(5):968–975, 2010.

[88] M. G. Mullender and R. Huiskes. Proposal for the regulatory mechanism of wolff's law. *Journal of Orthopaedic Research*, 13(4):503–512, 1995.

[89] Rik Huiskes, Ronald Ruimerman, G. Harry van Lenthe, and Jan D. Janssen. Effects of mechanical forces on maintenance and adaptation of form in trabecular bone. *Nature*, 405(6787):704–706, 2000.

[90] R. Weinkamer, M. A. Hartmann, Y. Bréchet, and P. Fratzl. Stochastic lattice model for bone remodeling and aging. *Physical Review Letters*, 93(22):–, 2004.

[91] J. W. C. Dunlop, M. A. Hartmann, Y. J. Brechet, P. Fratzl, and R. Weinkamer. New suggestions for the mechanical control of bone remodeling. *Calcified Tissue International*, 85(1):45–54, 2009.

[92] D. Thompson. *On Growth and Form*. Cambridge Press, p.985, 1961 (originally published 1917).

[93] H. M. Frost. Bone mass and the mechanostat - a proposal. *Anatomical Record*, 219(1):1–9, 1987.

[94] Rik Huiskes. *Bone Research in Biomechanics*. IOS Press,p.33, 1997.

[95] Tait S. Smith, R. Bruce Martin, Mont Hubbard, and Brian K. Bay. Surface remodeling of trabecular bone using a tissue level model. *Journal of Orthopaedic Research*, 15(4):593–600, 1997.

[96] Bríanne M. Mulvihill and Patrick J. Prendergast. An algorithm for bone mechanoresponsiveness: implementation to study the effect of patient-specific cell mechanosensitivity on trabecular bone loss. *Computer Methods in Biomechanics and Biomedical Engineering*, 11(5):443–451, 2008.

[97] René F.M. van Oers, Bert van Rietbergen, Keita Ito, Rik Huiskes, and Peter A.J. Hilbers. Simulations of trabecular remodeling and fatigue: Is remodeling helpful or harmful? *Bone*, 48(5):1210 – 1215, 2011.

[98] M. A. Hartmann, J. W. C. Dunlop, Y. J. M. Bréchet, P. Fratzl, and R. Weinkamer. Trabecular bone remodelling simulated by a stochastic exchange of discrete bone packets from the surface. *Journal of the Mechanical Behavior of Biomedical Materials*, 4(6):879–887, 2011.

[99] L. Mulder, J. H. Koolstra, J. M. J. den Toonder, and T. M. G. J. van Eijden. Intratrabecular distribution of tissue stiffness and mineralization in developing trabecular bone. *Bone*, 41(2):256–265, 2007.

[100] H. Follet, G. Boivin, C. Rumelhart, and P. J. Meunier. The degree of mineralization is a determinant of bone strength: a study on human calcanei. *Bone*, 34(5):783–789, 2004.

[101] G. Boivin, Y. Bala, A. Doublier, D. Farlay, L. G. Ste-Marie, P. J. Meunier, and P. D. Delmas. The role of mineralization and organic matrix in the microhardness of bone tissue from controls and osteoporotic patients. *Bone*, 43(3):532–538, 2008.

[102] Valérie Bousson, Catherine Bergot, Yan Wu, Erwan Jolivet, Liang Qiang Zhou, and Jean-Denis Laredo. Greater tissue mineralization heterogeneity in femoral neck cortex from hip-fractured females than controls. a microradiographic study. *Bone*, 48(6):1252 – 1259, 2011.

[103] Aymeric Larrue, Aline Rattner, Zsolt-Andrei Peter, Cécile Olivier, Norbert Laroche, Laurence Vico, and Françoise Peyrin. Synchrotron radiation micro-ct at the micrometer scale for the analysis of the three-dimensional morphology of microcracks in human trabecular bone. *PLoS ONE*, 6(7):e21297, 07 2011.

[104] D. M. L. Cooper, B. Erickson, A.G. Peele, K. Hannah, C. D. L. Thomas, and J. G. Clement. Visualization of 3d osteon morphology by synchrotron radiation micro-ct. *Journal of Anatomy*, 219(4):481–489, 2011.

[105] A. Boyde and S. A. Reid. A new method of scanning electron-microscopy for imaging biological tissues. *Nature*, 302(5908):522–523, 1983.

[106] J. G. Skedros, R. D. Bloebaum, K. N. Bachus, T. M. Boyce, and B. Constantz. Influence of mineral-content and composition on graylevels in backscattered electron images of bone. *Journal of Biomedical Materials Research*, 27(1):57–64, 1993.

[107] R. D. Bloebaum, J. G. Skedros, E. G. Vajda, K. N. Bachus, and B. R. Constantz. Determining mineral content variations in bone using backscattered electron imaging. *Bone*, 20(5):485–490, 1997.

[108] P. Roschger, H. S. Gupta, A. Berzanovich, G. Ittner, D. W. Dempster, P. Fratzl, F. Cosman, M. Parisien, R. Lindsay, J. W. Nieves, and K. Klaushofer. Constant mineralization density distribution in cancellous human bone. *Bone*, 32(3):316–323, 2003.

[109] B. Busse, M. Hahn, M. Soltau, J. Zustin, K. Puschel, G. N. Duda, and M. Amling. Increased calcium content and inhomogeneity of mineralization render bone toughness in osteoporosis: Mineralization, morphology and biomechanics of human single trabeculae. *Bone*, 45(6):1034–1043, 2009.

[110] Dale R. Sumner, James M. Bryan, Robert M. Urban, and Jerome R. Kuszak. Measuring the volume fraction of bone ingrowth: A comparison of three techniques. *Journal of Orthopaedic Research*, 8(3):448–452, 1990.

[111] S. Nuzzo, M. H. Lafage-Proust, E. Martin-Badosa, G. Boivin, T. Thomas, C. Alexandre, and F. Peyrin. Synchrotron radiation microtomography allows the analysis of three-dimensional microarchitecture and degree of mineralization of human iliac crest biopsy specimens: Effects of etidronate treatment. *Journal of Bone and Mineral Research*, 17(8):1372–1382, 2002.

[112] M. Ito, S. Ejiri, H. Jinnai, J. Kono, S. Ikeda, A. Nishida, K. Uesugi, N. Yagi, M. Tanaka, and K. Hayashi. Bone structure and mineralization demonstrated using synchrotron radiation computed tomography (sr-ct) in animal models: preliminary findings. *Journal of Bone and Mineral Metabolism*, 21(5):287–293, 2003.

[113] B. Borah, E. L. Ritman, T. E. Dufresne, S. M. Jorgensen, S. Liu, J. Sacha, R. J. Phipps, and R. T. Turner. The effect of risedronate on bone mineralization as measured by micro-computed tomography with synchrotron radiation: Correlation to histomorphometric indices of turnover. *Bone*, 37(1):1–9, 2005.

[114] P. Roschger, P. Fratzl, J. Eschberger, and K. Klaushofer. Validation of quantitative backscattered electron imaging for the measurement of mineral density distribution in human bone biopsies. *Bone*, 23(4):319–326, 1998.

[115] J.I. Goldstein, D.E. Newbury, P. Echlin, D.C. Joy, Jr. Roming, A.D., C.E. Lyman, C. Fiori, and E. Lifshin. *Scanning Electron Microscopy and X-Ray Microanalysis, 2nd ed.* Springer; 2nd edition (May 31, 1992), 1992.

[116] P. Roschger, A. Lombardi, B. M. Misof, G. Maier, N. Fratzl-Zelman, P. Fratzl, and K. Klaushofer. Mineralization density distribution of postmenopausal osteoporotic

bone is restored to normal after long-term alendronate treatment: qbei and ssaxs data from the fracture intervention trial long-term extension (flex). *Journal of Bone and Mineral Research*, 25(1):48–55, 2010.

[117] B. M. Misof, P. Roschger, F. Cosman, E. S. Kurland, W. Tesch, P. Messmer, D. W. Dempster, J. Nieves, E. Shane, P. Fratzl, K. Klaushofer, J. Bilezikian, and R. Lindsay. Effects of intermittent parathyroid hormone administration on bone mineralization density in iliac crest biopsies from patients with osteoporosis: A paired study before and after treatment. *Journal Of Clinical Endocrinology And Metabolism*, 88:1150–1156, 2003.

[118] P. Roschger, P. Fratzl, K. Klaushofer, and G. Rodan. Mineralization of cancellous bone after alendronate and sodium fluoride treatment: A quantitative backscattered electron imaging study on minipig ribs. *Bone*, 20(5):393–397, 1997.

[119] P. Fratzl, P. Roschger, N. Fratzl-Zelman, E. P. Paschalis, R. Phipps, and K. Klaushofer. Evidence that treatment with risedronate in women with postmenopausal osteoporosis affects bone mineralization and bone volume. *Calcified Tissue International*, 81(2):73–80, 2007.

[120] E. G. Vajda and J. G. Skedros. Letter to the editor. *Bone*, 24(6):619–620, 1999.

[121] P. Roschger, P. Fratzl, J. Eschberger, and K. Klaushofer. Response to the letter to the editor by e.g. vajda and j.g. skedros. *Bone*, 24(6):620–621, 1999.

[122] Martin Stauber and Ralph Müller. Micro-computed tomography: A method for the non-destructive evaluation of the three-dimensional structure of biological specimens. *Methods in Molecular Biology*, 455:273–292, May 2008.

[123] L. Mulder, J. H. Koolstra, and T. M. G. J. Van Euden. Accuracy of microct in the quantitative determination of the degree and distribution of mineralization in developing bone. *Acta Radiologica*, 45(7):769–777, 2004.

[124] Mary L Bouxsein, Stephen K Boyd, Blaine A Christiansen, Robert E Guldberg, Karl J Jepsen, and Ralph MÃ$\frac{1}{4}$ller. Guidelines for assessment of bone microstructure in rodents using micro-computed tomography. *Journal of Bone and Mineral Research*, 25(7):1468–1486, 2010.

[125] J. A. Meganck, K. M. Kozloff, M. M. Thornton, S. M. Broski, and S. A. Goldstein. Beam hardening artifacts in micro-computed tomography scanning can be reduced

by x-ray beam filtration and the resulting images can be used to accurately measure bmd. *Bone*, 45(6):1104–1116, 2009.

[126] S. Prevrhal. Beam hardening correction and quantitative micro-ct. *Proceedings of SPIE*, 5535(1):10.1117/12.559976, 2004.

[127] M. Kovacs, R. Danyi, M. Erdelyi, P. Fejerdy, and C. Dobo-Nagy. Distortional effect of beam-hardening artefacts on microct: a simulation study based on an in vitro caries model. *Oral Surgery Oral Medicine Oral Pathology Oral Radiology and Endodontology*, 108(4):591–599, 2009.

[128] L. Mulder, J. H. Koolstra, J. M. J. den Toonder, and Tmgj van Eijden. Relationship between tissue stiffness and degree of mineralization of developing trabecular bone. *Journal Of Biomedical Materials Research Part A*, 84A(2):508–515, 2008.

[129] D. J. Webster, P. L. Morley, G. H. van Lenthe, and R. Müller. A novel in vivo mouse model for mechanically stimulated bone adaptation - a combined experimental and computational validation study. *Computer Methods in Biomechanics and Biomedical Engineering*, 11:435–441, 2008.

[130] D. Webster, E. Wasserman, M. Ehrbar, F. Weber, I. Bab, and R. Müller. Mechanical loading of mouse caudal vertebrae increases trabecular and cortical bone mass-dependence on dose and genotype. *Biomechanics and Modeling in Mechanobiology*, 9:737–747, 2010.

[131] F. A. Schulte, F. M. Lambers, T. L. Müller, M Stauber, and R. Müller. Quantitative outcomes after image registration of micro-computed tomography scans critically depend on interpolation technique. *Computer Methods in Biomechanics and Biomedical Engineering*, conditionally accepted, 2011.

[132] Floor M. Lambers, Friederike A. Schulte, Gisela Kuhn, Duncan J. Webster, and Ralph Müller. Mouse tail vertebrae adapt to cyclic mechanical loading by increasing bone formation rate and decreasing bone resorption rate as shown by time-lapsed in vivo imaging of dynamic bone morphometry. *Bone*, 49(6):1340 – 1350, 2011.

[133] http://www.zoo-bilder.de/anatomie/bilder/a_skelett.gif.

[134] M. D. Abramoff, P. J. Magelhaes, and S. J. Ram. Image processing with ImageJ. *Biophotonics Int*, 11(7):36–42, 2004.

[135] I Bronstein, K. Semendjajew, G. Musiol, and H. Mühlig. *Taschenbuch der Mathematik*. Verlag Harri Deutsch, 1999.

[136] Heinz Werner Engl, Martin Hanke, and Andreas Neubauer. Regularization of inverse problems. *Mathematics and Its Applications*, 375:332, 1996.

[137] P. C. Hansen. Regularization tools version 4.0 for matlab 7.3. *Numerical Algorithms*, 46(2):189–194, 2007.

[138] G. Golub and C. Reinsch. Singular value decomposition and least squares solutions. *Numerische Mathematik*, 14(5):403–420, 1970.

[139] D. Ruffoni. *Modeling of material and architectural quality of trabecular bone*. PhD thesis, Fakultät für Mathematik und Naturwissenschaften, Universität Potsdam, September 2007.

[140] MATLAB. *version 7.10.0 (R2010a)*. The MathWorks Inc., Natick, Massachusetts, 2010.

[141] Geoffrey E. Lloyd. Atomic number and crystallographic contrast images with the sem: a review of backscattered electron techniques. *Mineralogical Magazine*, 51: 3–19, 1987.

[142] D. Meschede. *Gerthsen Physik*. Springer, 21. Auflage, 2002.

[143] J. F. Barrett and N. Keat. Artifacts in ct: Recognition and avoidance. *Radiographics*, 24(6):1679–1691, 2004.

[144] L. Mulder, J. H. Koolstra, H. W. de Jonge, and T. M. G. J. van Eijden. Architecture and mineralization of developing cortical and trabecular bone of the mandible. *Anatomy and Embryology*, 211(1):71–78, 2006.

[145] T. C. Lee, A. Staines, and D. Taylor. Bone adaptation to load: microdamage as a stimulus for bone remodelling. *Journal of Anatomy*, 201(6):437–446, 2002.

[146] R. J. Fajardo, E. Cory, N. D. Patel, A. Nazarian, A. Laib, R. K. Manoharan, J. E. Schmitz, J. M. DeSilva, L. M. MacLatchy, B. D. Snyder, and M. L. Bouxsein. Specimen size and porosity can introduce error into mu ct-based tissue mineral density measurements. *Bone*, 44(1):176–184, 2009.

[147] Julienne E.M. Brouwers, Bert van Rietbergen, and Rik Huiskes. No effects of in vivo micro-ct radiation on structural parameters and bone marrow cells in proximal

tibia of wistar rats detected after eight weekly scans. *Journal of Orthopaedic Research*, 25(10):1325–1332, 2007.

[148] R. Shahar, C. Lukas, S. Papo, J. W. C. Dunlop, and R. Weinkamer. Characterization of the spatial arrangement of secondary osteons in the diaphysis of equine and canine long bones. *Anatomical Record-Advances in Integrative Anatomy and Evolutionary Biology*, 294(7):1093–1102, 2011.

[149] S. Torquato. *Random Heterogeneous Materials: microstructure and macroscopic properties*, volume 16 of *Interdisciplinary Applied Mathematics*. New York: Springer, 2002.

[150] J. H. Kinney, J. Oliveira, D. L. Haupt, G. W. Marshall, and S. J. Marshall. The spatial arrangement of tubules in human dentin. *Journal of Materials Science: Materials in Medicine*, 12:743–751, 2001.

[151] T. Mattfeldt, S. Eckel, F. Fleischer, and V. Schmidt. Statistical analysis of reduced pair correlation functions of capillaries in the prostate gland. *Journal of Microscopy*, 223(2):107–119, 2006.

[152] Jon Power, Kenneth ES Poole, Rutger van Bezooijen, Michael Doube, Ana M Caballero-AlÃas, Clemens Lowik, Socrates Papapoulos, Jonathan Reeve, and Nigel Loveridge. Sclerostin and the regulation of bone formation: Effects in hip osteoarthritis and femoral neck fracture. *Journal of Bone and Mineral Research*, 25 (8):1867–1876, 2010.

[153] J. von Hardenberg, E. Meron, M. Shachak, and Y. Zarmi. Diversity of vegetation patterns and desertification. *Phys. Rev. Lett.*, 87:198101, Oct 2001.

[154] John Pastor, Yosef Cohen, and Ron Moen. Generation of spatial patterns in boreal forest landscapes. *Ecosystems*, 2(5):pp. 439–450, 1999.

[155] George W. Barlow. Hexagonal territories. *Animal Behaviour*, 22, Part 4(0):876 – IN1, 1974.

[156] Johan van de Koppel, Joanna C. Gascoigne, Guy Theraulaz, Max Rietkerk, Wolf M. Mooij, and Peter M. J. Herman. Experimental evidence for spatial self-organization and its emergent effects in mussel bed ecosystems. *Science*, 322(5902): 739–742, 2008.

Acknowledgment

I would like to express my gratitude to all the people who supported me during my doctoral studies. My special thanks go first to my supervisor Dr. Richard (Ricci) Weinkamer who continuously supported my work. The discussions with him and especially his ability to provide constructive criticism boosted my training as a researcher and he gave me the latitude to solve scientific problems independently. Through his commitment, I felt motivated to peek into a variety of projects and thus gained knowledge and skills in a wide spectrum of science.
I would like to thank Prof. Dr. Dr. h.c. Peter Fratzl, whose support was the foundation for a productive and rewarding experience in his department at the Max Planck Institute.
I would like to express special thanks to those who supported the individual projects that comprise my dissertation: Dr. Paul Roschger for providing experimental data and the discussions about the BMDD; Prof. Dr. Ron Shahar for the 'osteonal project'; and to Prof. Dr. Ralph Müller who enabled my stay at his department at the ETH in Zurich and let me work on the mouse data.
For their willingness to be external referees and their support for my PhD, I would like to thank Prof. Dr. Igor Sokolov and Prof. Dr. Dr. h.c. Jürgen Kurths.
I would also like to thank many of my colleagues who helped me when I had 'small' technical problems and who helped me learning new methods. First of all, Dr. Davide Ruffoni for the use of his custom script program and for his patience in discussing it with me. He also ensured that my work was productive in Zurich - thanks a lot, Davide. I am also grateful to Dr. Philip Kollmannsberger for many scientific (and also non-scientific) discussions. He repeatedly pulled me back from the brink of programming-related insanity. I would like to thank Dr. Clara Valverde-Serrano for bringing the secrets of chemistry to light for me. Last but not least I express my gratitude to Dr. Stefanie Krauß and Dr. Dmitri Fix for their really careful reading of this thesis and for making very helpful suggestions.
During my stay in Zurich, Dr. Floor Lambers and Dr. Friederike Schulte helped me with XIPL, a new programming language I had to learn to evaluate the micro-CT im-

ages. I also want to thank the whole group at the ETH for the very supportive and nice atmosphere.
Besides the pure scientific support, I would like to express many thanks to my colleagues at the MPI who have motivated me every day to pursue my goal and who were responsible for the good working atmosphere at the institute.

Selbständigkeitserklärung

Ich erkläre, dass ich die vorliegende Arbeit selbständig und nur unter Verwendung der angegebenen Literatur und Hilfsmittel angefertigt habe. Ich habe bisher an keiner Universität, weder im Inland oder Ausland, einen Promotionsversuch unternommen.
Ich erkläre, dass ich die Promotionsordnung der Mathematisch-Naturwissenschaftlichen Fakultät I der Humboldt-Universität zu Berlin in der Fassung vom 01.09.2005 anerkenne.

Berlin, den 07.08.2012 Carolin Lukas